UNIVERSITY OF NOVA GORICA
GRADUATE SCHOOL

STRUCTURAL AND MAGNETIC PROPERTIES OF Fe-DOPED $BaTiO_3$ CERAMICS

DISSERTATION

Iuliia Mikulska

Mentors: prof. dr. Iztok Arčon, prof. dr. Matjaž Valant

Nova Gorica, 2014

UNIVERZA V NOVI GORICI
FAKULTETA ZA PODIPLOMSKI ŠTUDIJ

STRUKTURNE IN MAGNETNE LASTNOSTI $BaTiO_3$ KERAMIKE DOPIRANE Z ŽELEZOM

DISERTACIJA

Iuliia Mikulska

Mentorja: prof. dr. Iztok Arčon, prof. dr. Matjaž Valant

Nova Gorica, 2014

“If you challenge yourself, you will grow. Your life will change. Your outlook will be positive. It’s not always easy to reach your goal but that’s no reason to stop. Never say die. Say yourself ‘I can do it. I’ll keep on trying until I win.’”

© Richard Branson ("Screw It, Let's Do It")

ACKNOWLEDGMENTS

First, I owe my deepest gratitude to my supervisors *Prof. Dr. Iztok Arčon* and *Prof. Dr. Matjaž Valant*, who have guided me, supported and provided with constructive ideas during my Ph.D. studies. Without their passion, enthusiasm, and encouragement this research would have never been completed. Therefore I strongly believe that I am fortunate to graduate under their guidance.

I would like to express my sincere gratitude to *Doc. Dr. Darja Lisjak* from the Advanced Materials Department at Jožef Stefan Institute, Ljubljana (Slovenia) who has provided the magnetization measurements used in the scope of my dissertation. I am grateful to *Prof. Dr. Nataša Zabukovec Logar* from Laboratory for Inorganic Chemistry and Technology at the National Institute of Chemistry in Ljubljana (Slovenia) for performing the XRD measurements. The data provided by them helped me a lot to accomplish this work.

I would like to acknowledge the provided access to synchrotron radiation facilities of HASYLAB (beamline C), ESRF (beamline BM23), and ELETTRA (XAFS beamline). I also would like to thank *Roman Chernikov* and *Edmund Welter* of HASYLAB and *Giuliana Aquilanti* and *Luca Olivi* of ELETTRA for expert advice on beamline operation. The CENN Nanocenter is acknowledged for the usage of the VSM. The National Institute of Chemistry is acknowledged for usage of XRD.

I am grateful to the Slovenian Research Agency for financial support.

I would like to express my gratitude to my committee members, *Prof. Dr. Urška Lavrenčič Štangar*, *Prof. Dr. Jana Padežnik Gomilšek* and *Prof. Dr. Adriano Filipponi*.

I specially would like to thank *Tea Stibilj Nemec* for help with administrative issues, making possible my arrival and stay in Slovenia.

I owe sincere and earnest thankfulness to my high school physics teacher, *Aleksandr Osherovich Korzhenevich*, who has opened the wonderful world of Physics to me.

It is pleasure for me to thank *Dr. Praveen Chandramathy Surendran* and *Dr. Mirela Dragomir* for their help, friendship, and advices given to me during my Ph.D. studies, especially in the beginning.

A special "thank you" goes to *Metka Benčina* and *Tina Mavrič* for our fruitful discussions, exchanges of knowledge and skills during my Ph.D. studies.

I would also like to take this chance to express my gratitude towards my colleagues, with whom I had the opportunity to work: *Egon Pavlica, Romain Bachelard, Benoît Mahieu Mattia Fanetti, Michael Pitcher, Saim Emin, Dmitry Orlov, Manisha Chhikara,* Raveendra Babu *Penumala, Kateryna Vyshniakova, Mojca Vrčon, Sandra Gardonio, Saša Badalič, Miro Zdvoc, Layla Samos, Simona Ovtar, Danijel Stojković, Maja Wagner, Vesna Mržek, Jinta Mathew, Srinivasa Rao Pathipathi, and Artem Badasyan*. They provided a friendly and cooperative atmosphere at work and made my daily life here joyful.

I am truly indebted and thankful to my best friends *Elena, Olga S. Olga. Y., Evgeniya, and Igor* for their support, understanding and encouragement.

Last, but not least I would like to express my deepest gratitude to my parents, who always believed in me and supported me with my creative endeavors. Without their constant love and encouragement, I would never finish this thesis.

ABSTRACT

The dissertation investigates the effect of annealing temperature and time on structural and magnetic properties of Fe-doped $BaTiO_3$, a potential room-temperature dilute magnetic oxide.

In order to understand the origin of the mechanism of ferromagnetic behaviour in this system in connection with its structural properties, especially the local coordination and valence state of Fe cations in the crystal structure of $BaTiO_3$ a detailed structural analysis has been performed using XAS methods.

We synthesized 10% and 20% Fe-doped $BaTiO_3$ by solid state reaction method. The initial powders were treated at different annealing temperatures (1250ºC and 1500ºC) for different time (1h, 3h, 5h, 10h and 50h).

The X-ray diffraction data showed that all the samples have single phase hexagonal 6H-$BaTiO_3$ crystal structure, except 10% Fe-doped $BaTiO_3$ sample fired at 1250ºC, which contains a minor amount of the tetragonal phase in addition to the prevailing 6H-$BaTiO_3$ phase.

The magnetic properties of the samples were measured by a vibrating sample magnetometer. The results of the magnetic measurements showed that all the samples fired at 1250ºC were paramagnetic. All additionally annealed samples exhibited ferromagnetic behaviour, except 10% Fe-doped $BaTiO_3$ additionally annealed at 1500ºC for only 1 h, which is still paramagnetic.

To understand the source of the ferromagnetism we used X-ray absorption spectroscopy methods (XANES and EXAFS) to obtain detailed information on a local structure of the Fe cations incorporated into the 6H-$BaTiO_3$ crystal structure. The Fe K-edge EXAFS analysis showed that in all the samples Fe^{3+} substituted Ti^{4+}. We found that in 10% Fe-doped $BaTiO_3$ fired at 1250ºC 50% of Fe atoms occupied the Ti(1) crystallographic sites, while another 50% of Fe occupied the Ti(2) sites. After the additional annealing at 1500ºC for 10h the ordering of oxygen vacancies on the O(2/2) crystallographic site was detected. On the other hand, the Fe K-edge EXAFS analysis shows that Fe^{3+} ions are randomly distributed over Ti(1) and Ti(2) sites in 20% Fe-doped $BaTiO_3$ samples treated at 1250ºC. During annealing at 1500ºC redistribution of the Fe cations was detected, leading to formation of Fe-Fe pairs in the face-sharing octahedrons on the Ti(2) sites. We have showed that the room-temperature ferromagnetism in Fe-doped $BaTiO_3$ samples cannot be explained

by double exchange interaction, p-d Zener model or RKKY interaction. In the 10% Fe-doped $BaTiO_3$ samples the oxygen vacancies are associated with induction of the room-temperature ferromagnetism and would favour the BMP model. In the 20% Fe-doped $BaTiO_3$ samples the formation of Fe-Fe pairs coincides with induction of the ferromagnetism. Based on our experimental results, it was shown that the ordering processes are associated with induction of room–temperature ferromagnetism.

KEYWORDS: Barium titanate; Oxygen vacancy; Fe K-edge EXAFS; XANES;

POVZETEK

Doktorska disertacija raziskuje vpliv temperature in časa sintranja na strukturne in magnetne lastnosti Fe-dopiranega $BaTiO_3$, potencialnega redčenega magnetnega oksida pri sobni temperaturi. Z namenom razumevanja izvora mehanizma feromagnetnega vedenja v tem sistemu, v povezavi s strukturnimi lastnostmi, zlasti lokalno koordinacijo in valenčnim stanjem Fe kationov v kristalni strukturi $BaTiO_3$, je bila izvedena podrobna strukturna analiza s pomočjo XAS metod.

Sintetizirali smo 10% in 20% Fe-dopiran $BaTiO_3$ z reakcijo v trdnem stanju. Začetni prahovi so bili obdelani pri različnih temperaturah (1250°C in 1500°C) in različnem času sintranja (1h, 3h, 5h, 10h in 50h).

Rezultati pridobljeni z rentgensko difrakcijo so pokazali, da imajo vsi vzorci enofazno heksagonalno 6H- $BaTiO_3$ kristalno strukturo, razen 10% Fe-dopiran $BaTiO_3$ vzorec, sintran pri 1250°C, ki ima manjši delež tetragonalne faze poleg prevladujoče 6H $BaTiO_3$ faze.

Magnetne lastnosti vzorcev smo izmerili z vibracijskim magnetometrom. Rezultati magnetnih meritev so pokazali, da so bili vsi vzorci sintrani pri 1250°C paramagnetni. Vsi dodatno sintrani vzorci so bili feromagnetni, razen 10% Fe-dopiran $BaTiO_3$ dodatno sintran pri 1500°C 1 uro, je še vedno kazal paramagnetne lastnosti.

Da bi razumeli vir feromagnetizma smo uporabili metode rentgenske žarkovne absorpcijske spektroskopije (XANES in EXAFS), z namenom pridobitve podrobnih informacij o lokalni strukturi Fe kationov, vključenih v kristalno strukturo 6H-$BaTiO_3$. EXAFS analiza Fe roba K je pokazala, da v vseh vzorcih Fe^{3+} nadomesti Ti^{4+}. Ugotovili smo, da v 10% Fe-dopiranem $BaTiO_3$ sintranem pri 1250°C, 50% Fe atomov zasede Ti(1) kristalografske pozicije, medtem ko drugih 50% Fe zasede Ti(2) pozicije. Po dodatnem sintranju pri 1500°C za 10h smo opazili urejanje kisikovih vrzeli na O(2/2) kristalografski poziciji. Po drugi strani pa EXAFS analiza Fe roba K kaže, da so Fe^{3+} ioni naključno porazdeljeni na Ti(1) in Ti(2) poziciji v 20% Fe-dopiranih $BaTiO_3$ vzorcih, sintranih pri 1250°C. Med sintranjem pri 1500ºC smo odkrili prerazporeditev Fe kationov, kar je pripeljalo do tvorbe Fe-Fe parov na Ti(2) poziciji v Ti_2O_9 poliedrih (nastanek Fe_2O_9 poliedra). Pokazali smo, da feromagnetizma pri sobni temperaturi v Fe-dopiranih $BaTiO_3$ vzorcih ni mogoče razložiti z izmenjalno interakcijo, p-d Zener-jevim modelom ali Ruderman-Kittel-

Kasuya-Yosida interakcijo.V 10% Fe-dopiranih $BaTiO_3$ vzorcih so kisikove vrzeli povezane z indukcijo feromagnetizma pri sobni temperaturi, kar bi lahko podprli z modelom magnetnega polarona. V 20% Fe-dopiranih $BaTiO_3$ vzorcih tvorba Fe-Fe parov sovpada z indukcijo feromagnetnega sklapljanja. Na podlagi naših eksperimentalnih rezultatov se je izkazalo, da so postopki urejanja povezani z indukcijo feromagnetizma pri sobni temperaturi.

KLJUČNE BESEDE: barijev titanat; kisikova vrzel; Fe rob K EXAFS; XANES;

TABLE OF CONTENTS

List of Figures

List of Tables

List of Symbols and Abbreviations

DMS	Dilute Magnetic Semiconductors
DMO	Dilute Magnetic Oxides
XRD	X-ray Diffraction
TEM	Transmission Electron Microscope
XMCD	X-Ray Magnetic Circular Dichroism
XAS	X-ray Absorption Spectroscopy
XANES	X-ray Absorption Near Edge Structure
EXAFS	Extended X-ray Absorption Fine Structure
RKKY	Ruderman-Kittel-Kasuya-Yosida
BMP	Bound Magnetic Polaron
6H-$BaTiO_3$	hexagonal $BaTiO_3$
VSM	Vibrating Sample Magnetometer

1 INTRODUCTION

1.1. Dilute magnetic semiconductors and oxides

Today's electronic devices are based on the semiconducting materials and utilize only the charge degree of freedom of electrons. However in last decade, much interest is focused on the exploiting of the spin of the electron as additional degree of freedom. The field of science and technology, which studies the control and manipulation of the spin degrees of freedom of electrons in addition to their charge, is called spintronics [1-6]. Using the charge of the electron together with its spin can improve performance of conventional electronic devices, making them faster, smaller and more versatile. To realize the electronic devices based on both aforementioned degrees of freedom, new materials, which possess simultaneously semiconducting and ferromagnetic properties at room temperature, are needed. One family of such promising materials that have been predicted to meet aforesaid requirements, are dilute magnetic semiconductors (DMS). DMS are nonmagnetic semiconducting materials, such as InAs and GaAs, which exhibit ferromagnetic properties when doped with a small amount of transition metal (TM) ions, such as Fe, Co or Mn (Figure 1.1) [7-10]. A disadvantage of these materials is a very low Curie temperature, less than 200 K [11-13]. The range of working temperatures for such materials is far below the room-temperature, what significantly limits the field of their application.

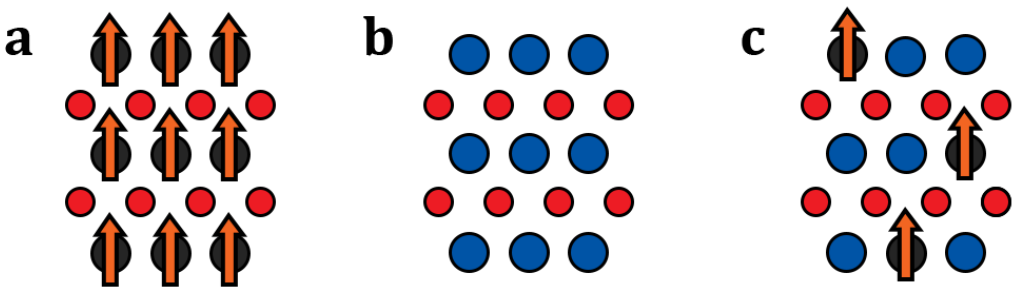

Figure 1.1. Schematic representation of the (a) magnetic semiconducting material, (b) nonmagnetic semiconducting material and (c) DMS and DMO materials. Blue circles are nonmagnetic cations, red circles are anions and black circles are magnetic cations. The arrows represent the magnetic moments of magnetic cations.

Dietl et al. predicted theoretically the room-temperature ferromagnetism in semiconducting oxide materials doped with the transition metal ions [14]. These materials are called dilute magnetic oxides (DMO) [15-17]. Later, the theoretical predictions were confirmed experimentally [18, 19]. For some potential DMO candidates (e.g. Mn-doped ZnO [18], Fe-doped SnO_2 [20]) it was shown that they possess room-temperature ferromagnetism. However, even for these well-investigated systems some disputes over the intrinsic nature of the magnetism exist [21, 22].

In the analysis of magnetism in DMO candidates it is very important to rule out the presence of secondary phases in these systems, which can be a spurious source of magnetism. There were a number of cases (Co:ZnO, Mn:ZnO, Mn:$KTaO_3$, Mn:$SrTiO_3$,) where it was shown that the ferromagnetism in the lightly doped oxide systems with the transition metal ions results from extrinsic sources, such as magnetic secondary phases, magnetic impurities, clustering of magnetic species, contaminations etc. [17, 23-27]. For example, in HfO_2 thin films the ferromagnetic coupling came from contamination with steel tweezers [28]. Even a small amount of the magnetic impurities can generate spurious magnetic signals, large enough to be detected by magnetometers. A combination of different techniques such as X-ray diffraction (XRD), transmission electron microscope (TEM), X-ray magnetic circular dichroism (XMCD), X-ray absorption spectroscopic methods XANES (X-ray Absorption Near Edge Structure) and EXAFS (Extended X-ray Absorption Fine Structure), are usually necessary to identify the source of ferromagnetism in DMO [24, 29-31].

Five different mechanisms were proposed in the literature to explain the intrinsic ferromagnetism in DMS and DMO systems [10]. First model is known as Ruderman-Kittel-Kasuya-Yosida (RKKY) interaction. This model is used to explain the ferromagnetism in metals, and later it was adopted to explain the ferromagnetism in DMS and DMO systems [8, 32]. In this model the interaction between localized magnetic moments of the dopant ions is mediated by band carriers introduced by these magnetic ions. However, in weakly doped systems, there are not enough charge carriers for establishing the long-range ferromagnetic ordering. The second model was proposed by Dietl and is known as the p-d Zener model [14]. This model was proposed to describe the origin of magnetism in Mn-doped p-type semiconductors, such as Mn-doped GaAs and

Mn-doped ZnO. According to this model the Mn ions provide both localized spins and itinerant holes. These holes mediate the magnetic interaction between the localized spins, resulting in the ferromagnetism. In the third model, the effect has been assigned to the double-exchange mechanism, where the magnetic interaction arises between the dopant cations in different valence state [33, 34]. In the fourth model it was suggested that interaction between magnetic nearest neighbour cations is mediated by non-magnetic anions, referring to the super-exchange interaction [35]. However, the double-exchange interaction as well as the super-exchange interactions cannot produce the long-range magnetic order in lightly doped systems. Thus, the conventional interactions used for explaining ferromagnetic behaviour in bulk ferromagnetic materials cannot be applied to DMO and DMS materials. Finally, the bound magnetic polaron (BMP) model, also known as the defect-mediated mechanism, was proposed to explain the ferromagnetism in DMO and DMS systems [32]. According to this model the oxygen vacancies create defect states within the band gap and act as trap levels to capture the delocalized electrons inside the sample [36]. All aforementioned magnetic interactions are further discussed in the Chapter 2.

1.2. Fe-doped $BaTiO_3$

Tetragonal perovskite $BaTiO_3$ is a well-known ferroelectric material. Achieving a magnetic ordering in the semiconducting $BaTiO_3$ by magnetic ions doping can extend the field of its application. The room temperature ferromagnetism has been predicted theoretically [37] and confirmed experimentally [38, 39] in $BaTiO_3$ doped by TM, such as Zn, Ni, Co, Fe, Mn and Cr.

The Fe-doped $BaTiO_3$ was found to be the most promising candidate for DMO group due to the presence of magnetic order [36, 39-52] in combination with semiconducting properties [36] and magnetoelectric coupling [40, 53-56].

Technological importance has triggered a number of studies on this material in a wide range of dopant concentrations. It was found that doping of $BaTiO_3$ by Fe ions stabilizes the hexagonal 6H-$BaTiO_3$ structure at room temperature [57]. The details about the $BaTiO_3$ structure are described in Chapter 3. Recently, the effect of Fe dopant on the transformation from tetragonal perovskite to hexagonal phase of

$BaTiO_3$ in the samples, prepared by solid state reaction method, has been investigated [45, 56-61]. It was found that 6H-$BaTiO_3$ structure can accommodate up to 84% of Fe ions by replacing Ti in the host matrix [59]. It is generally agreed that doping by Fe ions promotes formation of hexagonal phase of $BaTiO_3$ [45, 56-61]. This phase was found to be fully stabilized at high doping levels (≥13%) [48, 49, 51, 57-62]. For doping levels less than 2% the pure tetragonal perovskite phase of $BaTiO_3$ was observed [45, 56, 58, 63]. The intermediate dopant concentrations yield two phase mixture with the tetragonal perovskite and 6H phases [45, 56, 58]. An increase in the Fe content from x=0.01 to x=0.13 in the system with a general formula $BaTi_{1-x}Fe_xO_3$ gradually increases the crystalline volume fraction of the hexagonal phase, and reduces the volume fraction of the tetragonal phase [45, 56]. However, there are some conflicting reports in the literature about the minimum quantity of Fe needed to stabilize the pure hexagonal barium titanate structure. Vanderah et al. [59] reported the pure hexagonal phase for 6% Fe-doped $BaTiO_3$ prepared by multiple one week heatings at 1250 ºC - 1270 ºC. On the other hand, the two-phase mixture for the samples with the same dopant concentration but synthesised under different conditions, were reported by other researchers [45, 56, 58]. It was found that the formation of the hexagonal phase of Fe-doped $BaTiO_3$ can be promoted by higher sintering temperature [56, 60], longer sintering time [56] or even by using different synthesis methods, such as floating zone technique [44].

The Fe-doped $BaTiO_3$ system has unique magnetic properties. The samples with doping levels less than 2% exhibit paramagnetic behaviour [44, 56], while in the samples with higher doping concentrations (≥ 2%) the room-temperature ferromagnetism was observed [40, 42, 44, 45, 48-50, 53, 56, 64]. But even at higher dopant concentrations magnetization did not reach complete saturation at room temperature, which suggests coexistence of ferromagnetic and paramagnetic phases [45, 48, 49, 53].

At all doping concentrations unusual behaviour of saturation magnetization was observed [42, 44, 45, 49, 56]. Qiu et al. [56] showed that at low doping levels of 2%-10% the saturation magnetization did not show a monotonic trend with increasing dopant concentration. They observed an increase in saturation magnetization with increasing amount of iron up to 4%, where saturation magnetization reached its maximum value. At doping levels of 4% - 6% the saturation magnetization

decreased, while at higher doping levels (≥6%), it increased again. In a study by Dang et al. [45], only paramagnetic behaviour was observed in the samples with Fe content in the range of 2%-6%. At higher doping levels (≥10%) the saturation magnetization gradually decreased with increasing Fe content [42, 45, 49]. Lin et al. [49], synthesized $Ba(Ti_{1-x}Fe_x)O_3$ ceramics with 7%, 30% and 70% of Fe and found that all samples were ferromagnetic and their saturation magnetization decreased with increasing amount of the dopant. On the other hand, Wei et al. [42] showed that sample with 70% of Fe exhibited the paramagnetic behaviour. The saturation magnetization of the sample with 30% of Fe was much smaller compared to that reported by Lin et al. [49]. All aforementioned differences in the magnetic properties of Fe-doped $BaTiO_3$ were attributed to different sample fabrication conditions.

The effect of synthesis conditions, such as the annealing atmosphere, annealing temperature and the length of annealing time on magnetic properties of Fe-doped $BaTiO_3$ has been investigated by several different authors [48, 50, 56, 65]. Chakraborty et al. [65] showed that the ferromagnetism is enhanced when samples were annealed inside evacuated quartz tube, compared to those annealed in an oxygen atmosphere. The opposite was observed by Lin et al. [48], who showed smaller saturation magnetization after vacuum annealing, compared to samples annealed in oxygen ambient. Qiu et al. [56] investigated the effect of the annealing time on the ferromagnetic properties of 10% Fe-doped $BaTiO_3$ sintered at 1250ºC. They found that an increase in the sintering time from 5 h to 15 h leads to an increase in the saturation magnetization. Similar results were obtained by Lin. et al., who found an increase in the saturation magnetization of $BaTi_{0.93}Fe_{0.07}O_3$ after the pre-sintering time increased from 36 h to 108 h [50].

Despite the intensive research and a number of reports that claim the room-temperature ferromagnetism in the Fe-doped $BaTiO_3$ the origin of the magnetic coupling still remains unexplained [36, 42, 44, 45, 49, 56, 65]. Some authors claim that the room temperature ferromagnetism is attributed to some structural characteristics, such as ordering of oxygen vacancies [40] or formation of Fe_2O_9 polyhedra within 6H-$BaTiO_3$ unit cell [44, 66], while others attribute the ferromagnetic behaviour to the double exchange interaction, due to the simultaneous presence of Fe^{3+} and Fe^{2+} or Fe^{4+} valence states [47, 48, 58]. Also, there are

assumptions that Ti^{4+} is partially reduced to Ti^{3+}, which can contribute to the ferromagnetic coupling [40].

Often, the unusual ferromagnetism in the Fe-doped $BaTiO_3$ was attributed to oxygen vacancies [36, 40, 65]. According to electrostatic neutrality, replacement of Ti^{4+} by Fe^{3+} is accompanied by formation of oxygen vacancies. It is generally agreed, that oxygen vacancies are segregated in the phase-sharing plane of the hexagonal crystal structure of Fe-doped $BaTiO_3$ [49, 60, 61, 67, 68]. Experimental results of Wei et al. showed that the room-temperature ferromagnetism in heavily doped Fe-doped $BaTiO_3$ is attributed to dynamic exchanges of the trapped electrons among bound magnetic polarons, referring to the defect mediated mechanism [36]. Chakraborty et al. reported a study on 5% Fe-doped $BaTiO_3$ single crystal with varied oxygen content [65]. They found that amount of ferromagnetically interacting Fe ions increases with the increasing concentration of the oxygen vacancies, again suggesting the defect-mediated mechanism. Lin et al. assumed presence of pentahedrally coordinated Fe^{3+} associated with oxygen vacancies in vacuum annealed $Ba(Ti_{0.3}Fe_{0.7})O_3$ ceramic [48, 50]. They suggested that the origin of the ferromagnetism can be attributed to the competition between different super-exchange interactions: ferromagnetic pentahedral-pentahedral and pentahedral-octahedral Fe^{3+} interactions and anti-ferromagnetic octahedral-octahedral Fe^{3+} interaction.

On the other hand, there are a number of reports, where ferromagnetism is attributed to competing super-exchange and double-exchange interactions between Fe or Ti cations in mixed valence state. Lin et al. claimed that both Fe^{3+} and Fe^{4+} ions coexist in oxygen annealed $Ba(Ti_{0.3}Fe_{0.7})O_3$ ceramic [48]. They assumed that the origin of the ferromagnetism can be attributed to the competition between different interactions: ferromagnetic Fe^{4+}-O^{2}-Fe^{4+} and anti-ferromagnetic Fe^{3+}-O^{2}-Fe^{4+} and Fe^{3+}-O^{-2}-Fe^{3+}. Wei et al. suggested that besides the defect-mediated mechanism responsible for ferromagnetism in their $Ba(Ti_{1-x}Fe_x)O_{3-\delta}$ (x=1/6 and 1/3) also the Ti^{3+} cations notable contribute to magnetic properties [36].

Xu et al. [55] in their study of polycrystalline 5% Fe-doped $BaTiO_3$ suggested that the electron-mediated Zener interaction is responsible for the ferromagnetism. According to this mechanism the Fe atom on Ti sites in $BaTiO_3$ provides both, the localized magnetic moments and charge free carriers. Thus, the exchange interaction

between the local moments is mediated by the free electrons inducing the ferromagnetism in the Fe-doped $BaTiO_3$

1.3. Research objectives and thesis outline

Since the magnetic properties of Fe-doped $BaTiO_3$ remain a controversial topic, a detailed study on existence of the intrinsic magnetic ordering in such systems is needed. The main aim of our research is to understand the ferromagnetic behaviour of this system in connection with its structural properties, especially the local coordination and valence state of Fe cations in the crystal structure of $BaTiO_3$ ceramics. Following this goal, we have focused on the solid-state synthesis of the ferromagnetic Fe-doped $BaTiO_3$ at two different doping concentrations (10% and 20%). Considering, the significant influence of synthesis conditions on the structure and magnetic properties of this compound [48, 50, 56, 65] the effect of annealing temperature and time on the ferromagnetic properties of the Fe-doped $BaTiO_3$ compositions with different Fe concentration have been investigated. All heat treatments were carried out in oxygen atmosphere in order to stabilize Fe^{3+} valence state and at the same time to prevent formation of Ti^{3+}. With intention to understand the possible structural differences between samples, heat-treated at different conditions, and to correlate them with magnetic properties, different characterization techniques, such as XRD, X-ray absorption spectroscopic methods (XANES and EXAFS), vibrating sample magnetometer (VSM) were employed. To explore different mechanisms responsible for the ferromagnetism in 10% and 20% Fe-doped $BaTiO_3$ it is vital to investigate the Fe local structure. Thus, Fe K-edge EXAFS and XANES analysis of the local coordination and valence state of Fe cations in the crystal structure of $BaTiO_3$ ceramics were performed in order to determine the sites of incorporation of Fe cations in $BaTiO_3$ crystal structure, local deformations around Fe cations in the structure, the valence state of Fe cations, and the presence of eventual secondary iron phases, which may also be the source of magnetization. Ti K-edge XANES analysis was used to check the valence state of Ti cations.

The goals of the dissertation are:

1. Synthesis of the intrinsically ferromagnetic Fe-doped $BaTiO_3$ samples at different Fe doping concentrations.
2. Investigation of influence of annealing temperature and time on the ferromagnetic properties of Fe-doped $BaTiO_3$ compositions at different Fe doping concentrations.
3. Determination of the sites of incorporation of Fe cations in $BaTiO_3$ crystal structure and local deformations around Fe cations in the structure, by EXAFS and XANES analysis of the local coordination and valence state of Fe cations in the crystal structure of $BaTiO_3$ ceramics
4. Verification of the presence of eventual secondary iron phases, which may also be the source of magnetisation.
5. Investigation of the origin of magnetic properties in Fe-doped $BaTiO_3$ ceramics.

The dissertation is composed of seven themed chapters, including this introductory chapter. The Chapter 2 starts with introducing the physical quantities used to describe the magnetic properties of materials, following with description of basic properties of the main types of magnetic materials. The final section of this chapter gives the brief description of models used to describe ferromagnetism in DMO. This information is necessary to understand the controversy of the origin of magnetism in DMO. The Chapter 3 provides information about crystal structures of $BaTiO_3$. The Chapter 4 introduces the experimental methods employed in this study. First, the synthesis process of the samples is described. Then, several characterization techniques, such as VSM, XRD and X-ray absorption spectroscopic (XAS) methods are discussed. Chapter 5 presents the magnetic and structural properties of the synthesized 10% and 20% Fe-doped $BaTiO_3$ and correlations between structural changes in the samples treated at different annealing temperatures, and changes of their magnetic properties. In Chapter 6 different models, which may be responsible for ferromagnetism in Fe-doped $BaTiO_3$, are discussed. Finally, a brief summary on the major findings of the research is given.

2 MAGNETIC PROPERTIES

This chapter is split into four sections. Understanding the main aspects of collective magnetism is impossible without introducing the basic terms of magnetism. Thus, in the first section the fundamental concepts of magnetism, such as atomic magnetic moment, magnetization, magnetic field and susceptibility are introduced. In the second section we will consider some simple models, which are used to describe the main types of magnetism, i.e. paramagnetism, ferromagnetism, antiferromagnetism and ferrimagnetism. In many cases, different types of magnetism coexist in one material. The different type of magnetism can be distinguished by measurements of magnetization. The third section represents the method of separation of different types of magnetism superposed in hysteresis data. Finally, the last section is devoted to a discussion of models, which may account for ferromagnetism in such Fe-doped $BaTiO_3$ DMO system.

2.1 Magnetic parameters

2.1.1 Magnetic Moment

Unpaired electrons are playing an essential role in magnetism of magnetic materials. Total magnetic moment of the electrons consists of two components: spin magnetic moment and orbital magnetic moment. Spin magnetic moment is associated with internal angular momentum of the electrons, so called spin angular momentum. Orbital magnetic moment is associated with orbital motion of the electrons around the nucleus [69].

Let us consider the atom with single electron. First, the spin and the orbital magnetic moments of an electron will be considered. The magnitude of the spin angular momentum $\boldsymbol{s}$ for an electron is given by [69]:

$$|\boldsymbol{s}| = \sqrt{s(s+1)}\hbar = \sqrt{\frac{1}{2}\left(\frac{1}{2}+1\right)}\hbar = \sqrt{3}\frac{\hbar}{2}, \tag{2.1}$$

where $s = \frac{1}{2}$ is spin quantum number of the electron, $\hbar = \frac{h}{2\pi} = 6.626 \cdot 10^{-34}\, J \cdot s$ – reduced Planck's constant.

The component of spin angular momentum of the electron in the direction of specified axes z (for example, in the direction of external magnetic field $\boldsymbol{H}$) can take only two possible values:

$$s_z = m_s\hbar = \pm\frac{\hbar}{2}, \tag{2.2}$$

where $m_s = \pm\frac{1}{2}$ is spin quantum number.

Spin angular momentum is associated with spin magnetic moment and can be written as:

$$\boldsymbol{\mu_s} = -2\frac{\mu_B}{\hbar}\boldsymbol{s} \tag{2.3}$$

where $\mu_B = 9.274 \cdot 10^{-24} Am^2$ is Bohr magneton [70].

The z component of spin magnetic moment is given by:

$$\mu_z^{(s)} = -2\frac{\mu_B}{\hbar}s_z = \mp\mu_B, \tag{2.4}$$

Thus, according to (2.1) and (2.3) magnitude of the spin magnetic moment is

$$|\boldsymbol{\mu_s}| = \sqrt{3}\mu_B. \tag{2.5}$$

Now, let us consider the orbital magnetic moment of the electron. The orbital quantum number l gives the magnitude of the orbital angular momentum:

$$|\boldsymbol{l}| = \sqrt{l(l+1)}\hbar. \tag{2.6}$$

Similar to spin angular momentum, the component of orbital angular momentum of the electron along a particular axes z can take different values:

$$l_z = m_l \hbar, \tag{2.7}$$

where $m_l = l, (l-1), \dots, 0, \dots, -(l-1), -l$ is magnetic quantum number.
Similar to spin magnetic moment, the orbital magnetic moment is associated with orbital angular momentum and is defined by

$$\boldsymbol{\mu_l} = -\frac{\mu_B}{\hbar}\boldsymbol{l}. \tag{2.8}$$

Using (2.7) and (2.8) the components of magnetic orbital moment along particular axes z can be defined as:

$$\mu_z^{(l)} = m_l \mu_B. \tag{2.9}$$

The magnitude of orbital magnetic moment is written as

$$|\boldsymbol{\mu_l}| = \sqrt{l(l+1)}\mu_B. \tag{2.10}$$

Using (2.3) and (2.8) the total magnetic moment of the electron can be written as:

$$\boldsymbol{\mu_e} = \boldsymbol{\mu_s} + \boldsymbol{\mu_l} = -\frac{\mu_B}{\hbar}(2\boldsymbol{s} + \boldsymbol{l}). \tag{2.11}$$

Usually we are dealing with many-electron atoms. Let us define the total magnetic moment for many-electron atom.
The total angular momentum of the many-electron atom $\boldsymbol{J}$ is a vector sum of resultant spin $\boldsymbol{S} = \sum_i \boldsymbol{s_i}$ and resultant orbital $\boldsymbol{L} = \sum_i \boldsymbol{l_i}$ angular momenta of the electrons in many-electron atom and is given by:

$$\boldsymbol{J} = \boldsymbol{S} + \boldsymbol{L}. \tag{2.12}$$

The magnitude of the total angular momentum of many-electron atom is given by

$$|\boldsymbol{J}| = \sqrt{J(J+1)}\hbar, \tag{2.13}$$

where J is total angular momentum quantum number possessing the values: if $L \geq S$, then $J = L+S, L+S-1, \ldots, L-S$; if $L < S$, then $J = S+L, S+L-1, \ldots, S-L$, where $S = \sum_i s_i$ and $L = \sum_i l_i$ is resultant spin and orbital quantum numbers.
The component of the total angular momentum along fixed axes z is

$$J_z = m_J\hbar, \tag{2.14}$$

where $m_J = J, (J-1), \ldots, 0, \ldots, -(J-1), -J$ is azimuthal quantum number, which represents the projection of the vector of total angular momentum, $\boldsymbol{J}$, onto the z axe.
The total magnetic moment of the many-electron atom is given by the vector sum of total spin $\boldsymbol{\mu_S} = -2\mu_B\boldsymbol{S}$ and total orbital $\boldsymbol{\mu_L} = -\mu_B\boldsymbol{L}$ magnetic moments of the electrons:

$$\boldsymbol{\mu} = \boldsymbol{\mu_S} + \boldsymbol{\mu_L}, \tag{2.15}$$

where $\mu_S = 2\sqrt{S(S+1)}\mu_B$ and $\mu_L = \sqrt{L(L+1)}\mu_B$ are the magnitude of total spin and total orbital magnetic moments.
The total magnetic moment is connected with angular momentum which is quantized. The component of the total magnetic moment in the direction of applied magnetic field is given by [57]:

$$\mu_z^{(J)} = -g_J m_J \mu_B \tag{2.16}$$

where $g_J = \frac{3}{2} + \frac{S(S+1)-L(L+1)}{2J(J+1)}$ is Lande g-value.

2.1.2 Magnetization

Magnetic materials consist of atoms with non-zero magnetic moments. Individual atomic magnetic moments contribute to the resultant macroscopic magnetic moment of the whole substance. Therefore, for characterization of magnetic state of materials it is convenient to define magnetization, $\boldsymbol{M}$**.** Letting $\boldsymbol{\mu_i}$ be the magnetic moment of the i type of atom, the definition of the magnetization $\boldsymbol{M}$ is the magnetic moment per unit volume [71]:

$$\boldsymbol{M} = \frac{\sum_i \boldsymbol{\mu_i}}{V}, \tag{2.17}$$

where V is the volume of the magnetic solid.

Magnetization can also be expressed per unit mass, i.e. mass magnetization $\boldsymbol{\sigma}$:

$$\boldsymbol{\sigma} = \frac{\sum_i \boldsymbol{\mu_i}}{m_s}, \tag{2.18}$$

where m_s is the mass of the solid.

In case of dilute magnetic oxide materials only dopant ions are responsible for ferromagnetic interaction, while the ions of host oxide material do not give the contribution to the ferromagnetism. In such cases, it is convenient to express magnetization per atom in Bohr magnetons. Thus, we can convert the measured mass magnetization into magnetization in units of Bohr magnetons per dopant atoms M_X by follow expression [44, 48-51, 65]:

$$\mathrm{M}_X = \frac{M_s \sigma}{N_A \mu_\mathrm{B} X_d}, \tag{2.19}$$

where M_s – molar mass of the substance, X_d– amount of dopant atoms per formula unit, $N_A = 6.022 \cdot 10^{23}\ mol^{-1}$ – Avogadro's number. The value $\frac{N_A}{M_s}$ is the number of molecules per unit mass.

2.1.3 *Susceptibility*

Magnetization is the function of external magnetic field strength $\boldsymbol{H}$. For some materials magnetization is linearly dependent on the applied magnetic field and can be expressed as [72]:

$$\boldsymbol{M} = \chi \boldsymbol{H}, \tag{2.20}$$

where χ is the magnetic susceptibility. Similar to magnetization, susceptibility can be expressed as molar χ_m or massχ_g susceptibility [72]:

$$\begin{aligned} \chi_m &= \chi V_m, \\ \chi_g &= \frac{\chi}{\rho}. \end{aligned} \tag{2.21}$$

where V_m – molar volume of the substance, ρ – density of the substance.
In DMO materials, the susceptibility per dopant atoms χ_X in units of Bohr magnetons is introduced:

$$\chi_X = \frac{M_o \chi_g}{N_A \mu_B X_a}. \tag{2.22}$$

2.1.4 Energy of magnetic moment in magnetic field.

The energy of an atom with magnetic moment $\boldsymbol{\mu}$ in the externally applied magnetic field is called Zeeman energy and is given by [73]:

$$E = -\mu_0 \boldsymbol{\mu} \cdot \boldsymbol{H} = -\boldsymbol{\mu} \cdot \boldsymbol{B} \tag{2.23}$$

where $\boldsymbol{B} = \mu_0 \boldsymbol{H}$ is magnetic flux density, and magnetic permeability of vacuum is $\mu_0 = 4\pi \cdot 10^{-7} \frac{Vs}{Am}$.

Substituting (2.16) into (2.23) leads to:

$$\mathrm{E} = m_J g_J \mu_B \mu_0 H = m_J g_J \mu_B B. \tag{2.24}$$

2.2 Classification of magnetic materials

In matter, the atomic magnetic moments interact with each other and with their surroundings. Below the critical temperature such interaction results in collective behaviour, which reveals itself by the long-range magnetic orders, such as ferromagnetism, antiferromagnetism and ferrimagnetism. Above the critical temperature the magnetic order is broken and substance becomes paramagnetic.

Usually, the exchange interaction is used to explain the microscopic magnetic properties of majority of materials [40]. First, let us consider the system with two electrons. If two electrons are located close to each other the magnetic moments of these electrons interact with each other. This interaction is described by spin Hamiltonian given by [74]:

$$\boldsymbol{\mathcal{H}} = -J_{ex}\boldsymbol{s_1} \cdot \boldsymbol{s}_2, \tag{2.25}$$

where spins $\boldsymbol{s_1}$ and $\boldsymbol{s_2}$ of the electrons are parallelly aligned if the exchange integral, J_{ex}, is positive and antiparallel aligned if J_{ex} is negative.

However, atoms in magnetic substances have many electrons, which interact with each other. Thus, the two-spin Hamiltonian can be extended to the many-electron system by summing over all pairs of ions [74]:

$$\boldsymbol{\mathcal{H}} = -\sum_{\boldsymbol{ij}} J_{ij}\boldsymbol{S_i} \cdot \boldsymbol{S_j}, \tag{2.26}$$

where J_{ij} is the exchange integral between the total spins $\boldsymbol{S_i}$ and $\boldsymbol{S_j}$ of neighboring atoms i and j.

2.2.1 Paramagnetism

Paramagnetic behavior is inherent to all substances composed of atoms, ions and molecules which have unpaired electrons on its electronic shells. Thus, in paramagnetic materials the net magnetic moment of individual atoms is nonzero. In the absence of magnetic field the magnetic moments are pointed in random directions and, resultant magnetic moment is zero (Figure 2.1 a). The applied external magnetic field rotates individual atomic magnetic moments in the direction of the external filed, resulting in the nonzero magnetization. Magnetic susceptibility of paramagnetic materials is positive. Paramagnetic materials have small value of the magnetic susceptibility (between 10^{-6} - 10^{-3}), which depends on the temperature [69, 70]. For paramagnetic materials the magnetization is linearly dependent on applied external magnetic field: (Figure 2.1 b).

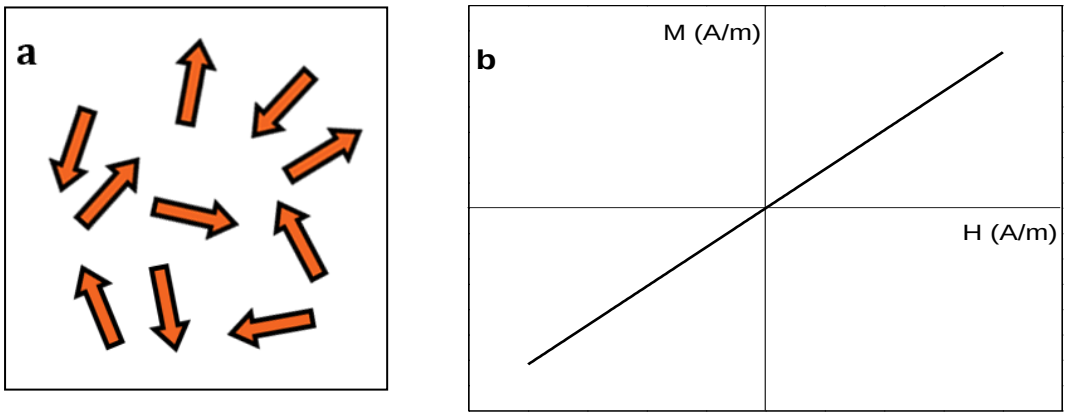

Figure 2.1. (a) Schematic representation of the atomic spins arrangement for magnetic field $\boldsymbol{H} = \boldsymbol{0}$ in the paramagnetic material. (b) Dependence of magnetization on external magnetic field strength for paramagnetic materials.

Let us calculate the paramagnetic susceptibility for paramagnetic material at temperature T. The Free energy of the system can be expressed by [69, 72]:

$$F = -k_B T \ln Z, \tag{2.27}$$

where $Z = \sum_n e^{-\frac{E_n}{k_B T}}$ is partition function of a system of N atoms with E_n being the energy of a single atom with magnetic moment $\boldsymbol{\mu}$ in magnetic field $\boldsymbol{H}$ (2.24).

Therefore magnetization of N ions in volume V can be expressed by

$$M = -\frac{N}{V}\frac{\partial F}{\partial H} = k_B T \frac{N}{V}\frac{\partial \ln Z}{\partial H} = -\frac{N}{V}\frac{\sum_n \frac{\partial E_n}{\partial H} e^{-\frac{E_n}{k_B T}}}{\sum_n e^{-\frac{E_n}{k_B T}}} \tag{2.28}$$

Substituting (2.24) into (2.28) we get:

$$M = -\frac{N}{V}\frac{\sum_{m_j=-J}^{+J} g_J \mu_B m_j e^{-\frac{g_J \mu_B \mu_0 H}{k_B T} m_j}}{\sum_{m_j=-J}^{+J} e^{-\frac{g_J \mu_B \mu_0 H}{k_B T} m_j}}. \tag{2.29}$$

In case when $\mu_B \mu_0 H \ll k_B T$ the paramagnetic susceptibility is given by Curie Law:

$$\chi_p = \frac{N \mu_B^2 g_J^2 J(J+1)}{3 V k_B T}. \tag{2.30}$$

2.2.2 Ferromagnetism

Ferromagnetic material is material, where at microscopic scale all atomic magnetic moments are aligned parallel in the absence of applied external magnetic field, below the critical temperature. Thus, at macroscopic scale ferromagnetic material exhibits spontaneous magnetization. In general, magnetic materials are composed of small microscopic regions separated by boundaries. Within each such region all atomic magnetic moments are aligned. These regions are so called magnetic domains. The boundaries between magnetic domains are called domain walls. The volume of one magnetic domain is very small and ranges between $10^{-12}\ m^3$ and $10^{-8}\ m^3$ [75]. In unmagnetized sample the resultant magnetic moment is zero, because the net magnetic moments of different domains are randomly oriented in the absence of external magnetic field (Figure 2.2 a, b). Applying the external magnetic field leads to the expansion of volume of magnetic domains with the net magnetic moment parallel to the external magnetic field and rotation of domains as a whole in the

direction of external magnetic field [74]. The expansion of the domain volume is realized at the expense of unfavorably oriented domains (Figure 2.2 c). In the end of the process sample is magnetized: the net magnetic moment of the sample is parallel to the external magnetic field (Figure 2.2 d).

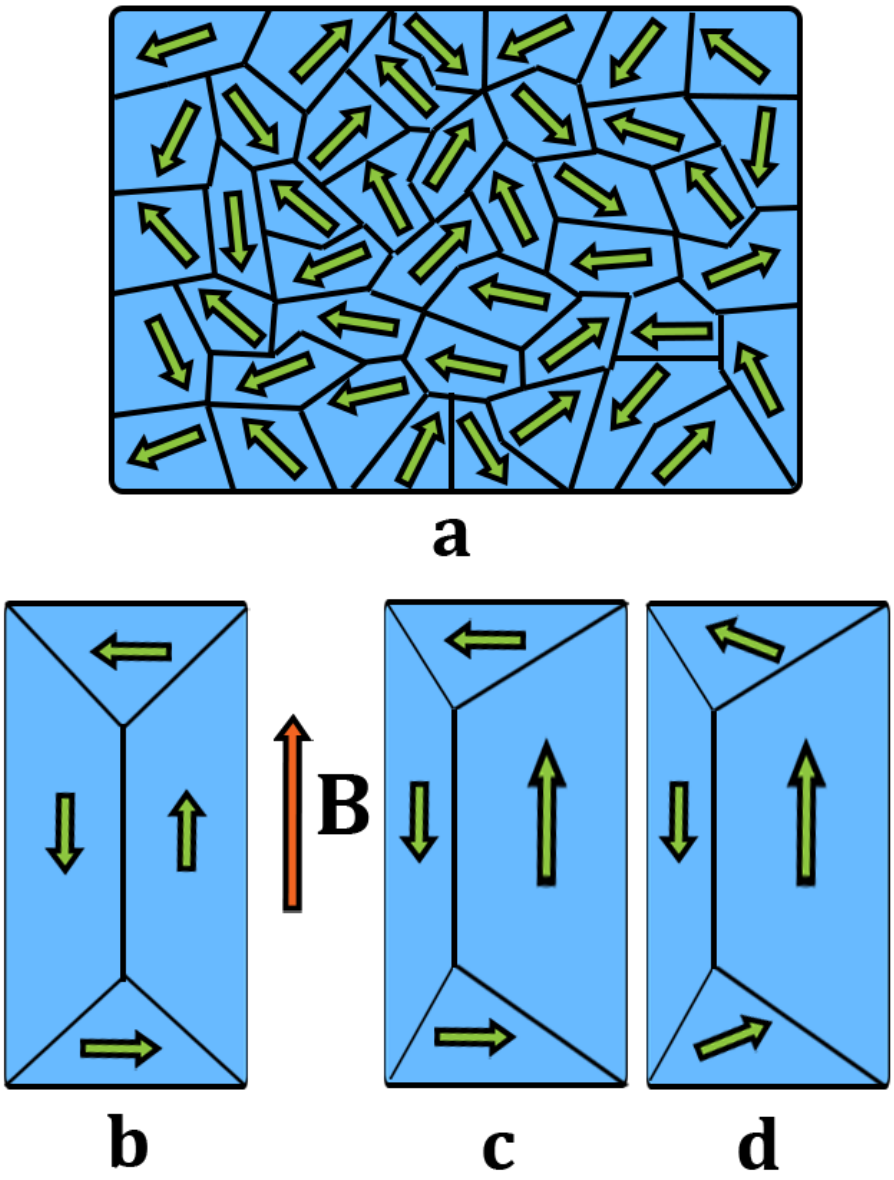

Figure 2.2. (a and b) Schematic presentation of random orientation of net magnetic moments of domains in unmagnetized sample. (c) Sample is in a weak external magnetic field ***B***. The volume of domains with magnetic moment parallel to the applied magnetic field expands by motion of domain walls. (d) As the magnetic field becomes stronger the domains start to rotate in the direction of external magnetic field.

The characteristic magnetization dependence on applied external magnetic field for ferromagnetic material is called a hysteresis loop. The hysteresis loop for ferromagnetic materials is presented on Figure 2.3 b. The magnetization is increasing with increasing magnitude of applied magnetic field. When all magnetic moments are aligned parallel the saturation magnetization M_S is reached. Decreasing of the applied magnetic field leads to decreasing of the magnetization, however at $H = 0$ the magnetization still remains nonzero. This is so called remanent magnetization, M_r. To obtain the zero magnetization ($M = 0$) it is necessary to apply the external magnetic field of magnitude $-H_c$ which is called the coercive field. Further increasing of the magnitude of the external magnetic field in opposite direction leads to saturation of the material in opposite direction ($-M_s$). If the magnitude of magnetic field increases again the return curve at $H = 0$ comes through negative remanent magnetization ($-M_r$). Zero value of magnetization is obtained at positive coercive fiel ($+H_c$) and finally saturated magnetization is reached ($+M_s$).

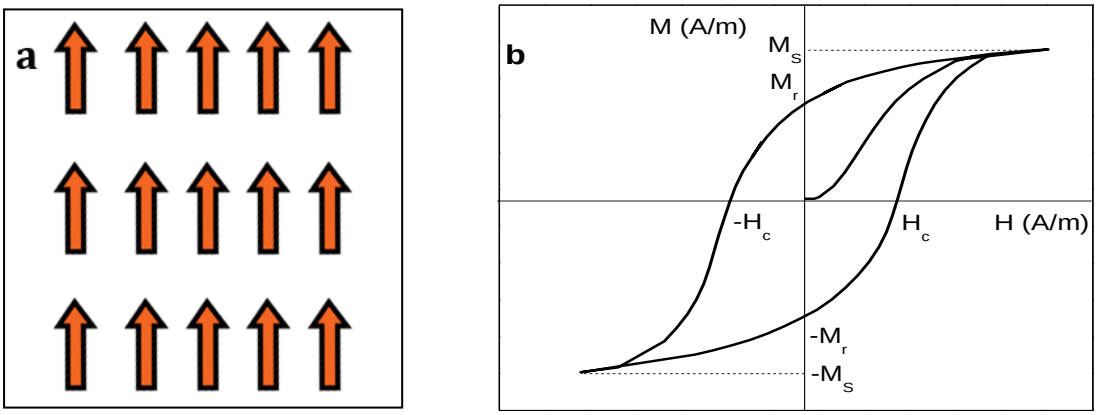

Figure 2.3. (a) Schematic representation of the atomic spins arrangement in a single domain in the ferromagnetic material. (b) Dependence of magnetization on external magnetic field strength for ferromagnetic materials.

The magnitude of the saturation magnetization is strongly dependent on the temperature: increasing the temperature leads to the decreasing of saturation magnetization. There is a certain temperature at which the ferromagnetic properties of the material disappear and material becomes paramagnetic. This temperature is called the Curie temperature, T_C.

Let us come back to microscopic aspects of ferromagnetism. Let us consider a set of magnetic ions with resultant spin $\boldsymbol{S}$ each, which interact with each other, and in the presence of applied external magnetic field $\boldsymbol{H}$. Thus, using (2.23) and (2.26) Hamiltonian for such system can be expressed by [76]:

$$\boldsymbol{\mathcal{H}} = -\sum_{\boldsymbol{ij}} J_{ij}\boldsymbol{S_i}\cdot\boldsymbol{S_j} + g\mu_B\sum_{j}\boldsymbol{S_j}\cdot\boldsymbol{B}, \tag{2.31}$$

P. Weiss proposed the model for describing ferromagnetic behaviour. According to Weiss assumptions the interaction of magnetic ions with its neighbours can be described using molecular field $\boldsymbol{B_{mf}}$. Molecular field at the i^{th} site can be defined as [72]:

$$\boldsymbol{B_{mf}} = -\frac{2}{g_J\mu_B}\sum_{j} J_{ij}\boldsymbol{S_j}. \tag{2.32}$$

The total exchange interaction of i^{th} spin with its neighbourhood is $-2\sum_{\boldsymbol{j}} J_{ij}\boldsymbol{S_i}\cdot\boldsymbol{S_j}$ where factor of 2 is due to double counting. Thus, this total exchange interaction can be expressed through the molecular field, using (2.32) by:

$$-2\boldsymbol{S_i}\sum_{\boldsymbol{j}} J_{ij}\cdot\boldsymbol{S_j} = g\mu_B\boldsymbol{S_i}\cdot\boldsymbol{B_{mf}}. \tag{2.33}$$

Therefore, substituting (2.33) into (2.31) the Hamiltonian can be written as:

$$\boldsymbol{\mathcal{H}} = g_J\mu_B\sum_{i}\boldsymbol{S_i}\cdot\left(\boldsymbol{B}+\boldsymbol{B_{mf}}\right). \tag{2.34}$$

The molecular field aligns the neighbouring magnetic moments, thus it can be assumed that the molecular field is proportional to magnetization:

$$\boldsymbol{B_{mf}} = \lambda\boldsymbol{M}, \tag{2.35}$$

where λ is the molecular field constant.

The magnetization is given by:

$$M = M_s B_J(y), \tag{2.36}$$

where $B_J(y)$ is Brullion function and $y = \frac{g_J \mu_B J(B+\lambda M)}{k_B T}$.

Increasing of the temperature leads to disorientation of magnetic moments and at Curie Temperature (T_c) magnetization disappears. Curie temperature can be expressed by:

$$T_C = \frac{g_J \mu_B (J+1) \lambda M_s}{3k_B}. \tag{2.37}$$

2.2.3 Antiferromagnetism

The phenomenon when closest magnetic moments are aligned antiparallel to each other is called antiferromagnetism [72]. Such ordering will be broken at temperatures higher the transition temperature called Neel temperature, T_N. Usually, in real materials this situation is realized when there are two equivalent sublattices. Thus, in one sublattice magnetic moments are looking up (↑), while in other one they look down (↓). Thus, we have two ferromagnetically ordered sublattices. Because sublattices are equivalent the magnetic moments of atoms in each sublattice are equal in size, but pointed in opposite directions. In absence of magnetic field the net magnetization is zero (Figure 2.4). The magnetization curve of the antiferromagnetic material is shown on the Figure 2.4 (b and c) [72, 77]. There are two different cases of the response of material to external magnetic field. In the first case the magnetization is zero until the critical magnetic field of magnitude H_1 is applied (Figure 2.4 (b)). At this moment the spin-flop transition occurs: the angle between magnetizations of two sublattices becomes different from 180º. Further increasing of magnetic field leads to decreasing of the angle between magnetizations of two sublattices. This results in linear increasing of magnetization with increasing of applied magnetic field until saturation is reached at very large magnetic fields

($H_2 > 10$ T). In second case, if the anisotropy effect is strong the magnetization remains zero, until the critical magnetic field of magnitude H_3 is applied (Figure 2.4 c). At this moment the spin-flip transition occurs: the magnetization of one sublattice suddenly rotates for 180º and magnetization reaches saturation.

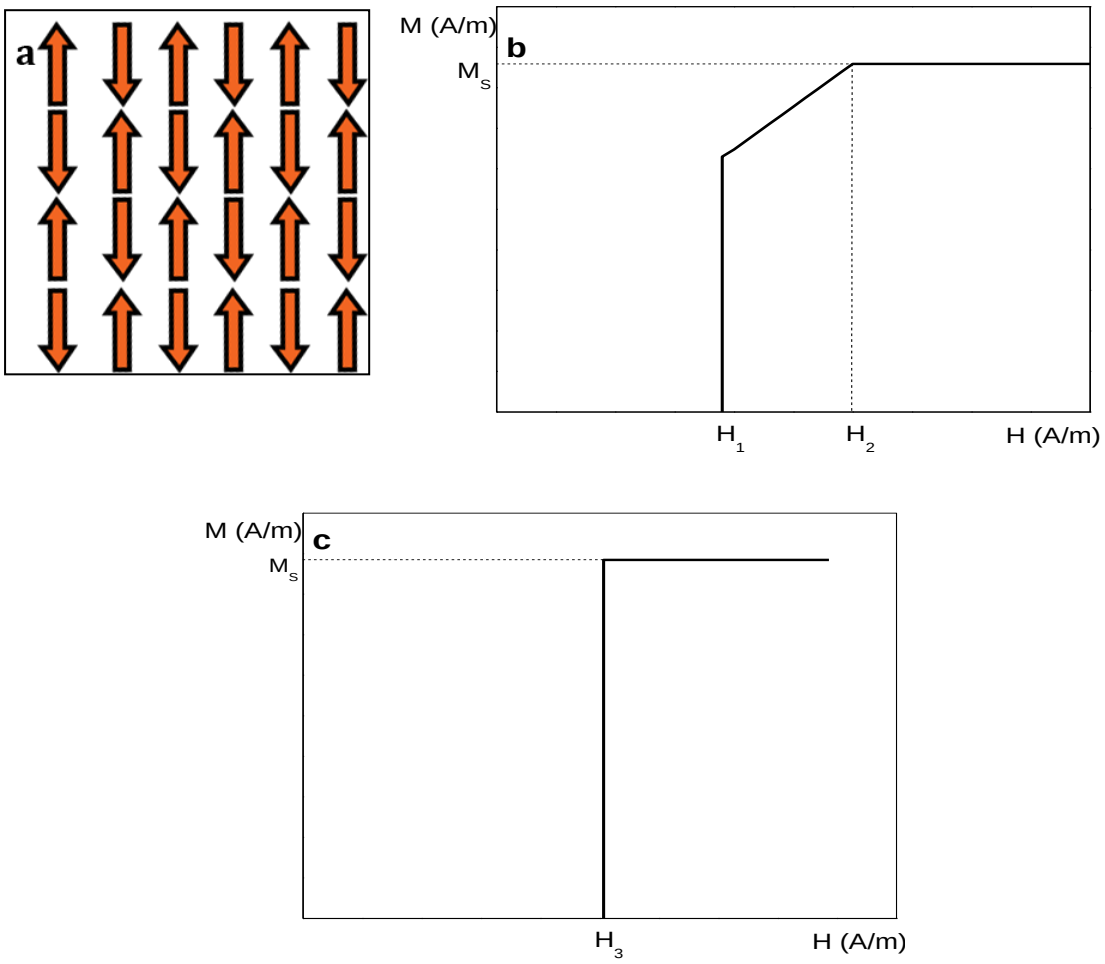

Figure 2.4. (a) Schematic representation of the atomic spins arrangement in the antiferromagnetic material. (b) and (c) Dependence of magnetization on external magnetic field strength for antiferromagnetic materials .

Thus, the antiferromagnetic material is material, where the magnetization, at atomic scale, is zero. Similar, as for ferromagnetism, the molecular field in each sublattice can be expressed by [76]:

$$\begin{aligned} \boldsymbol{B}_{\boldsymbol{mf}}^{\uparrow} &= -|\lambda|\boldsymbol{M}_{\uparrow} \\ \boldsymbol{B}_{\boldsymbol{mf}}^{\downarrow} &= -|\lambda|\boldsymbol{M}_{\downarrow} \end{aligned} \tag{2.38}$$

Then, magnetization in each sublattice can be given by

$$\begin{aligned} M_{\uparrow} &= M_s B_J\left(-\frac{g_J\mu_B J|\lambda|M_{\downarrow}}{k_B T}\right) \\ M_{\downarrow} &= M_s B_J\left(-\frac{g_J\mu_B J|\lambda|M_{\uparrow}}{k_B T}\right) \end{aligned}. \tag{2.39}$$

As it was mentioned earlier, the two sublattices are equivalent in everything except direction of the magnetic moments so

$$|\boldsymbol{M}_{\uparrow}| = |\boldsymbol{M}_{\downarrow}| = M \tag{2.40}$$

and hence the magnetization of each sublattice is

$$M = M_s B_J\left(-\frac{g_J\mu_B J|\lambda|M}{k_B T}\right). \tag{2.41}$$

The Neel temperature, T_N, at which the magnetization of each sublattice vanishes can be derived by:

$$T_N = \frac{(J+1)g_J\mu_B|\lambda|M_S}{3k_B}. \tag{2.42}$$

2.2.4 Ferrimagnetism

Similar to antiferromagnetic material, ferrimagnetic material also consist of two sublattices, however, these two sublattices are not equivalent. Therefore, the magnitudes of the magnetization of the two sublattices are different, resulting in nonzero net magnetization (Figure 2.5). The magnetization dependence on applied magnetic field for ferrimagnetic material is the same as for ferromagnetic material - hysteresis loop (Figure 2.5 b).

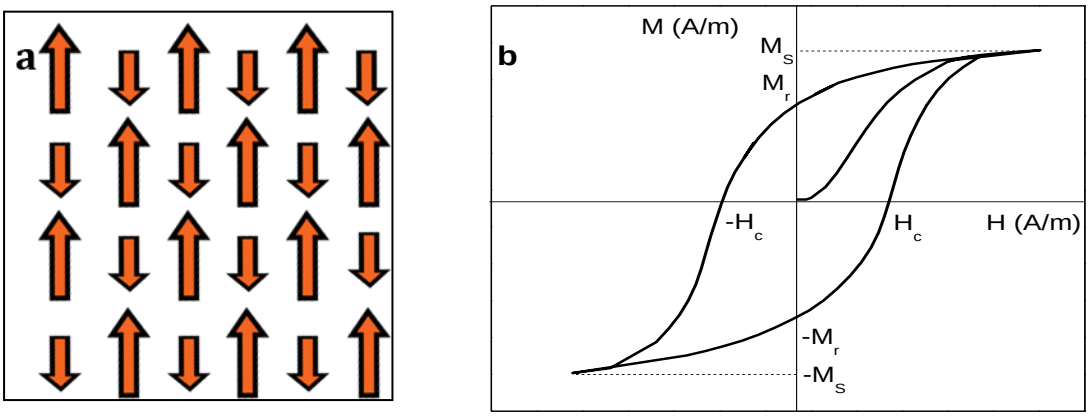

Figure 2.5. **(**a) Schematic representation of the atomic spins arrangement in the ferrimagnetic material. (b) Dependence of magnetization on external magnetic field strength for ferromagnetic materials.

Let us come back to microscopic aspects of ferrimagnetism. The magnitude of the molecular field in each sublattice can be expressed by [76]:

$$\begin{aligned} \boldsymbol{B}_{\boldsymbol{mf}}^{\uparrow} &= \upsilon_{\uparrow}\boldsymbol{M}_{\downarrow} + \omega_{\uparrow}\boldsymbol{M}_{\uparrow} \\ \boldsymbol{B}_{\boldsymbol{mf}}^{\downarrow} &= \upsilon_{\downarrow}\boldsymbol{M}_{\downarrow} + \omega_{\downarrow}\boldsymbol{M}_{\uparrow}, \end{aligned} \tag{2.43}$$

where $\upsilon_{\uparrow}, \omega_{\uparrow}, \upsilon_{\downarrow}, \omega_{\downarrow}$ are molecular field constants.
Due to the symmetry reason we have:

$$\upsilon_{\uparrow}, = \omega_{\downarrow} = -\lambda, \tag{2.44}$$

where $\lambda > 0$.

Let us set:

$$\begin{matrix} \upsilon_{\downarrow} = \alpha\lambda \\ \omega_{\uparrow} = \beta\lambda' \end{matrix} \tag{2.45}$$

Substituting (2.44) and (2.45) into (2.43) we get:

$$\begin{matrix} \boldsymbol{B}_{\boldsymbol{mf}}^{\uparrow} = \alpha\lambda\boldsymbol{M}_{\downarrow} - \lambda\boldsymbol{M}_{\uparrow} \\ \boldsymbol{B}_{\boldsymbol{mf}}^{\downarrow} = -\lambda\boldsymbol{M}_{\downarrow} + \beta\lambda\boldsymbol{M}_{\uparrow} \end{matrix}. \tag{2.46}$$

The magnetization in each sublattice can be expressed by:

$$\begin{matrix} M_{\uparrow} = \frac{c_{\uparrow}}{T}(B + \alpha\lambda\boldsymbol{M}_{\downarrow} - \lambda\boldsymbol{M}_{\uparrow}) \\ M_{\downarrow} = \frac{c_{\downarrow}}{T}(B - \lambda\boldsymbol{M}_{\downarrow} + \beta\lambda\boldsymbol{M}_{\uparrow}) \end{matrix}, \tag{2.47}$$

where $c_{\uparrow}$ and $c_{\downarrow}$ are constants.

The magnitude of the net magnetization is:

$$M = |M_{\uparrow} - M_{\downarrow}| = \frac{c_{\uparrow}T - c_{\uparrow}c_{\downarrow}\beta\mathrm{w} - c_{\uparrow}c_{\downarrow}\mathrm{w} - c_{\downarrow}T + c_{\uparrow}c_{\downarrow}\alpha\mathrm{w} + c_{\uparrow}c_{\downarrow}\mathrm{w}}{T^2 - \mathrm{w}(\alpha c_{\uparrow} + \beta c_{\downarrow})T + c_{\uparrow}c_{\downarrow}\mathrm{w}^2(\alpha\beta - 1)}B. \tag{2.48}$$

2.3 Discrimination of components in mixed magnetic systems

It is quite common situation when different types of magnetism coexist in one material resulting in a mixture of aforementioned magnetic contributions in hysteresis data [78, 79]. The presence of mixture of magnetic contributions can lead to the distortions of the magnetization curves. In this case, each of magnetic characteristic can be distinguished and separated from magnetic field dependence of magnetization.

The presence of paramagnetic phase is indicated by high field positive slope [48]. Figure 2.6 shows the example of hysteresis loop of the sample with superimposed ferromagnetic and paramagnetic contributions.

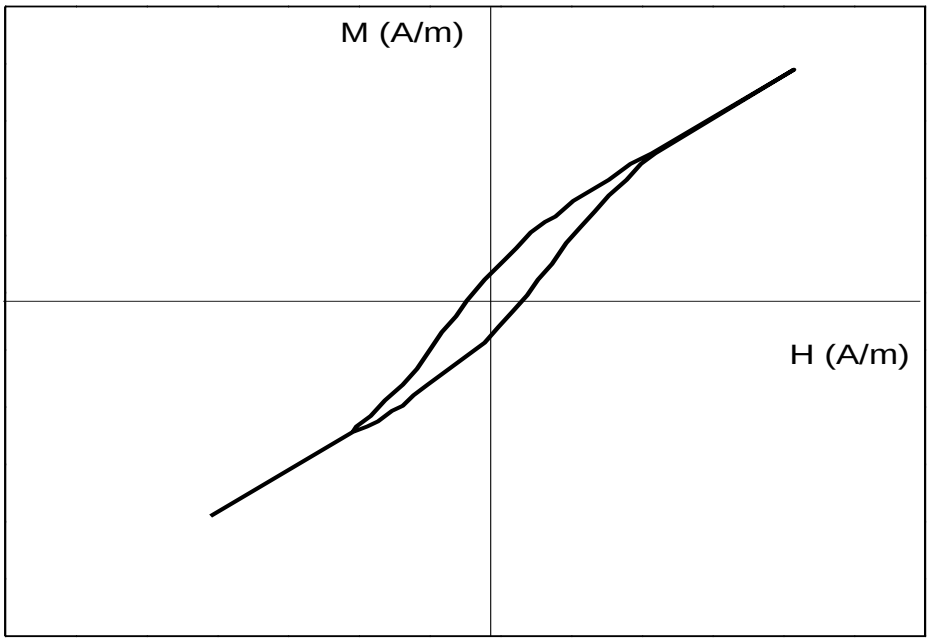

Figure 2.6 Induced magnetization as a function of an applied external magnetic field for a material with a mixture of paramagnetic response (linear) and ferromagnetic contributions (hysteresis loop).

Figure 2.7 shows the example of hysteresis loop of the sample with simultaneous ferromagnetic and antiferromagnetic contributions. The characteristic feature of the presence of the antiferromagnetic contribution is the constricted middle of the hysteresis loop, so called “wasp-waisted” hysteresis loop.

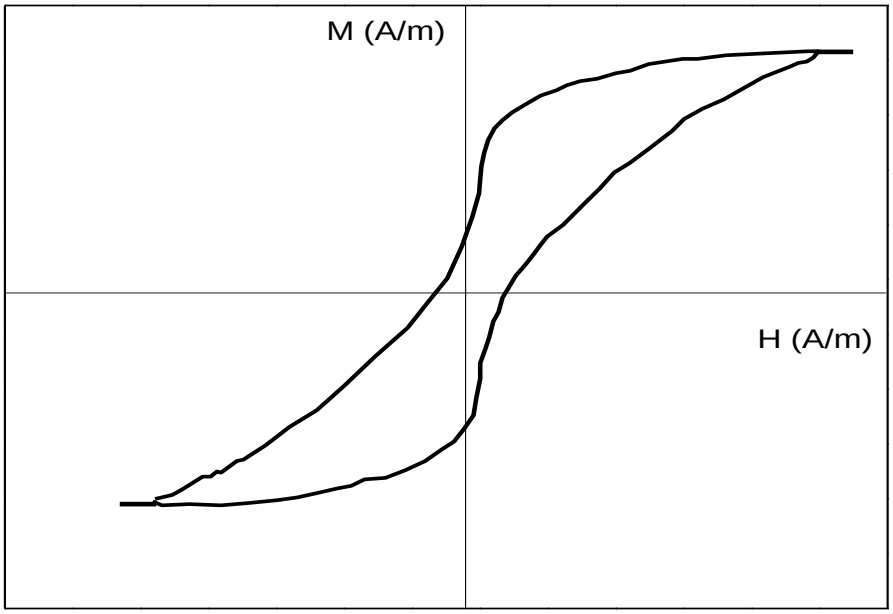

Figure 2.7. Induced magnetization as a function of an applied external magnetic field for a material with a mixture of antiferromagnetic and ferromagnetic contributions (hysteresis loop).

2.4. Ferromagnetism in Dilute Magnetic Oxides

Intrinsic ferromagnetism in dilute magnetic oxide materials cannot be explained by conventional exchange interaction due to the absence of free carriers in these systems. Below are considered models, which are used to explain intrinsic ferromagnetism in DMO and DMS systems.

2.4.1 Double exchange interaction

Double exchange appears in materials where magnetic ion is present in mixed valence state and results in ferromagnetic arrangement [80]. For example, in Mn-doped ZnO [18] Mn ions are presented as Mn^{3+} and Mn^{4+}. Thus, $3d$ orbitals of Mn directly interact with $2p$ oxygen orbitals. Mn^{4+} has vacant site on its e_g orbital, while Mn^{3+} has one electron on the e_g orbital (Figure 2.8). If spin up electron of $2p$ O orbitals will hop to e_g orbital of Mn^{4+}, then electron of Mn^{3+} will move to the vacant

$2p$ oxygen orbital. Therefore, in the end of the process one electron has been transferred between two Mn ions resulting in minimization of overall energy. In order to save the energy system ferromagnetically aligns.

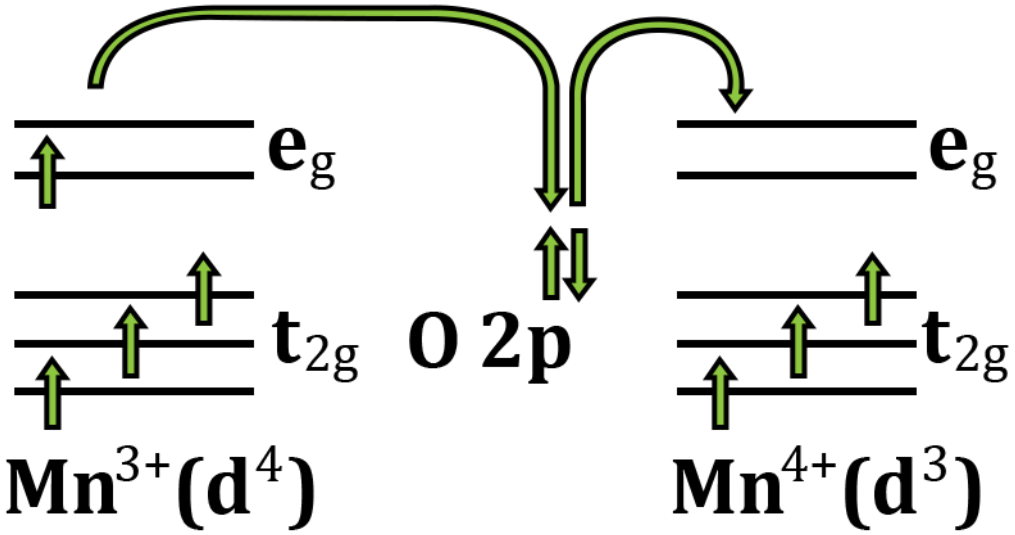

Figure 2.8. Schematic representation of the double exchange interaction of Mn^{3+}-O^{2-}-Mn^{4+}.

2.4.2 Bound Magnetic Polaron model

The Bound Magnetic Polaron (BMP) model was first suggested by J.B. Torrance et al. for describing the insulator-metal transition in Eu-reach EuO [81]. According to the BMP model, each oxygen vacancy contains two electrons, where one of the electrons is loosely bound and confined on the molecular orbital, while other electron is more rigidly bound. Therefore, oxygen vacancies are presented as shallow donors of electrons. The loosely bound electron on its orbit is overlapping Eu^{2+} ions and partially aligns their spins, forming the bound magnetic polaron. Overlapping of such bound magnetic polarons leads to the ferromagnetic exchange coupling between them.

Later BMP model was applied to the dilute n-type oxides materials by J. M. D. Coey et al. [32]. Each donor defect provides an electron which is confined to the hydrogenic orbital of the radius:

$$r_H = \epsilon \frac{m_e}{m^*} a_0, \tag{2.49}$$

where ϵ is the high-frequency dielectric constant, $a_0 = 5.29 \times 10^{-11} m$ is the Bohr radius, m_e is mass of the electron and m^* - effective mass of the donor electrons. Coey et al. [32] have calculated the values of hydrogenic radius of the loosely bound electron for some oxide materials such as ZnO, TiO_2 and SnO_2 and found it to be 0.76 nm, 0.48 nm and 0.86 nm, correspondingly. Let us introduce the donor concentration $\delta = \frac{n_{def}}{n_o}$, where n_{def}- is the density of defects and $n_o \approx 6 * 10^{28}\, m^{-3}$ is oxygen density for oxides with closed packed oxygen lattice. Increasing of the donor concentration δ leads to the creation of the impurity band by overlapping of 1s orbitals:

$$\psi(r) = \frac{1}{\sqrt{\pi r_H^3}} e^{-\frac{r}{r_H}}, \tag{2.50}$$

where r is the distance from nucleus.

We are dealing with DMO materials with the presence of magnetic dopant 3d cations. Thus, the donor electron on its orbital overlaps the magnetic cations and tends to align them, forming the bound magnetic polaron (Figure 2.9). The interaction of the spin of the electron with 3d spins of magnetic cations can be written as:

$$\Delta E_{ex} = -J_{sd} \boldsymbol{S} \cdot \boldsymbol{s} |\psi(r)|^2 \Omega, \tag{2.51}$$

where J_{sd}- is the s-d exchange parameter, $\boldsymbol{S}$ is the total spin of the 3d cations that have volume of $\Omega = \frac{4}{3}\pi r_c^3$, r_c is the radius of the cation, $\boldsymbol{s}$ is the donor electron spin, the electron density $|\psi(r)|^2 = \frac{3}{4\pi r_H^3}$ is constant when $r < r_H$, and zero otherwise.

This coupling between cation and donor electron can be either ferromagnetic or antiferromagnetic depending on the occupancy of the 3d band of magnetic cations: the interaction is ferromagnetic when 3d shell is less than half filled and is antiferromagnetic when shell is half-filled or more. However, coupling between two dopant cations within the same hydrogenic orbital is always ferromagnetic. The long range ferromagnetic coupling will appear only when polarons overlap. Therefore,

there is a certain n_{def} concentration of defects at which the formed polarons will overlap. It was found that long-range ferromagnetic interaction will be observed, when polarons fill about 16% of space or in other terms $\gamma^3\delta_{crit} \approx 4.3$. On the other hand, there is a solubility limit x_{crit} of transition metal dopants in the semiconducting material. Thus, the long–range ferromagnetic coupling will be observed when $x < x_{crit}$ and $\delta > \delta_{crit}$.

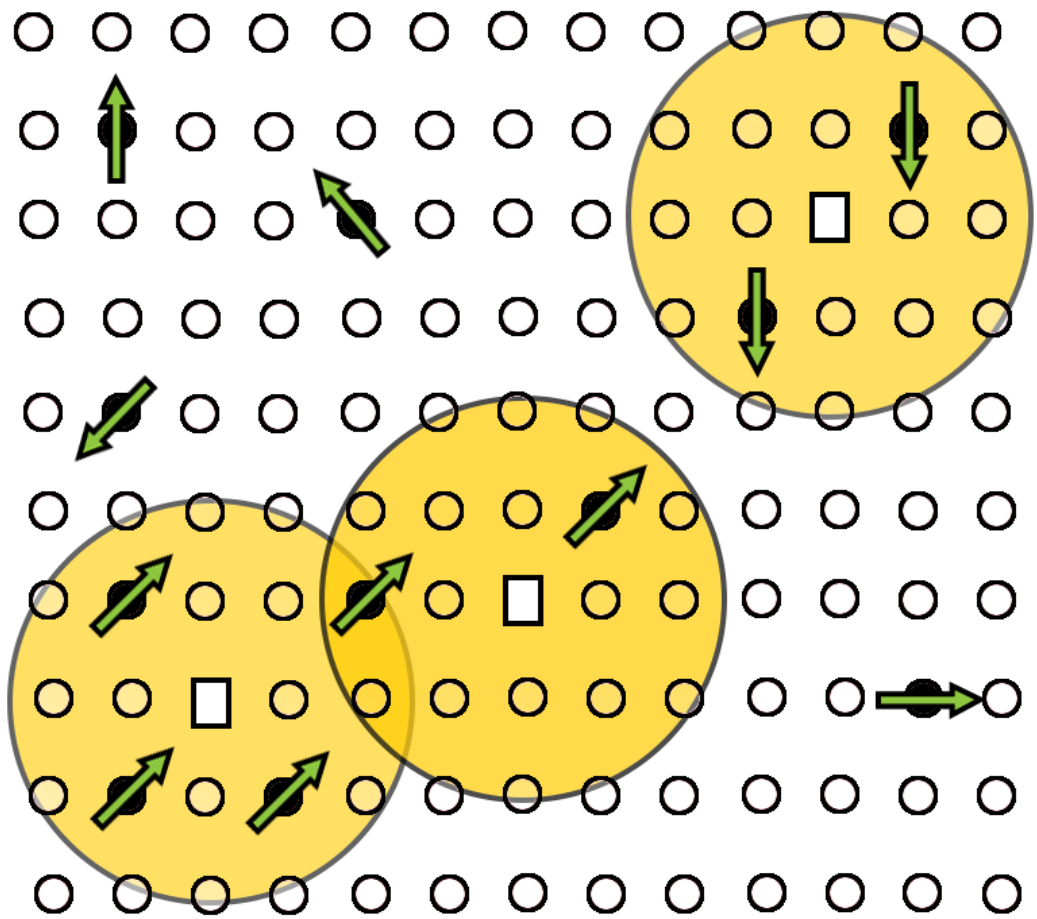

Figure 2.9. Schematic view of the BMP model. Black circles – the doping ions, squares – oxygen vacancies. Yellow circles indicate the forming polarons. Green arrows represents the magnetic moments of dopants.

2.4.3 Ruderman-Kittel-Kasuya-Yosida (RKKY) exchange

When concentration of donors increases the impurity band is merged with the conduction band and BMP model is not relevant anymore for describing the

ferromagnetic behavior in such systems. In this case RKKY exchange can be used [32]. This model suggests that magnetic ions interact through the conduction electrons.

The interaction of the point-like spin $\boldsymbol{S}$ with spins $\boldsymbol{s}$ of conduction electrons can be described by following Hamiltonian [32]:

$$\mathcal{H} = 2A\delta(\boldsymbol{r} - \boldsymbol{R})\boldsymbol{S} \cdot \boldsymbol{s}, \tag{2.52}$$

where A is the intra-atomic exchange parameter, δ – is delta function, which limits the interaction to be of contact form. While interaction between magnetic ions can be described by effective Heisenberg Hamiltonian [32]:

$$\begin{gathered} \mathcal{H} = -2\sum_{i<j}^{N} J(R)\boldsymbol{S_i} \cdot \boldsymbol{S_j} \\ J(R) = \frac{16A^2 m k_F^4}{(2\pi)^3 \hbar^2}\left[\frac{\cos(2k_F R)}{(2k_F R)^3} - \frac{\sin(2k_F R)}{(2k_F R)^4}\right] \end{gathered}, \tag{2.53}$$

where $J(R)$ is the RKKY exchange coefficient, the sign of which is oscillating with the distance. The RKKY interaction is strongly dependent on the distance between interacting ions and can be either ferromagnetic or antiferromagnetic.

2.4.4 p-d Zener model

This model was proposed by Dietl et al. [14, 82] in order to describe the origin of ferromagnetism in p-type Mn-doped semiconductors. According to this model the dopant ions act as acceptors and as the source of localized spins. The ferromagnetic interaction between localized magnetic moments of dopant ions is mediated by holes. The structure of the valence subbands can be described by Kohn-Luttinger six-band *kp* Hamiltonian [14]:

$$\boldsymbol{\mathcal{H}}_{pd} = \frac{\beta \boldsymbol{s}\boldsymbol{M}}{g\mu_B}, \tag{2.54}$$

where $\boldsymbol{M}$ is spatially uniform magnetization, β is coefficient.

According to this model the dopant spin magnetization $\boldsymbol{M}$ at given temperature, T, and magnetic field, H, can be written as:

$$\boldsymbol{M}(\boldsymbol{T}, \boldsymbol{H}) = x_{eff} N_A g_J \mu_B S B_J \left[\frac{g_J \mu_B \left(-\frac{\partial F_c[\boldsymbol{M}]}{\partial \boldsymbol{M}} + \boldsymbol{H} \right)}{k_B (T + T_{AF})} \right], \tag{2.55}$$

where x_{eff} is effective concentration of magnetic dopants, T_{AF} is Curie-Weiss temperature, $F_c[\boldsymbol{M}]$ is the free energy density of the carriers in the presence of dopant spins.

3 POLYMORPHISM OF $BaTiO_3$

Barium titanate is a very well-known ferroelectric material, one of the most widely used materials in electronic devices, such as thermistors, detectors capacitors, etc. [57]. This material is cheap, chemically and mechanically stable, environmentally friendly and can be used over a wide temperature range. $BaTiO_3$ is known to exist in different crystal structures: hexagonal, cubic, tetragonal, orthorhombic, and rhombohedral [83].

3.1 Hexagonal 6H-$BaTiO_3$

Hexagonal phase of $BaTiO_3$ with *P63/mmc* space group is thermodynamically stable over the temperature range from 1430ºC to 1623ºC, where the latter is melting point of the material. The lattice parameters of the unit cell are $a = b = 5.724$ Å and $c = 13.965$ Å measured at room temperature [84]. The unit cell (Figure 3.1) contains six atoms O(1), O(2), Ti(1), Ti(2), Ba(1) and Ba(2) at relative positions given in Table 3.1.

The 6H-$BaTiO_3$ structure is not a proper perovskite structure, even though it is often referred as such. A very unique feature of the 6H-$BaTiO_3$ structure are layers of $Ti(2)_2O(2)_9$ units that are composed of two face-sharing TiO_6 octahedral at *4f* site (Figure 3.1) [84, 85]. They are positioned between two layers of the perovskite-type corner-sharing $Ti(1)O(2)_6$ octahedra. The O(2) ions that are connecting the face-sharing octahedra, together with Ba(1) ions, form the hexagonal close-packed arrangement. In the $Ti(2)_2O(2)_9$ groups the highly charged Ti^{4+} ions are located at unusual proximity of 2.69 Å [85], which is, due to the high electrostatic repulsion, unfavourable for the stability of the structure.

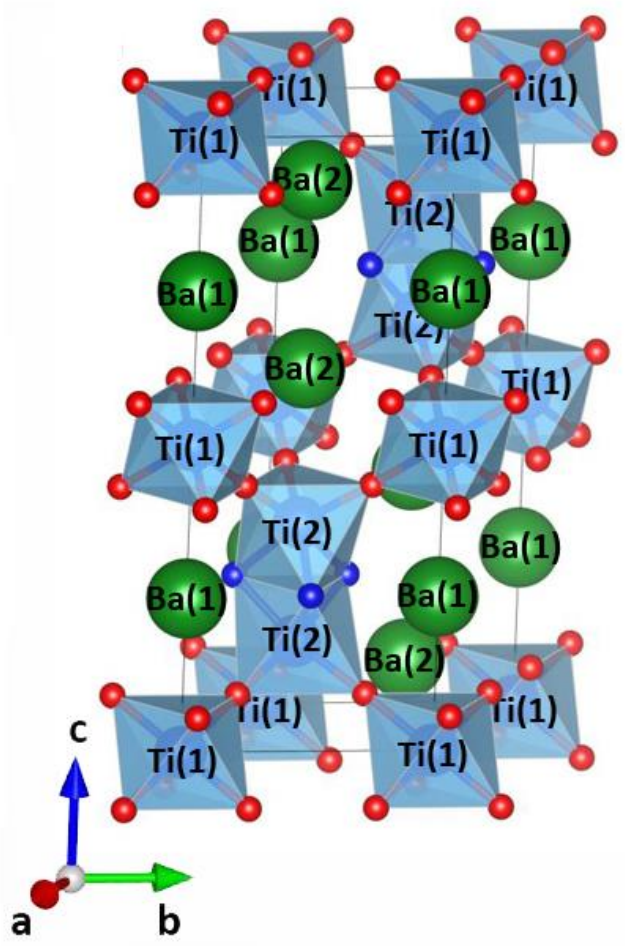

Figure 3.1. Schematic presentation of the unit cell of hexagonal 6H-$BaTiO_3$ crystal structure with the equivalent crystallographic sites annotated as Ti(1), Ti(2), Ba(1), and Ba(2). The red and blue spheres are oxygen atoms on the O(1) and O(2) crystallographic sites, respectively.

Table 3.1. Fractional atomic positions for hexagonal $BaTiO_3$ with *P63/mmc* space group [84].

Name	Element	X	Y	Z	Wyck.
O(1)	O	0.51850	0.03700	0.25000	6h
O(2)	O	0.83490	0.66980	0.08020	12k
Ti(1)	Ti	0.00000	0.00000	0.00000	2a
Ti(2)	Ti	0.33330	0.66670	0.84633	4f
Ba(1)	Ba	0.00000	0.00000	0.25000	2b
Ba(2)	Ba	0.33330	0.66670	0.09671	4f

3.2 Cubic perovskite $BaTiO_3$

The phase transition from hexagonal into cubic perovskite occurs in the temperature range between 1430°C and 1460°C. The cubic phase is stable down to 120°C. This cubic perovskite structure can be described with *Pm-3m* space group and a unit cell with $a = b = c = 3.996$ Å at room temperature [86]. The unit cell (Figure 3.2) contains three atoms O, Ti, and Ba at relative positions given in Table 3.2. The Ti^{4+} cations are located in the middle of the unit cell, Ba^{2+} cations in the corners and O^{2-} anions in the centre of the each face of the unit cell. Ti atoms are surrounded by six oxygen atoms, forming TiO_6 corner-sharing octahedra, while Ba atoms are cubohedrally coordinated by 12 oxygen atoms (Figure 3.2).

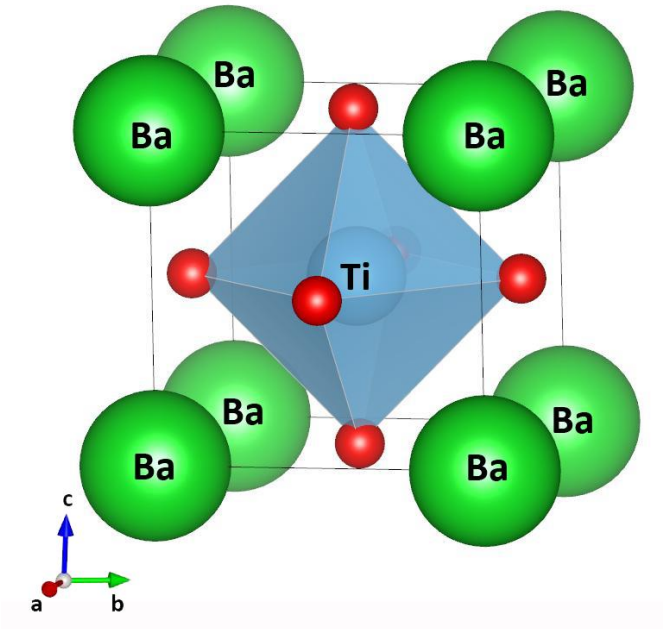

Figure 3.2. Schematic presentation of the unit cell of cubic perovskite $BaTiO_3$ crystal structure with the equivalent crystallographic sites annotated as Ti and Ba. The red spheres are oxygen atoms.

Table 3.2. Fractional atomic positions for cubic $BaTiO_3$ with a *Pm-3m* space group [86].

Element	X	Y	Z	Wyck.
O	0.50000	0.50000	0.50000	3c
Ti	0.50000	0.50000	0.50000	1b
Ba	0.00000	0.00000	0.25000	1a

3.3 Tetragonal perovskite $BaTiO_3$

At 120ºC a phase transition of the cubic $BaTiO_3$ perovskite into the tetragonal polymorph occurs. The tetragonal phase is stable from 120ºC down to 5ºC. This phase has a distorted perovskite crystal structure with *P4mm* space group and $a = b = 3.9950$ Å and $c = 4.0340$ Å [87]. The tetragonal crystal structure is a result of displacement of the ions from the symmetry positions along the c axes (Figure 3.3). The atomic positions in tetragonal $BaTiO_3$ are listed in the Table 3.3.

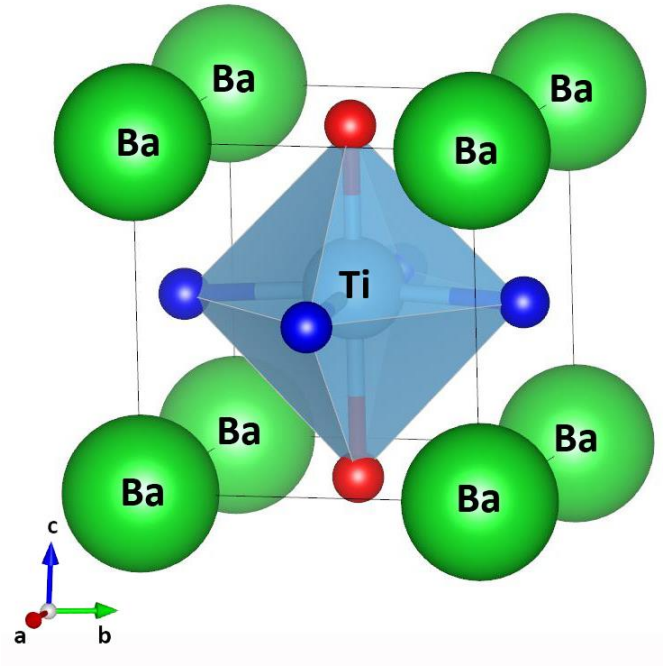

Figure 3.3. Schematic presentation of the unit cell of tetragonal $BaTiO_3$ crystal structure with the equivalent crystallographic sites annotated as Ti and Ba. The blue and red spheres are oxygen atoms on the O(1) and O(2) crystallographic sites, respectively.

Table 3.3. Fractional atomic positions for tetragonal $BaTiO_3$ [87].

Name	Element	X	Y	Z	Wyck.
O(1)	O	0.50000	0.00000	0.48500	2c
O(2)	O	0.50000	0.50000	0.97600	1b
Ti	Ti	0.50000	0.50000	0.51350	1b
Ba	Ba	0.00000	0.00000	0.00000	1a

3.4 Orthorhombic $BaTiO_3$

The phase transition from tetragonal into orthorhombic takes place at temperature of 5 ºC [88]. The orthorhombic (*Amm2* space group) form of $BaTiO_3$ is stable between -90ºC and 0ºC. The lattice parameters are a=3.9830 Å, b=5.6750 Å and c=5.6920 Å. The phase transition is accompanied by lattice distortions, which are associated with

tilting of the TiO_6 octahedra about the *a* and *b* axes and displacements of the Ba cations (Figure 3.4). The atomic positions in orthorhombic $BaTiO_3$ are listed in the Table 3.4.

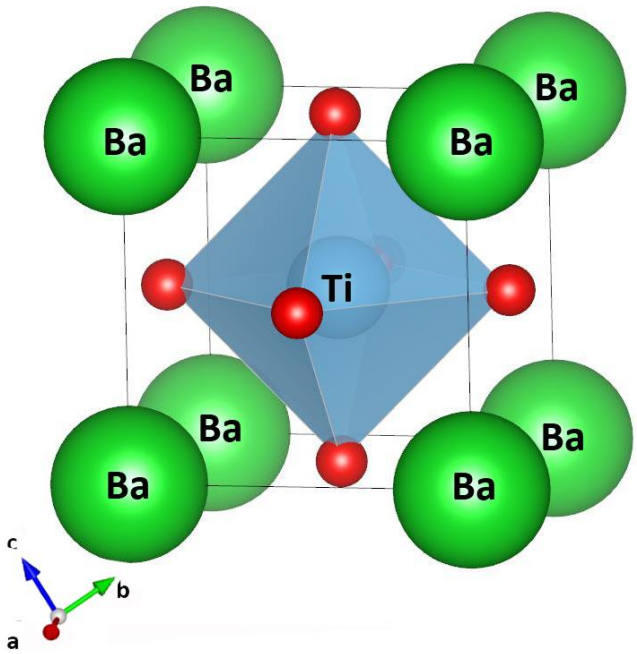

Figure 3.4. Schematic presentation of the unit cell of orthorhombic $BaTiO_3$ crystal structure with *Amm2* space group. The equivalent crystallographic sites are annotated as Ti and Ba. The red and blue spheres are oxygen atoms on the O(1) and O(2) crystallographic sites, respectively.

Table 3.4. Fractional atomic positions for orthorhombic $BaTiO_3$ with *Amm2* space group [89]

Name	Element	X	Y	Z	Wyck.
O(1)	O	0.50000	0.25610	0.23430	4e
O(2)	O	0.00000	0.00000	0.48900	2a
Ti	Ti	0.50000	0.00000	0.51700	2b
Ba	Ba	0.00000	0.00000	0.00000	2a

3.5 Rhombohedral $BaTiO_3$

Below -90ºC barium titanate is known to have rhombohedral crystal structure with *R3m* space group. The lattice parameters of unit cell are a=b=c=4.004 Å with angles α=β=γ=89.836° [89]. Fractional atomic positions for rhombohedral $BaTiO_3$ are listed in Table 3.5. The rhombohedral crystal structure is formed by tilting of the TiO_6 octahedra about each axes (a, b and c) (Figure 3.5).

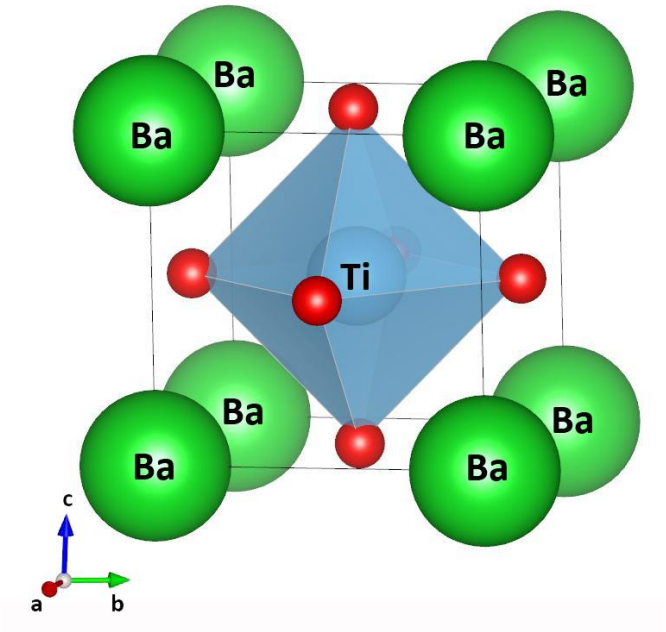

Figure 3.5. Schematic presentation of the unit cell of rhombohedral BaTiO3 crystal structure with the equivalent crystallographic sites annotated as Ti and Ba. The red spheres are oxygen atoms.

Table 3.5. Fractional atomic positions for rhombohedral $BaTiO_3$ with *R3m* space group [89].

Element	X	Y	Z	Wyck.
O	0.511300	0.511300	0.020000	3b
Ti	0.489300	0.489300	0.489300	1a
Ba	0.00000	0.00000	0.00000	1a

4 EXPERIMENTAL METHODS

4.1 Synthesis

The Fe-doped $BaTiO_3$ samples with a general formula of $BaTi_{1-x}Fe_xO_{3-\delta}$ (x=0.1, 0.2) were synthesized by the solid-state reaction method in two synthesis steps. During the first synthesis step, high purity $BaCO_3$ (99.8 % purity, Alfa Aesar), TiO_2 (99.9 % purity, Sigma-Aldrich) and Fe_2O_3 (99.945 % purity, Alfa Aesar) were homogenized by high energy milling in a planetary mill using yttria-stabilized zirconia balls and jar. After 1h of the milling in ethanol medium at 200 rpm the powders were dried at 70°C. The dried powders were pressed into 3-4 g pellets in a stainless steel die under a load of $8 \cdot 10^6\ Pa$. The pellets were fired at 1000°C for 5 h with 8°C/min heating and cooling rates. After initial firing, the pellets were crushed and thoroughly ground in the planetary mill under the same conditions as before. The powders were pressed into pellets and twice fired at 1250°C for 5h with intermediate grinding in the planetary mill.

To investigate the effect of annealing time on the magnetic properties of the Fe-doped $BaTiO_3$, the powders obtained after the first synthesis step were divided into five parts and four of them were additionally annealed at 1500°C (second synthesis step) for 1h, 3h, 5h and 10h, while the remaining part was not additionally annealed. In this way we obtained a set of five different samples for each doping concentration denoted as Batch 1.

In addition, another batch (Batch 2) of the 20% Fe-doped $BaTiO_3$ samples was synthesized to study the effect of extended annealing at 1500°C and re-annealing at lower temperature (1250°C). For this batch, the powder, obtained after first synthesis step, was divided into three parts. Two of them were additionally annealed at 1500°C (second synthesis step) for 10h and 50h. The powder treated at 1500°C for 10h was further divided into two parts. One part was re-annealed at 1250°C for 10h (third synthesis step) and the other was not re-annealed. The Batch 2 therefore consisted of a set of four different samples of 20% Fe-doped $BaTiO_3$ samples.

To summarize, we synthesised five samples of 10% Fe-doped $BaTiO_3$ and nine samples of the 20% Fe-doped $BaTiO_3$ treated at different annealing temperatures and time. All the heat treatments were carried out in oxygen atmosphere.

The samples (listed in Table 4.1) are denoted by abbreviated names, which indicate the specific parameters of their composition and synthesis. For example, the abbreviated name "10FBTO_15(3)_B1" refers to 10% Fe-doped $BaTiO_3$ sample, which was additionally annealed at 1500°C for 3h in the Batch 1. The 20% Fe-doped $BaTiO_3$ sample of the Batch 2, additionally annealed at 1500°C for 10h and re-annealed at 1250°C for 10h in the third synthesis step is denoted as "r(20FBTO_15(10)_B2)".

Undoped $BaTiO_3$, as a reference sample, was synthesized by the solid state reaction method by stoichiometric mixing of raw oxide materials of $BaCO_3$ (99.8 % purity, Alfa Aesar) and TiO_2 (99.9 % purity, Sigma-Aldrich). Before each heat treatment the sample was homogenized in the planetary mill at 200 rpm for 1 h in ethanol, dried at 70ºC and pressed into 3-4 g pellets. The pellets were calcined at 1000ºC for 5 h and then fired at 1250°C for 5 h. All the heat treatments were carried out in the nitrogen atmosphere.

Table 4.1. Heat treatment details of the second and third synthesis steps for 10% and 20% Fe-doped $BaTiO_3$ samples.

sample's name	**Second synthesis step**		**Third synthesis step**	
	T (ºC)	**t (h)**	**T (ºC)**	**t (h)**
10% Fe-doped $BaTiO_3$ (Batch 1)				
10FBTO_12(5)_B1	-	-	-	-
10FBTO_15(1)_B1	1500	1	-	-
10FBTO_15(3)_B1	1500	3	-	-
10FBTO_15(5)_B1	1500	5	-	-
10FBTO_15(10)_B1	1500	10	-	-
20% Fe-doped $BaTiO_3$ (Batch 1)				
20FBTO_12(5)_B1	-	-	-	-
20FBTO_15(1)_B1	1500	1	-	-
20FBTO_15(3)_B1	1500	3	-	-
20FBTO_15(5)_B1	1500	5	-	-
20FBTO_15(10)_B1	1500	10	-	-
20% Fe-doped $BaTiO_3$ (Batch 2)				
20FBTO_12(5)_B2	-	-	-	-
20FBTO_15(10)_B2	1500	10	-	-
r(20FBTO_15(10)_B2)	1500	10	1250	10
20FBTO_15(50)_B2	1500	50	-	-

4.2 X-Ray Powder Diffraction

For the phase analysis the X-ray diffraction patterns were taken with PANalytical X'PRO powder diffractometer in reflection (Bragg-Brentano) mode using Cu Kα radiation. The X-ray tube was operated at 45 kV and 40 mA at room temperature with distant focus-divergence slit of 100 mm and 0.1 mm receiving slit. Samples for XRD analysis were prepared using the back-loading technique. Data were collected on X'Celerator detector. The XRD measurements were carried out at two different laboratories. Because of this the measurement conditions are slightly different for samples from different batches. The XRD measurements for samples of Batch 1 were performed at the Centre of Excellence for Biosensors, Instrumentation and Process Control (COBIK) in Ajdovščina (Slovenia). For samples of Batch1 the data were collected in the range of $15° \leq 2\theta \leq 90°$, with the scan step of 0.008° and counting step time of 25. The XRD measurements for samples of Batch 2 were performed at the Laboratory for Inorganic Chemistry and Technology of National Institute of Chemistry in Ljubljana (Slovenia). For samples of Batch 2 the data were collected in the range of $5° \leq 2\theta \leq 70°$ with the scan step of 0.033°, counting step time of 100 s. The XRD spectra were recorded in a continuous scanning mode. The unit cells were determined by Rietveld profile refinement using HighScore plus software.

4.3 Magnetic measurements

All magnetic measurements of the finely powdered samples were performed with a vibrating sample magnetometer (VSM, LakeShore, 7307) at the Advanced Materials Department of Jožef Stefan Institute in Ljubljana (Slovenia). On Figure 4.1 the schematic view of the VSM is shown [90, 91]. A sample in VSM sinusoidally vibrates up and down in a uniform magnetic field. The movement of the sample leads to the change in the magnetic flux, which is sensed by pick-up coils. The magnetic characterization of the samples was carried out at room temperature with maximum applied field up to 12 kOe ($9.55 \cdot 10^5 \frac{A}{m}$) and 10^{-6} emu ($10^{-9}\mathrm{Am}^2$) sensitivity.

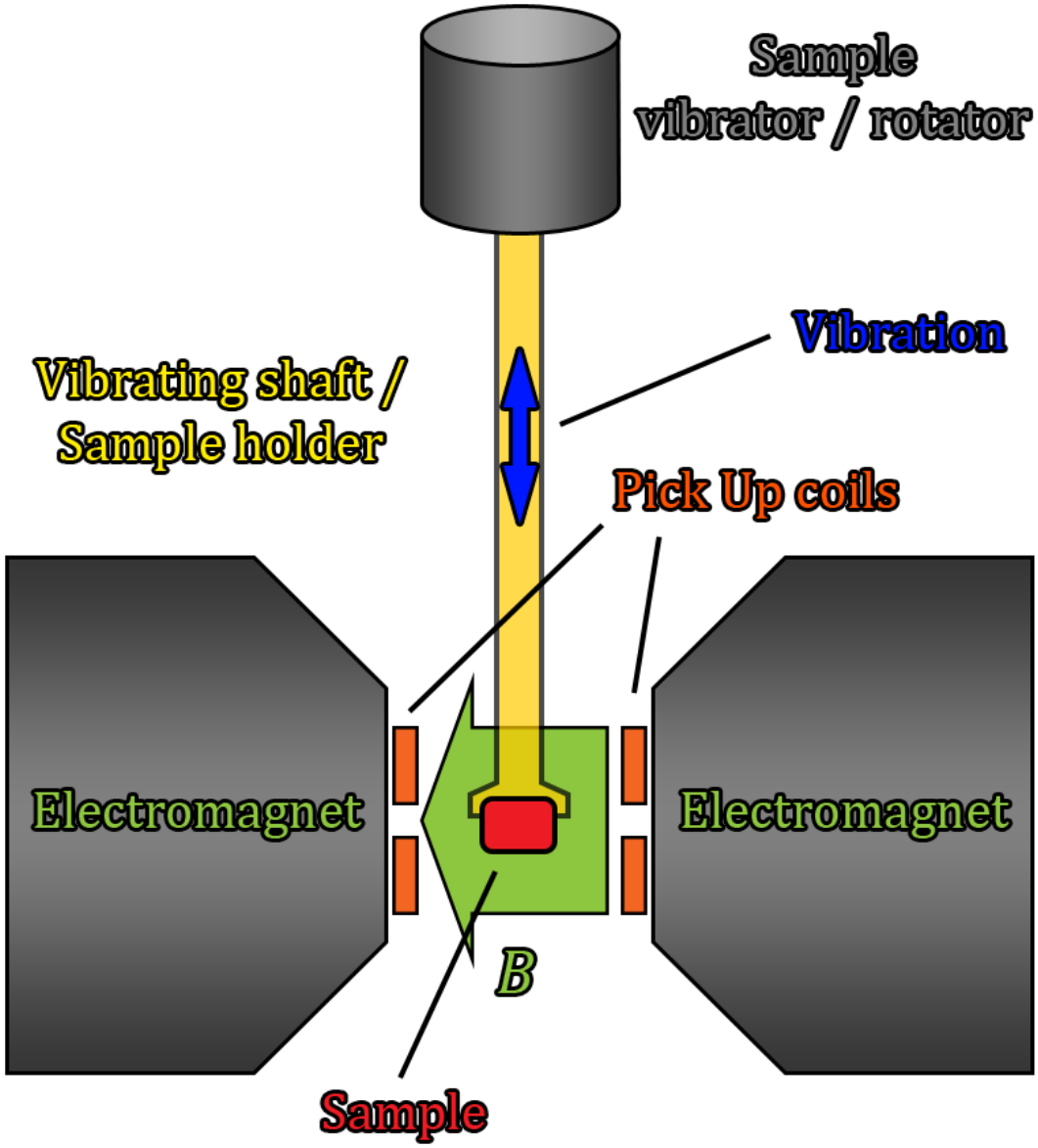

Figure 4.1. The schematic view of the vibrating sample magnetometer.

4.4 X-ray absorption experiment

The Fe K-edge XAS spectra were measured in fluorescence detection mode and Ti K-edge spectra were measured in transmission mode at the beamline C of HASYLAB at DESY in Hamburg (Germany), at the XAFS beamline of ELETTRA synchrotron radiation facility in Trieste (Italy) and at the BM23 beamline of European Synchrotron Radiation Facility (ESRF) in Grenoble (France). The samples were prepared in the form of homogeneous pellets, pressed from mixture of

micronized sample and boron nitride powders, with the total absorption thickness of about 2.5 above the investigated (Fe or Ti) K-edge. A Si (111) double-crystal monochromator was used, with energy resolution at Fe K-edge (7112 eV) of about 1 eV at C beamline of HASYLAB, 0.7 eV at XAFS beamline of Elettra and at BM23 beamline of ESRF. Higher order harmonics were effectively eliminated by detuning of the monochromator crystals to 60% of the rocking curve maximum, using the beam-stabilization feedback control. At C beamline the intensity of the x-ray beam was measured by three consecutive 10 cm long ionization detectors, filled with 30 mbar Ar and 650 mbar N_2; 380 mbar Ar; 580 mbar Ar, respectively. At XAFS beamline 30 cm long ionization detectors were used, filled with gas mixtures: N_2 at 580 mbar and He at 1420 mbar; Ar at 90 mbar, N_2 at 910 mbar and He at 1000 mbar; Ar at 350 mbar, N_2 at 650 mbar and He at 1000 mbar, respectively. At BM23 beamline three 30 cm long ion chambers were filled with follow gases: 630 mbar N_2, 130 mbar Ar and 200 mbar Ar, respectively. For Ti K-edge the three ionization chambers at XAFS beamline were filled with the following gas mixtures: N_2 at 200 mbar and He at 1800 mbar; N_2 at 900 mbar and He at1100 mbar; Ar at 140 mbar N_2 at 1000 mbar and He at 860 mbar, respectively.

The samples were mounted on the sample holder placed between the first and second ionisation detectors (in case of Fe K-edge spectra rotated by 45° to allow fluorescence detection). The fluorescence signal was detected with a silicon drift diode detector (80 mm^2) with a Be window at C beamline of HASYLAB and XAFS beamline of ELETTRA, while at BM23 beamline of ESRF the 13-element Ge detector was used. The self-absorption effect in fluorescence spectra was negligible. In all of the experiments, the exact energy calibration was established with simultaneous absorption measurements on 5 μm-thick Fe or Ti metal foil, placed between the second and third ionisation chambers. The absolute energy reproducibility of the measured spectra was ±0.1 eV or better.

The absorption spectra were measured within the interval [-250 eV to 1000 eV] relative to the Fe K-edge, and [-250 eV to 120 eV] relative to the Ti K-edge. In the XANES region equidistant energy steps of 0.3 eV were used, while for the EXAFS region equidistant k-steps of 0.05 $Å^{-1}$ were adopted, with an integration time of 1 s/step for the Ti K-edge and 5 s/step for the Fe K-edge spectra. In case of Fe K-edge

spectra the data of three to ten identical runs were superposed to improve the signal-to-noise ratio and to check the stability and reproducibility of the detection system. The Fe and Ti XAS spectra were analysed with the IFEFFIT program package [92].

5 STRUCTURAL AND MAGNETIC CHARACTERIZATION OF THE Fe-DOPED $BaTiO_3$

5.1.X-Ray Diffraction

A detailed XRD analysis was performed for phase identification of all samples. Figure 5.1 and Figure 5.2 show the XRD patterns of the 10% and 20% Fe-doped $BaTiO_3$. XRD pattern of the 10% Fe-doped $BaTiO_3$ sample fired at 1250ºC (10FBTO_12(5)_B1) indicates the presence of the tetragonal perovskite (*P4mm*) and prevailing hexagonal 6H (*P63/mmc*) phases (Figure 5.1). For other samples only the 6H-$BaTiO_3$ (*P63/mmc*) phase was observed (Figure 5.1 and Figure 5.2). Undoped $BaTiO_3$ reference sample shows a single phase composition with only tetragonal perovskite $BaTiO_3$ phase (Figure 5.1).

Based on the measured XRD patterns we have determined the unit cell parameters of the samples by Rietveld profile refinement using HighScore plus software (Table 5.1). The standard deviation of the calculated unit cell parameters was ± 0.004 Å. We observed that the c unit cell parameter slightly increased with Fe-doping of $BaTiO_3$ samples compared to the undoped $BaTiO_3$ sample (Figure 5.3). After the heat treatment of the 20% Fe-doped $BaTiO_3$ at 1500^{o}C an additional increase in the c unit cell parameter was observed, while for 10% Fe-doped $BaTiO_3$ this has not been observed and the unit cell remained unchanged. The c unit cell parameter of 20% Fe-doped $BaTiO_3$ re-annealed at 1250^{o}C (r(20FBTO_15(10)_B2)) decreased to about the same value as after initial treatment at 1250^{o}C.

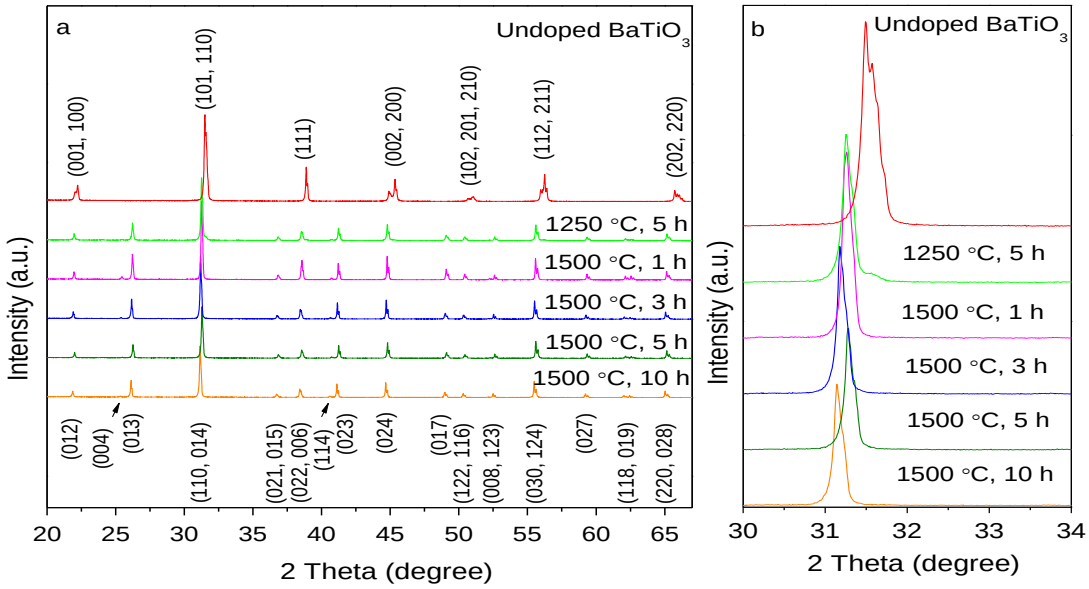

Figure 5.1. (a) X-ray diffraction patterns of 10% Fe-doped 6H-$BaTiO_3$ powder samples treated at different annealing temperatures (1250°C and 1500°C) for different length of time (1h, 3h, 5 h and 10 h). The peaks of tetragonal (top) and hexagonal (bottom) $BaTiO_3$ are labelled with Miller indices (hkl). (b) Magnification of diffraction peaks in the 2θ interval 30º - 34º, which shows the effect of annealing temperature on the phase evolution of 10% Fe-doped $BaTiO_3$. The XRD patterns are displaced vertically for clarity.

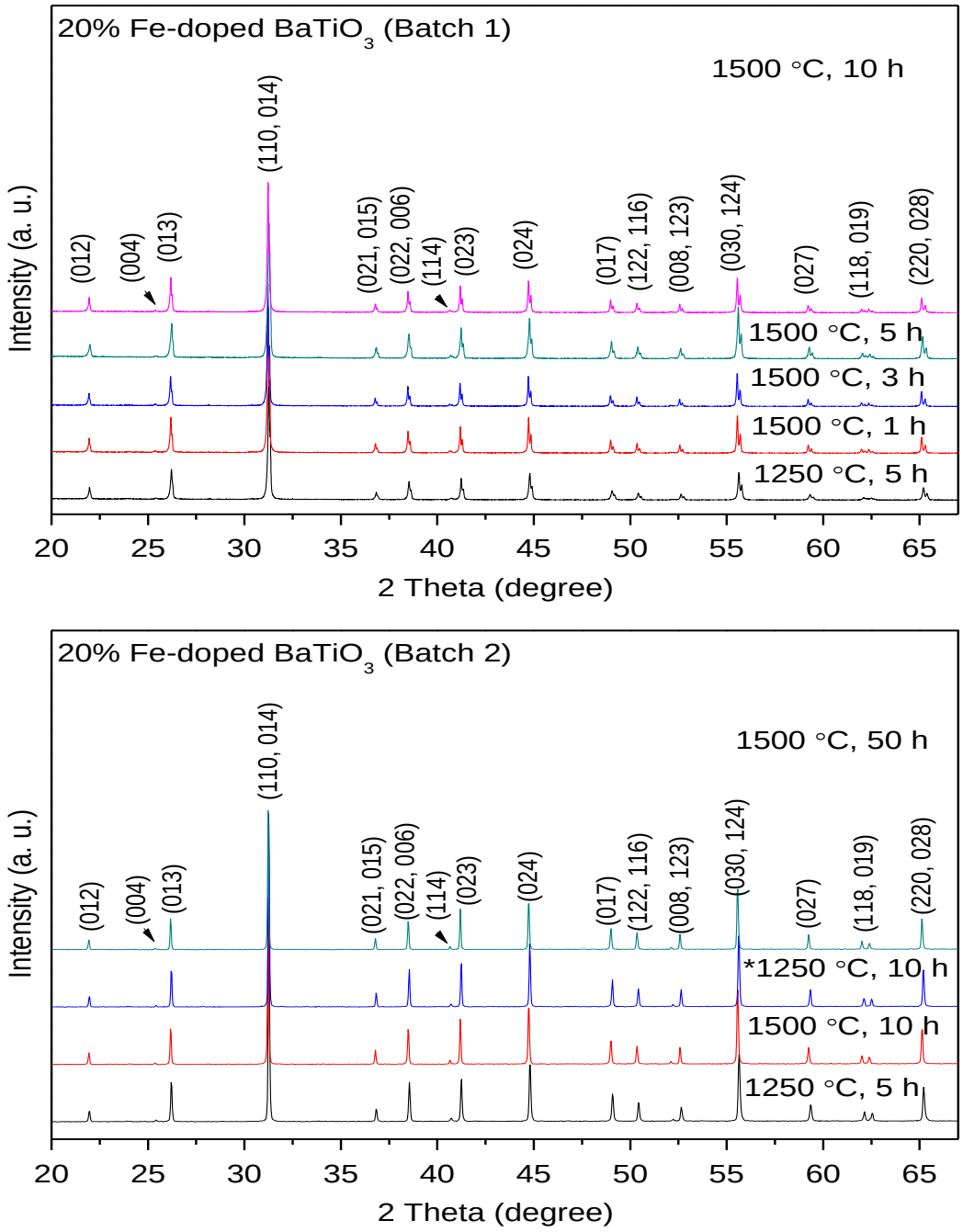

Figure 5.2. X-ray diffraction patterns of the 20% Fe-doped 6H-$BaTiO_3$ powder samples treated at different annealing temperatures (1250°C and 1500°C) for different length of time (1h, 3h, 5 h and 10 h, 50 h). The XRD patterns are displaced vertically for clarity. The 20% Fe-doped $BaTiO_3$ sample re-annealed at 1250 °C for 10h (r(20FBTO_15(10)_B2) is marked with asterisk.

Table 5.1. Lattice parameters of 10% and 20% Fe-doped $BaTiO_3$. The data for undoped 6H-$BaTiO_3$ are taken from Ref. [84].

sample's name	**a (Å)**	**c (Å)**
undoped $BaTiO_3$		
6H-$BaTiO_3$	5.724 (1)	13.965 (1)
$BaTiO_3$	3.996 (4)	4.031 (4)
10% Fe-doped $BaTiO_3$ (Batch 1)		
10FBTO_12(5)_B1	5.722 (4)	13.996 (4)
10FBTO_15(1)_B1	5.725 (4)	13.999 (4)
10FBTO_15(3)_B1	5.725 (4)	14.000 (4)
10FBTO_15(5)_B1	5.725 (4)	14.002 (4)
10FBTO_15(10)_B1	5.724 (4)	13.997 (4)
20% Fe-doped $BaTiO_3$ (Batch 1)		
20FBTO_12(5)_B1	5.718 (4)	14.011 (4)
20FBTO_15(1)_B1	5.726 (4)	14.036 (4)
20FBTO_15(3)_B1	5.726 (4)	14.035 (4)
20FBTO_15(5)_B1	5.725 (4)	14.033 (4)
20FBTO_15(10)_B1	5.726 (4)	14.036 (4)
20% Fe-doped $BaTiO_3$ (Batch 2)		
20FBTO_12(5)_B2	5.718 (4)	13.999 (4)
20FBTO_15(10)_B2	5.725 (4)	14.034 (4)
r(20FBTO_15(10)_B2)	5.720 (4)	14.006 (4)
20FBTO_15(50)_B2	5.725 (4)	14.034 (4)

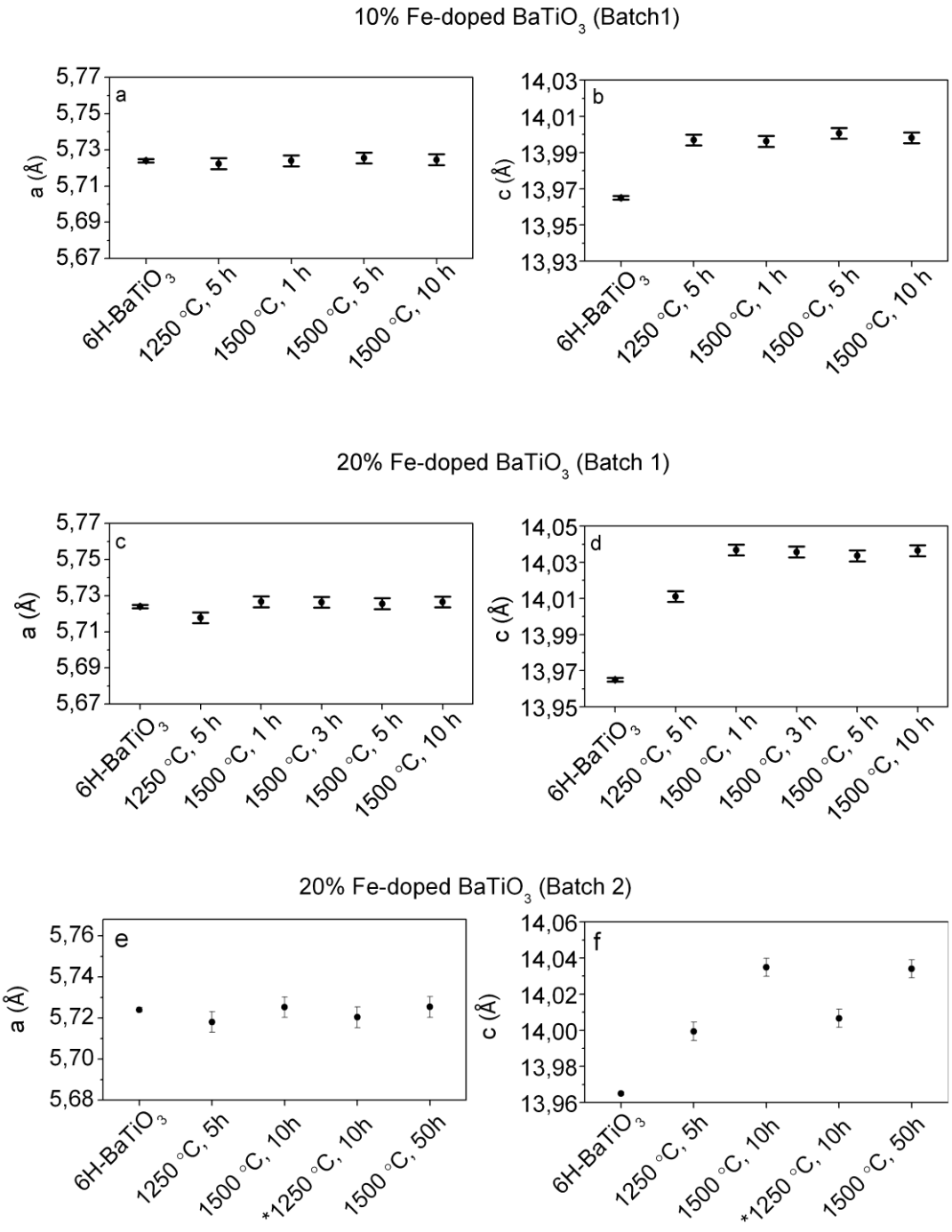

Figure 5.3. Unit-cell parameters (a and c axes) of the 10% and 20% Fe-doped $BaTiO_3$ (Batch 1 and Batch 2) samples treated at different annealing temperatures (1250°C and 1500°C) for different length of time (1h, 3h, 5 h and 10 h, 50 h). The a and c unit-cell axes are plotted on the graph with the same scale for comparison. The 20% Fe-doped $BaTiO_3$ sample re-annealed at 1250 °C for 10h (r(20FBTO_15(10)_B2) is annotated with asterisk. The first point on the plots represents unit cell parameters for undoped 6H-$BaTiO_3$ from Ref. [84].

5.2.Magnetic measurements

Magnetization of all Fe-doped $BaTiO_3$ samples as function of an applied external magnetic field was measured on the vibrating sample magnetometer at room temperature. To compare our results with recently published data [44, 48-51, 65] the as-measured magnetization values were converted to Bohr magnetons and normalised per Fe atom using equation (2.19) in Chapter 2. (Figure 5.4).

A shape of the magnetization curves gives information about possible magnetic phases present in the sample [78, 79]. The magnetic measurements reveal that all the samples obtained after the first synthesis step and 10% Fe-doped $BaTiO_3$ sample treated at 1500 ºC for 1h (10FBTO_15(1)_B1) are paramagnetic, while the other, additionally annealed at 1500°C, exhibit ferromagnetic behaviour (Figure 5.4). However, in all ferromagnetic samples the magnetization does not reach saturation indicating the coexistence of ferromagnetic and paramagnetic states.

The hysteresis loops of 10% Fe-doped $BaTiO_3$ samples exhibit a different shape compared with 20% Fe-doped $BaTiO_3$ samples: the hysteresis loops of 10% Fe-doped $BaTiO_3$ are constricted in the middle. This is so called “wasp-waisted” hysteresis loop, the origin of which can be attributed to the competing ferromagnetic and antiferromagnetic interactions (Figure 5.4) [78].

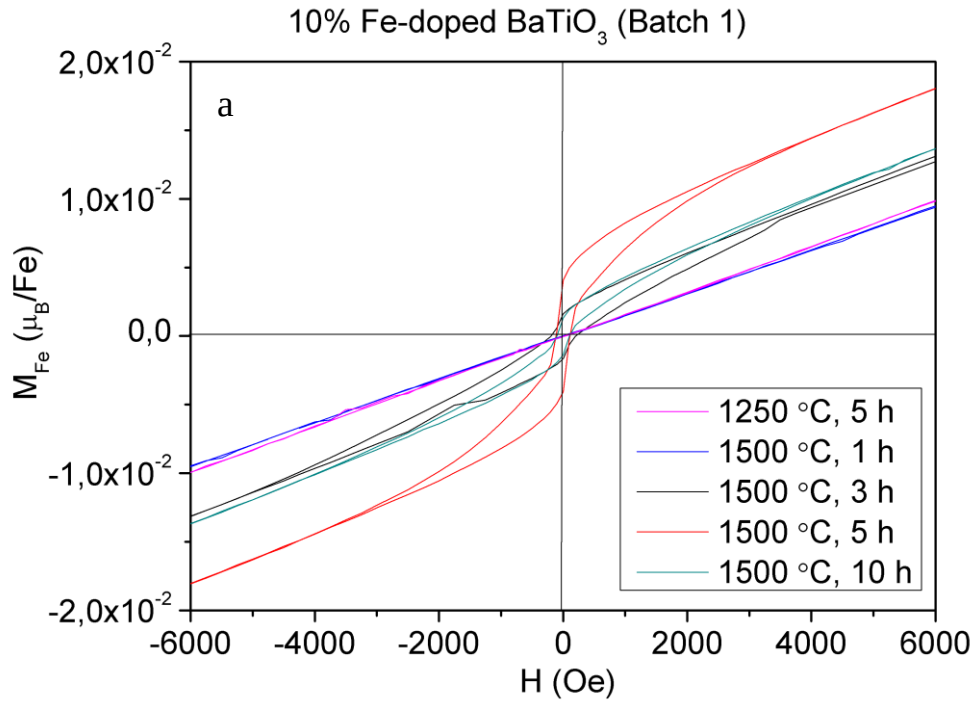
10% Fe-doped BaTiO3 (Batch 1)
a
2,0x10-2
1,0x10-2
0,0
-1,0x10-2
-2,0x10-2
MFe (μB/Fe)
-6000
-4000
-2000
0
2000
4000
6000
H (Oe)
1250 °C, 5 h
1500 °C, 1 h
1500 °C, 3 h
1500 °C, 5 h
1500 °C, 10 h

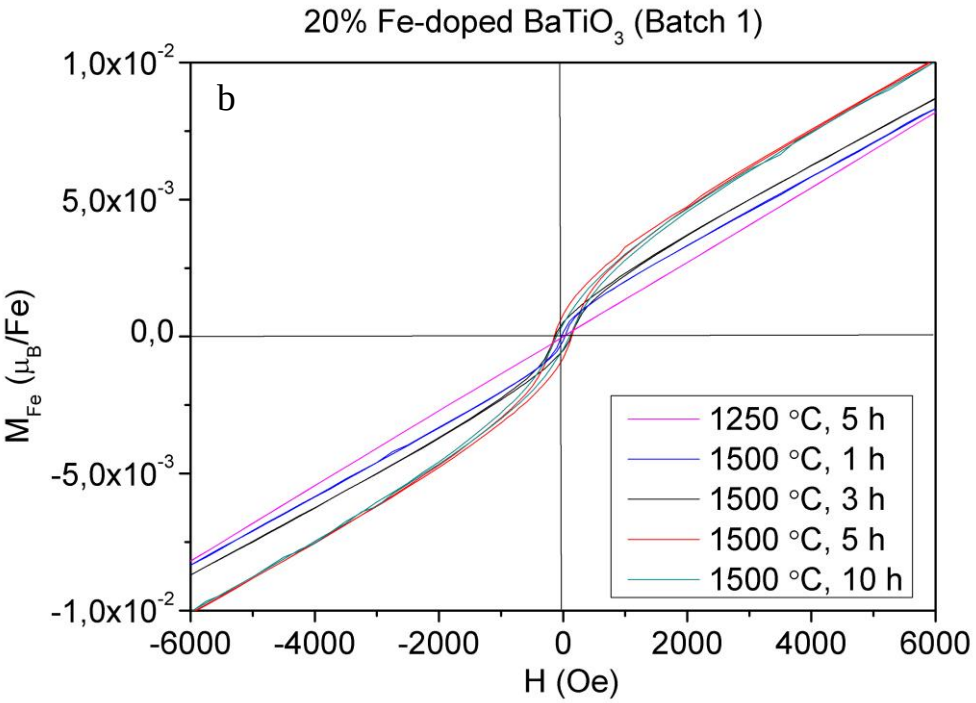
20% Fe-doped BaTiO3 (Batch 1)
b
1,0x10-2
5,0x10-3
0,0
-5,0x10-3
-1,0x10-2
MFe (μB/Fe)
-6000
-4000
-2000
0
2000
4000
6000
H (Oe)
1250 °C, 5 h
1500 °C, 1 h
1500 °C, 3 h
1500 °C, 5 h
1500 °C, 10 h

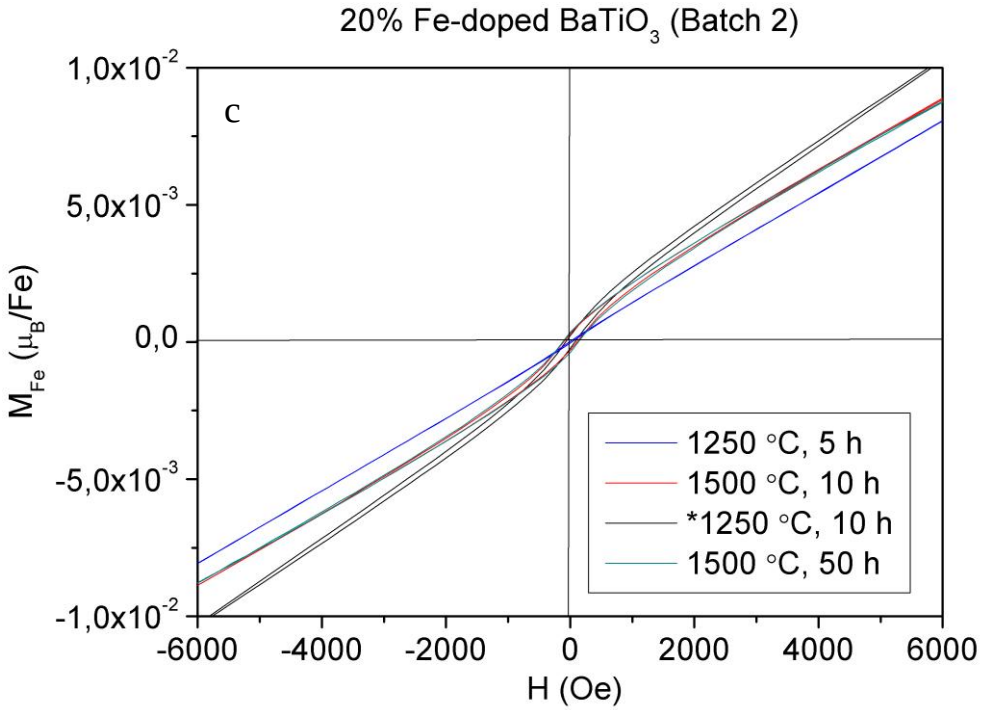

Figure 5.4. The magnetization ($\boldsymbol{M_{Fe}}$) as function of an external applied magnetic field ($\boldsymbol{H}$) measured at room-temperature for 10% (a) and 20% (b and c) Fe-doped 6H-$BaTiO_3$ samples treated at different annealing temperatures (1250°C and 1500°C) for different length of time (1h, 3h, 5 h, 10 h and 50 h). The 20% Fe-doped $BaTiO_3$ re-annealed at 1250°C for 10h sample (r(20FBTO_15(10)_B2) is annotated with asterisk.

The samples obtained after first synthesis step and 10% Fe-doped $BaTiO_3$ sample treated for 1h (10FBTO_15(1)_B1) exhibit paramagnetic behaviour, while the rest of the samples subsequently annealed at 1500°C exhibit ferromagnetic behaviour. However, for all ferromagnetic samples the magnetization does not reach saturation indicating a superposition of ferromagnetic and paramagnetic states.

With intention to analyse the ferromagnetic properties of the samples, the so-called slope correction of hysteresis loops was carried out. The tangent of the slope of the linear part of the hysteresis loop corresponds to the magnetic susceptibility χ_{Fe} [79]. Thus, the line $M = \chi_{Fe}H$ passed through the origin represents the paramagnetic contribution and was subtracted from as-measured hysteresis loops to obtain the ferromagnetic component (Figure 5.5).

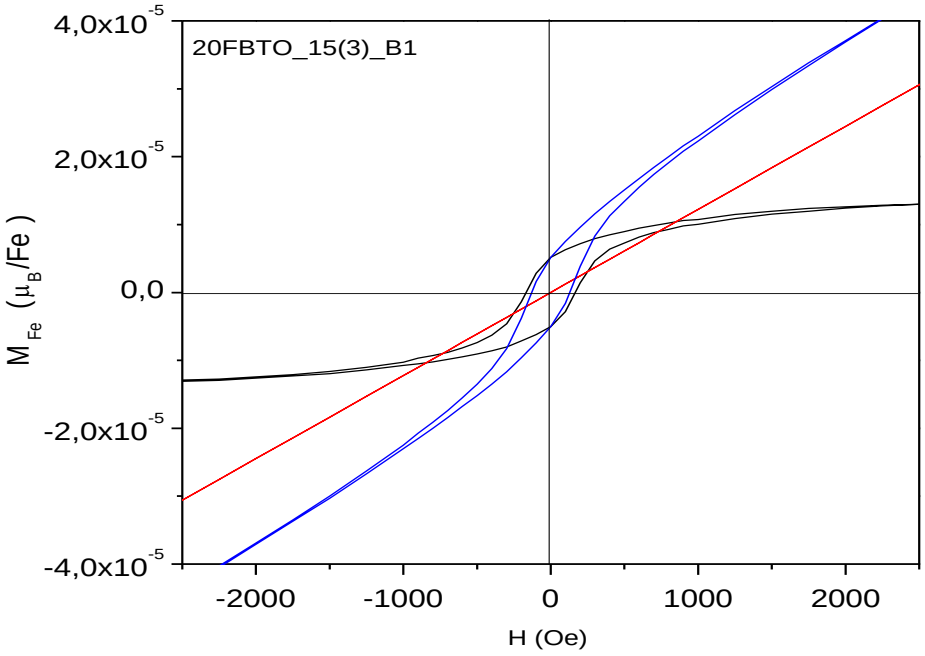

Figure 5.5. Slope corrected hysteresis loop for 20% Fe-doped $BaTiO_3$ additionally annealed at 1500ºC for 3h (20FBTO_15(3)_B1). Blue line is as-obtained hysteresis loop; red line – paramagnetic contribution, black line – ferromagnetic contribution.

The magnetic susceptibility values are listed in the Table 5.2. The magnetic susceptibility was found to be higher for 10% than 20% Fe doping. No variations in the magnetic susceptibility were observed after the heat treatment at higher temperatures.

The slope-corrected room-temperature magnetization curves for 10% and 20% Fe-doped 6H-$BaTiO_3$ are shown in the Figure 5.6. The saturation magnetization M_S was determined by extrapolation of the linear part of the slope-corrected magnetization curves to zero magnetic field. The saturation magnetization values are listed in the Table 5.2. M_S decreases with increasing Fe content. The saturation magnetization as function of annealing time for 10% and 20% Fe-doped $BaTiO_3$ samples annealed at 1500^{o}C is shown in Figure 5.7. M_S gradually increases with increasing annealing time up to 5h (Figure 5.7). After further heat treatment at 1500^{o}C for 10h the saturation magnetization exhibits different behaviour for samples with different Fe content: the saturation magnetization decreases for 10% Fe-doped $BaTiO_3$ sample, while for the one with 20% of Fe remains unchanged.

Table 5.2. Magnetic susceptibility (χ_{Fe}) and saturation magnetization (M_S) for 10% and 20% Fe-doped $BaTiO_3$ samples treated at different annealing temperature (1250°C and 1500°C) time (1h, 3h, 5 h, 10 h and 50h).

Sample	χ_{Fe} $(*10^{-6})$	M_s $(*10^{-3}\frac{\mu_B}{Fe})$
10% Fe-doped $BaTiO_3$ (Batch 1)		
10FBTO_12(5)_B1	1.66 (7)	-
10FBTO_15(1)_B1	1.57 (7)	-
10FBTO_15(3)_B1	1.72 (7)	2.76 (14)
10FBTO_15(5)_B1	1.75(7)	7.58 (38)
10FBTO_15(10)_B1	1.73 (7)	3.31 (17)
20% Fe-doped $BaTiO_3$ (Batch 1)		
20FBTO_12(5)_B1	1.37 (7)	-
20FBTO_15(1)_B1	1.25 (7)	0.84 (4)
20FBTO_15(3)_B1	1.22 (7)	1.36 (7)
20FBTO_15(5)_B1	1.28 (7)	2.45 (12)
20FBTO_15(10)_B1	1.29 (7)	2.23 (11)
20% Fe-doped $BaTiO_3$ (Batch 2)		
20FBTO_12(5)_B2	1.32 (7)	-
20FBTO_15(10)_B2	1.29 (7)	1.16 (6)
r(20FBTO_15(10)_B2)	1.46 (7)	1.58 (8)
20FBTO_15(50)_B2	1.24 (7)	1.29 (7)

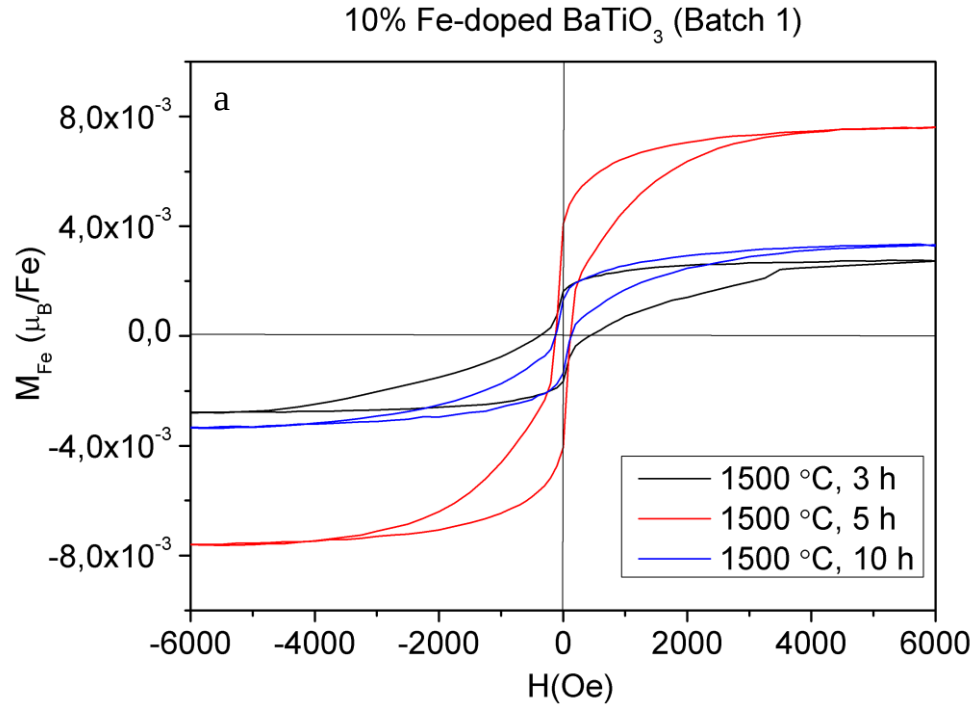
10% Fe-doped BaTiO3 (Batch 1)
a
8,0x10-3
4,0x10-3
0,0
-4,0x10-3
-8,0x10-3
MFe (μB/Fe)
-6000
-4000
-2000
0
2000
4000
6000
H(Oe)
1500 °C, 3 h
1500 °C, 5 h
1500 °C, 10 h

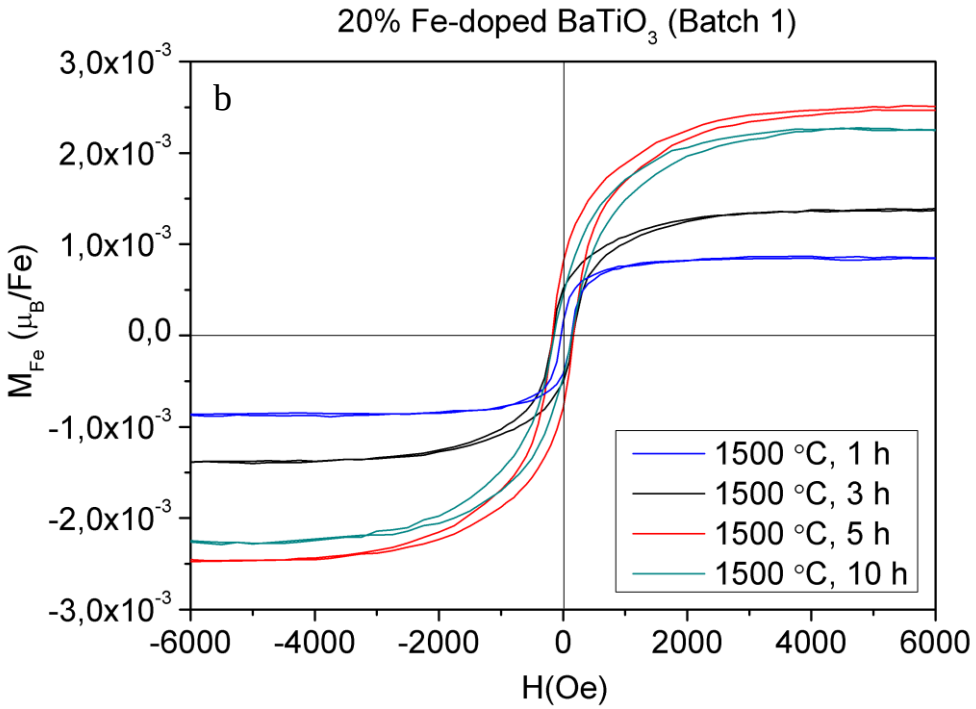
20% Fe-doped BaTiO3 (Batch 1)
b
3,0x10-3
2,0x10-3
1,0x10-3
0,0
-1,0x10-3
-2,0x10-3
-3,0x10-3
MFe (μB/Fe)
-6000
-4000
-2000
0
2000
4000
6000
H(Oe)
1500 °C, 1 h
1500 °C, 3 h
1500 °C, 5 h
1500 °C, 10 h

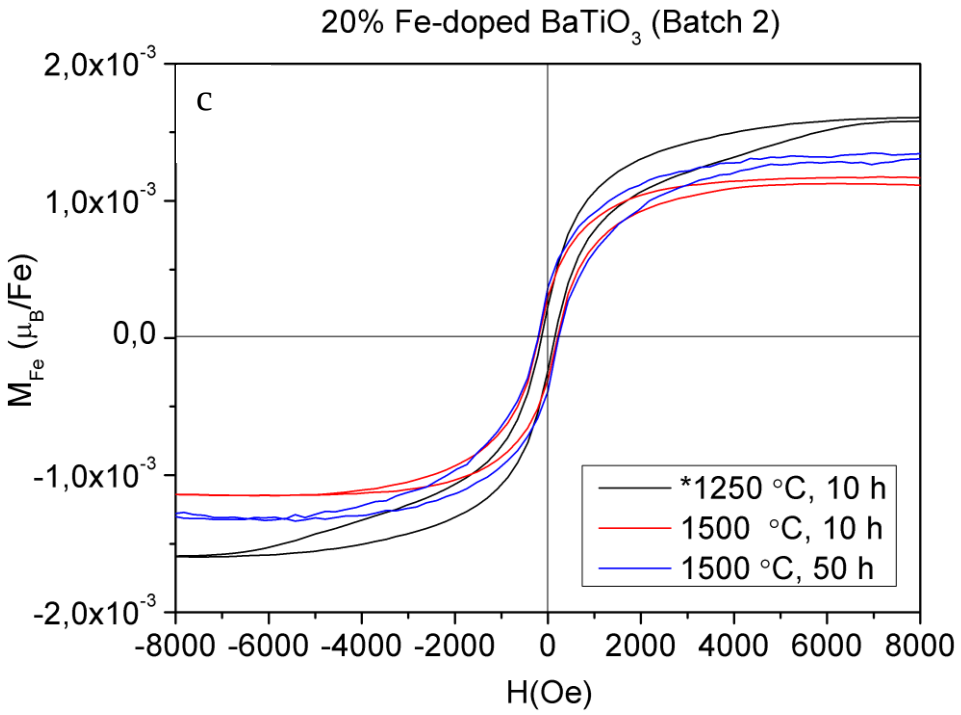

Figure 5.6. Slope-corrected room-temperature magnetization curves for 10% (a) and 20% (b and c) Fe-doped 6H-$BaTiO_3$ samples treated at 1500°C for different time (1h, 3h, 5 h and 10 h). The 20% Fe-doped $BaTiO_3$ sample re-annealed at 1250°C for 10h (r(20FBTO_15(10)_B2) is annotated with asterisk.

For 20% Fe-doped $BaTiO_3$ samples of Batch 2 we found that M_S slightly increased after additional annealing at 1250^{o}C for 10h (r(20FBTO_15(10)_B2), while after heat treatment at 1500^{o}C for 50h (20FBTO_15(50)_B2) it remained unchanged, compared with the saturation magnetization of the sample treated at 1500^{o}C for 10h (20FBTO_15(10)_B2).

A comparison of the saturation magnetizations of the 20% Fe-doped $BaTiO_3$ samples, treated at 1500^{o}C for 10h, from two different batches shows that the saturation magnetization of the 20FBTO_15(10)_B2 sample is about two times lower than saturation magnetization of the 20FBTO_15(10)_B1 sample. Such differences can be attributed to the differences in the synthesis parameters, which could not be precisely controlled, such as oxygen flow rate.

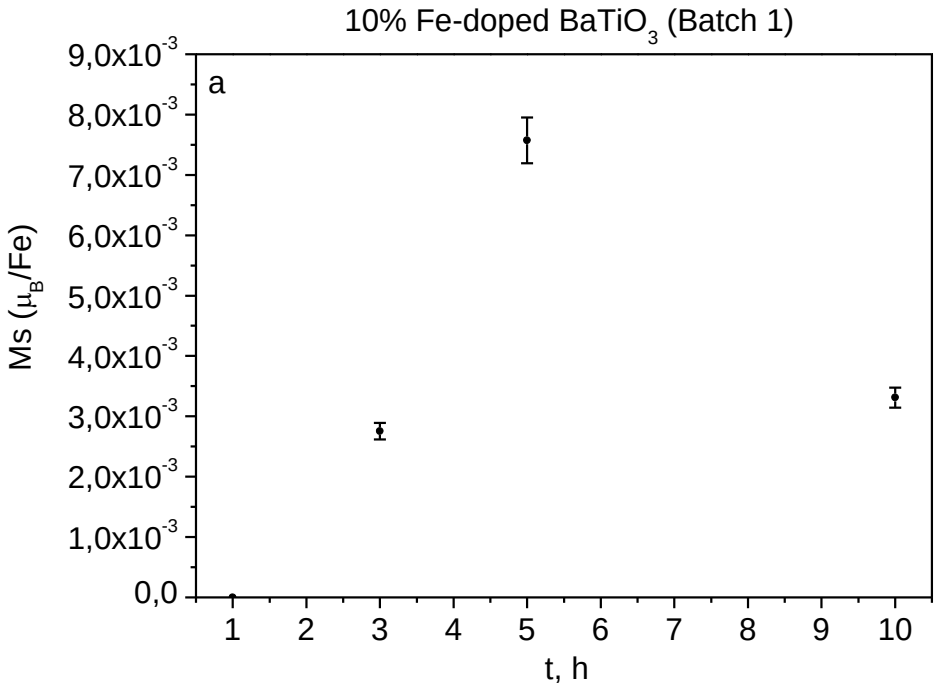
10% Fe-doped BaTiO3 (Batch 1)
a
Ms (μB/Fe)
9,0x10-3
8,0x10-3
7,0x10-3
6,0x10-3
5,0x10-3
4,0x10-3
3,0x10-3
2,0x10-3
1,0x10-3
0,0
1
2
3
4
5
6
7
8
9
10
t, h

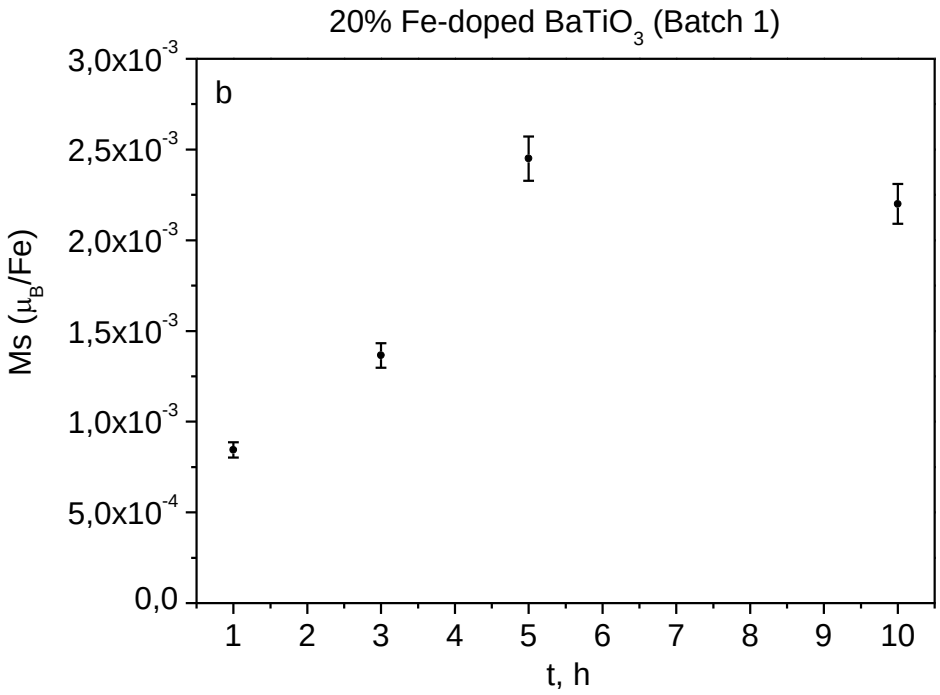
20% Fe-doped BaTiO3 (Batch 1)
b
Ms (μB/Fe)
3,0x10-3
2,5x10-3
2,0x10-3
1,5x10-3
1,0x10-3
5,0x10-4
0,0
1
2
3
4
5
6
7
8
9
10
t, h

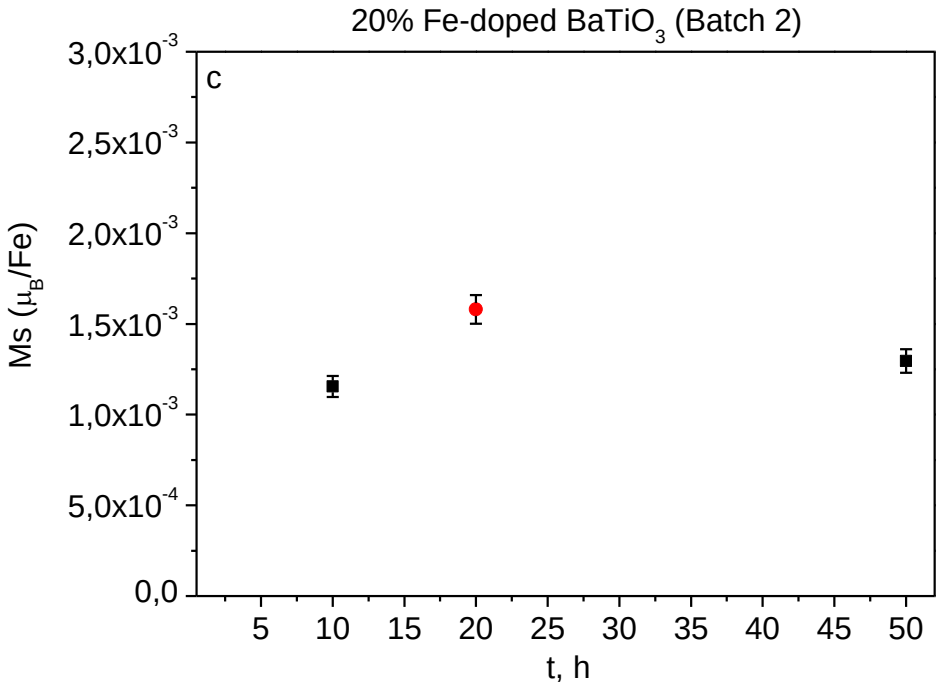

Figure 5.7. Saturation magnetization as a function of annealing time for 10% (a) and 20% (b and c) Fe-doped $BaTiO_3$ samples treated at 1500°C. The 10% Fe-doped $BaTiO_3$ sample treated for 1h (10FBTO_15(1)_B1) is paramagnetic, thus the saturation magnetization is equal to zero. The 20% Fe-doped $BaTiO_3$ sample re-annealed at 1250°C for 10h (r(20FBTO_15(10)_B2) is denoted by a red circle.

In a case when each Fe^{3+} ion in Fe-doped $BaTiO_3$ is in the high-spin state with $5\ \mu_B/Fe$ spin magnetic moment, the fraction of ferromagnetically coupled Fe atoms (N/N_{Fe}) in the Fe-doped $BaTiO_3$ can be estimated from the saturation magnetization values M_S:

$$\frac{\mathrm{N}}{N_{Fe}} = \frac{\mathrm{M}_S}{\mu_S^{Fe}} \cdot 100\%, \tag{5.1}$$

where N is number of ferromagnetically coupled Fe atoms, $N_{Fe} = N_A X_{Fe}$ is the total number of Fe atoms in the Fe-doped $BaTiO_3$ and $\mu_S^{Fe} = 5\ \mu_B/Fe$ is net spin magnetic moment of Fe^{3+} cation.

The results of the calculations for all ferromagnetic samples are presented in the Table 5.3. It is seen that only a tiny amount (about 0.05 %) of Fe ions are coupled

ferromagnetically, while the magnetic moments of the rest of the Fe ions contribute to paramagnetism.

Table 5.3. The fraction of ferromagnetically coupled Fe atoms in the Fe-doped $BaTiO_3$

Sample	$\frac{N}{N_{Fe}}$ **(%)**
10% Fe-doped $BaTiO_3$ (Batch 1)	
10FBTO_15(3)_B1	0.055 (3)
10FBTO_15(5)_B1	0.015 (1)
10FBTO_15(10)_B1	0.066 (3)
20% Fe-doped $BaTiO_3$ (Batch 1)	
20FBTO_15(1)_B1	0.017 (1)
20FBTO_15(3)_B1	0.027 (1)
20FBTO_15(5)_B1	0.049 (2)
20FBTO_15(10)_B1	0.044 (2)
20% Fe-doped $BaTiO_3$ (Batch 2)	
20FBTO_15(10)_B2	0.023 (1)
r(20FBTO_15(10)_B2)	0.032 (2)
20FBTO_15(50)_B2	0.026 (1)

5.3.XANES analysis

A shape and energy position of an absorption edge contains information about valence state of the absorbing atom and the local symmetry of its unoccupied orbitals. The valence state of the metal cations can be deduced from the energy position of the absorption edge: increasing of the valence state of the metal cations leads to the shift of the absorption edge to higher energies [24, 92-94]. Thus, we used Ti K-edge and Fe K-edge XANES analysis, as a precise tool to determine the average valence state of the Ti and Fe atoms, correspondingly. All Ti and Fe XANES spectra (Figure 5.8 and Figure 5.9) were normalised by a standard procedure implemented in the IFEFFIT [92] program package.

5.3.1. Ti K-edge XANES

Based on results of magnetic measurements, some representative samples (listed in Table 5.4) were selected for Ti K-edge XANES measurements. The Ti K-edge XANES spectra of all the 20% Fe-doped $BaTiO_3$ samples exhibit same shape and energy position of the Ti K-edge edge and pre-edge resonances (Figure 5.8). The Ti K-edge XANES profile of the undoped $BaTiO_3$ compound with tetragonal crystal structure, used as a reference for Ti^{4+} valence state, exhibits a slightly different shape of the edge, due to small differences in local structure around Ti cations in the two (tetragonal and hexagonal) crystal structures. However, the Ti K-edge energy position in XANES spectra of Fe-doped $BaTiO_3$ samples is the same as in the XANES spectrum of the undoped $BaTiO_3$ compound, which shows that all Ti cations in the samples are in Ti^{4+} valence state.

Table 5.4. The list of the samples, which have been used for Ti K-edge analysis.

Sample
10% Fe-doped $BaTiO_3$ (Batch 1)
10FBTO_12(5)_B1
10FBTO_15(1)_B1
10FBTO_15(3)_B1
10FBTO_15(10)_B1
20% Fe-doped $BaTiO_3$ (Batch 1)
20FBTO_12(5)_B1
20FBTO_15(1)_B1
20FBTO_15(5)_B1
20FBTO_15(10)_B1
undoped $BaTiO_3$
$BaTiO_3$

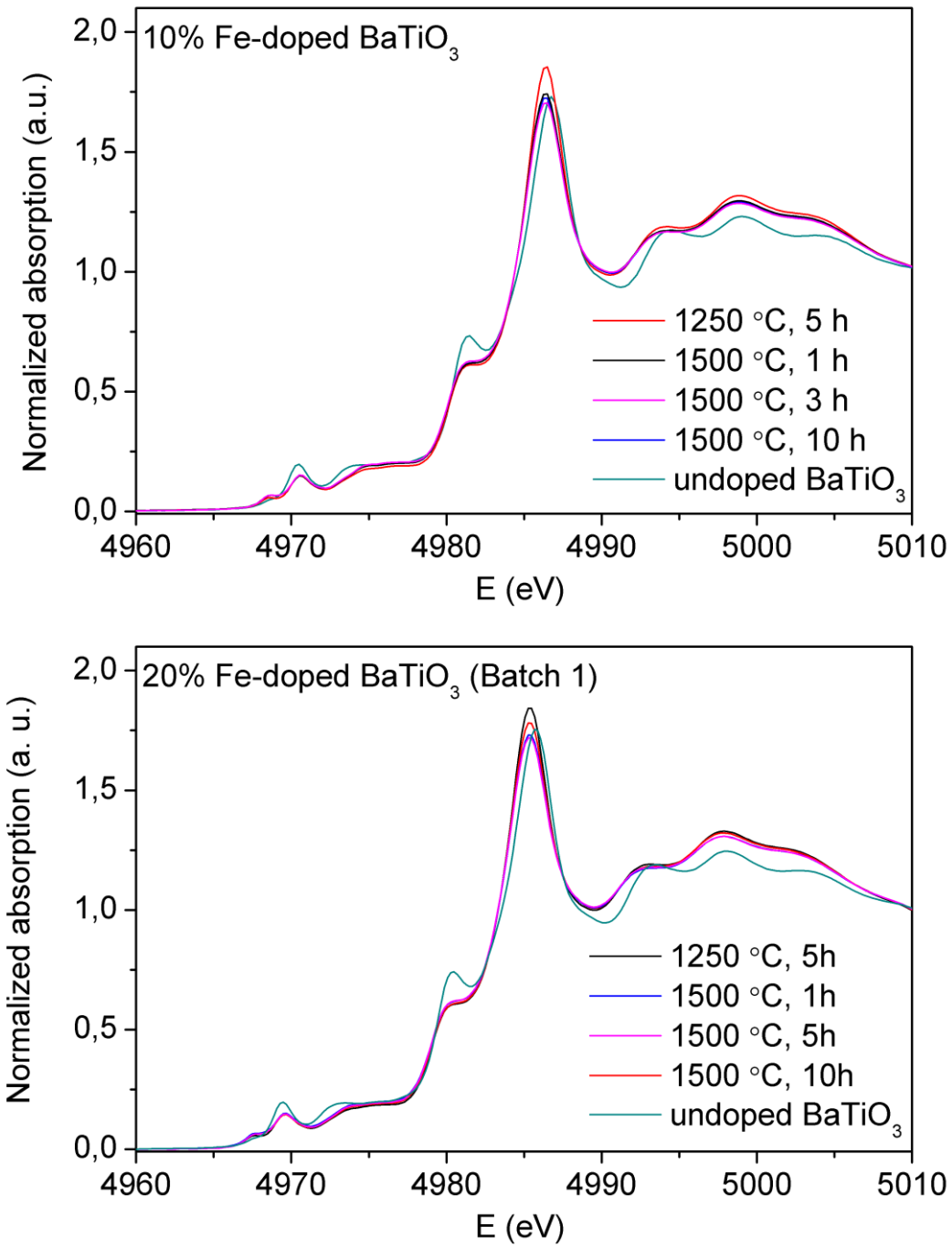

Figure 5.8. Normalized Ti K-edge XANES spectra measured on 10% and 20% Fe-doped 6H-$BaTiO_3$ (Batch 1) powder samples, treated at different annealing temperatures (1250°C and 1500°C) for different length of time (1h, 5 h and 10 h) in oxygen atmosphere, and undoped $BaTiO_3$ with tetragonal (*P4mm*) crystal structure as a standard for Ti^{4+}.

5.3.2. Fe K-edge XANES

Similar as for Ti K-edge XANES analysis, representative samples (listed in Table 5.5) were selected for Fe K-edge XANES and EXAFS analysis.

Table 5.5. The list of the samples, which have been used for Fe K-edge XANES and EXAFS analysis.

Sample
10% Fe-doped $BaTiO_3$ (Batch 1)
10FBTO_12(5)_B1
10FBTO_15(10)_B1
20% Fe-doped $BaTiO_3$ (Batch 1)
20FBTO_12(5)_B1
20FBTO_15(5)_B1
20FBTO_15(10)_B1
20% Fe-doped $BaTiO_3$ (Batch 2)
20FBTO_12(5)_B2
20FBTO_15(10)_B2
r(20FBTO_15(10)_B2)
20FBTO_15(50)_B2

It is worth to mention, that Fe K-edge XANES profile is very sensitive to changes in the Fe local neighbourhood [94-96]. Thus, structural changes around Fe ions, such as ordering of oxygen vacancies or pairing of Fe cations in one crystallographic site, may cause small shifts of the energy position of Fe K-edge XANES profile and the pre-edge lines.

The normalised Fe K-edge XANES spectra of all 10% and 20% Fe-doped $BaTiO_3$ samples exhibit similar shape and same energy position of the Fe K-edge and pre-edge resonances (Figure 5.9). The edge shape is in all cases characteristic for

octahedrally coordinated Fe cations [94]. XANES profiles of the samples treated at the same temperature, but with different concentration of iron are identical regardless the length of annealing time (Figure 5.10 and Figure 5.11). Small differences in the edge profile and intensity of the pre-edge resonances for samples treated at 1250°C and 1500°C (Figure 5.11) can be attributed to changes in average local environment of Fe cations, detected in the Fe K-edge EXAFS analysis and discussed in detail in the next chapter.

To deduce the average valence state of the Fe cations in the samples we compared the Fe K-edge energy positions of the samples with those measured on the reference compounds with similar octahedral symmetry of Fe cations and well established Fe^{3+} and Fe^{2+} valence states ($Fe(III)_2O_3$, $NdFe(III)O_3$, and $Fe(II)SO_4$) (Figure 5.9). A shift of about 4.5 eV is found between the spectra of the two- and three- valent iron compounds in agreement with previous observations [94, 97]. The energy positions of Fe K-edge in the Fe-doped $BaTiO_3$ samples coincides with the edge positions of the Fe^{3+} reference compounds, indicating that all iron in the samples is in trivalent form. XANES profile of the re-annealed sample (r(20FBTO_15(10)_B2)) can be completely described by a linear combination of the XANES spectra of 20% Fe-doped $BaTiO_3$ (Batch 2) samples, the one fired at 1250ºC for 5h (20FBTO_12(5)_B2) and the one additionally annealed at 1500ºC for 10 h (20FBTO_15(10)_B2), with the relative ratio of 34% : 66%. The quality of the fit is illustrated on the Figure 5.12. This result indicates that during the post annealing at 1250ºC system experiences changes in local structure around Fe atoms that bring the system towards the state after the first synthesis step (1250ºC for 5 h), before annealing at 1500ºC.

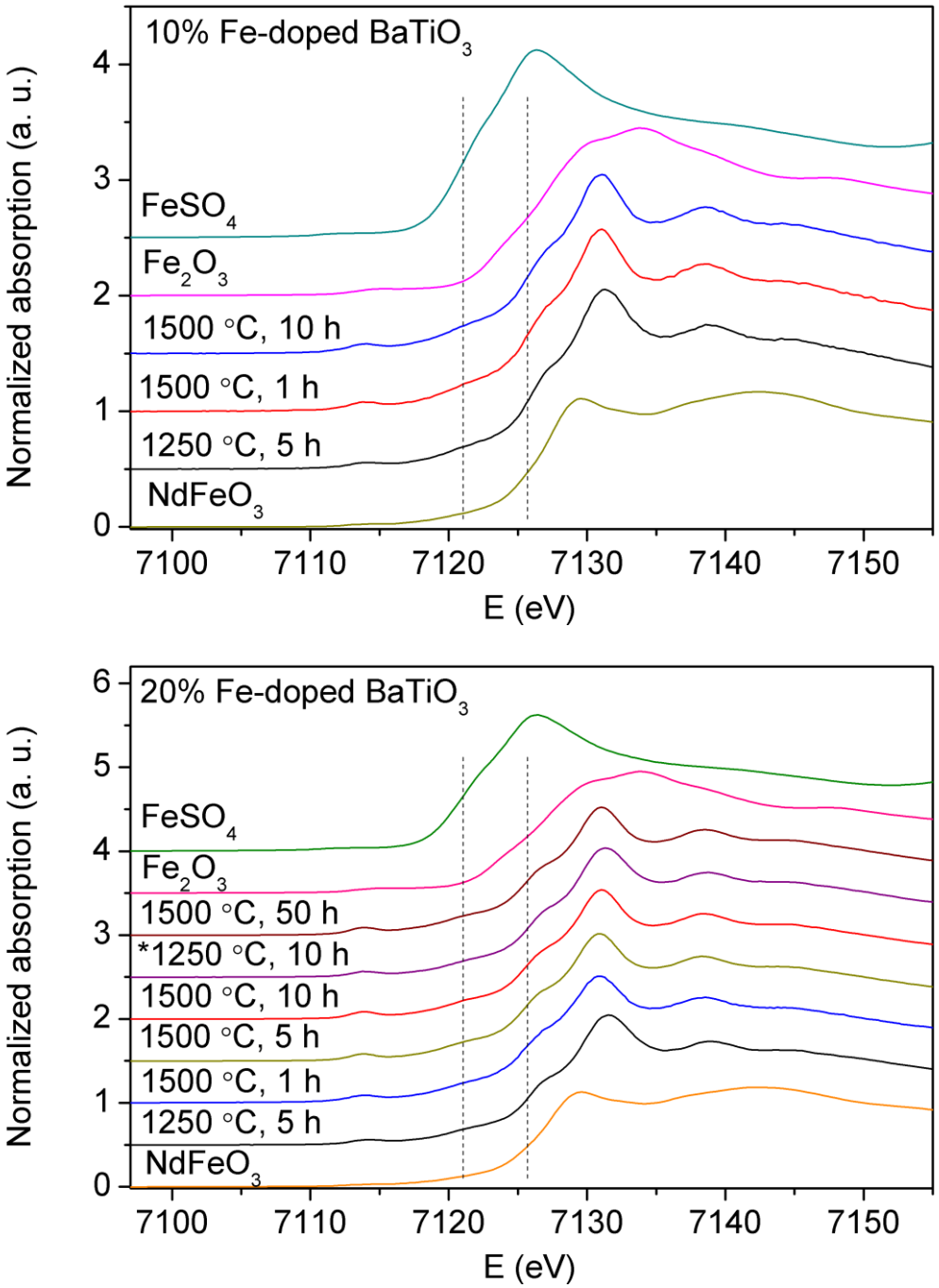

Figure 5.9. Normalized Fe K-edge XANES spectra measured on the 10% and 20% Fe-doped $BaTiO_3$ samples after different heat treatments, and reference compounds ($Fe(III)_2O_3$, $NdFe(III)O_3$, and $Fe(II)SO_4$) with known Fe valence state. The 20% Fe-doped $BaTiO_3$ sample re-annealed at 1250°C for 10h (r(20FBTO_15(10)_B2) was identified with asterisk. Two vertical lines are plotted at the position of the Fe(II) K-edge (7121 eV) and Fe(III) K-edge (7125.7 eV) to facilitate the comparison of the Fe K-edge position in the samples. The spectra are displaced vertically for clarity.

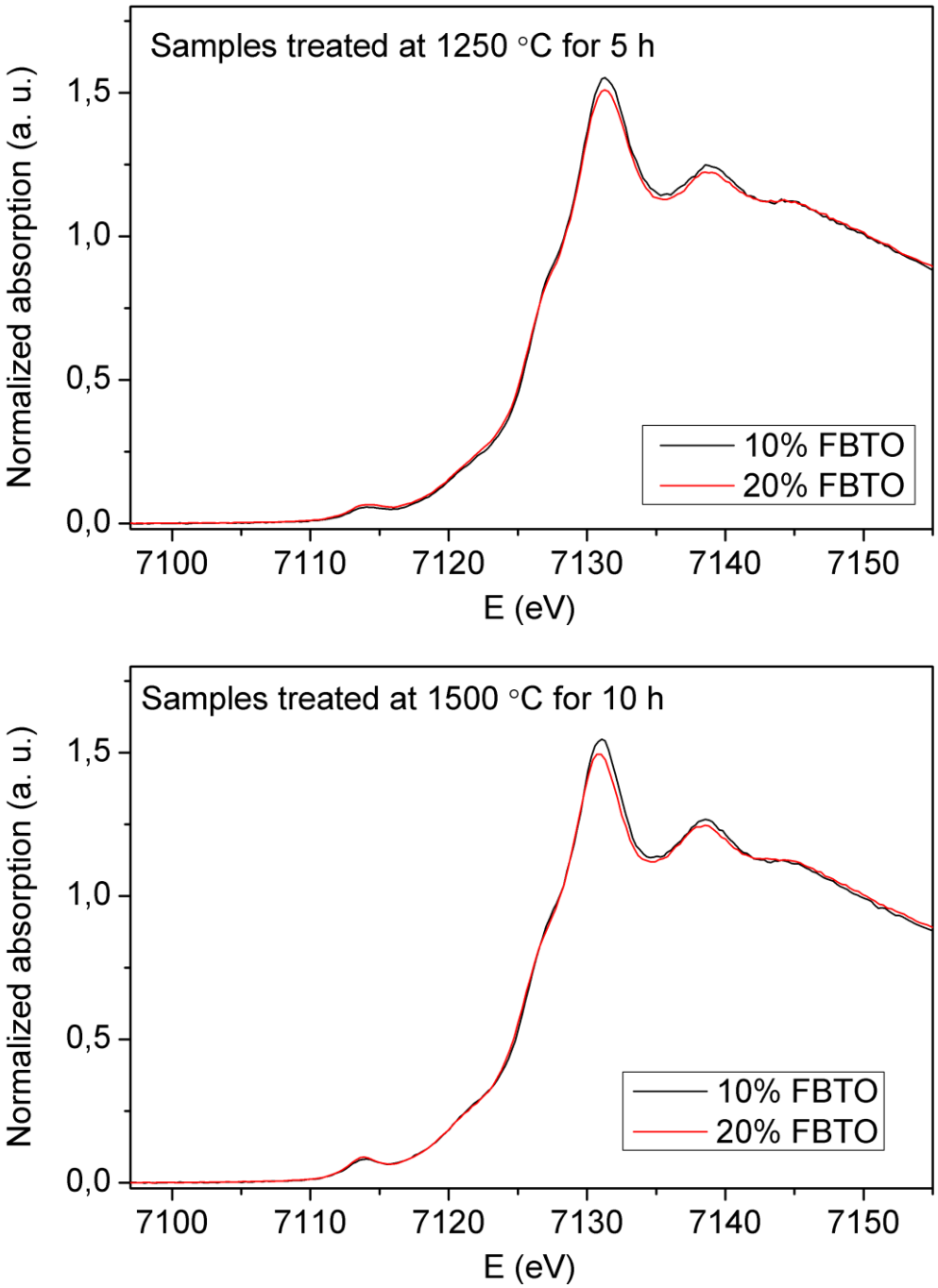

Figure 5.10. Normalized Fe K-edge XANES spectra measured on the 10% and 20% Fe-doped $BaTiO_3$ (Batch 1) samples after treatment at 1250°C for 5h (10FBTO_12(5)_B1 and 20FBTO_12(5)_B1) and subsequent annealing at 1500°C for 10 h (10FBTO_15(10)_B1 and 20FBTO_15(10)_B1).

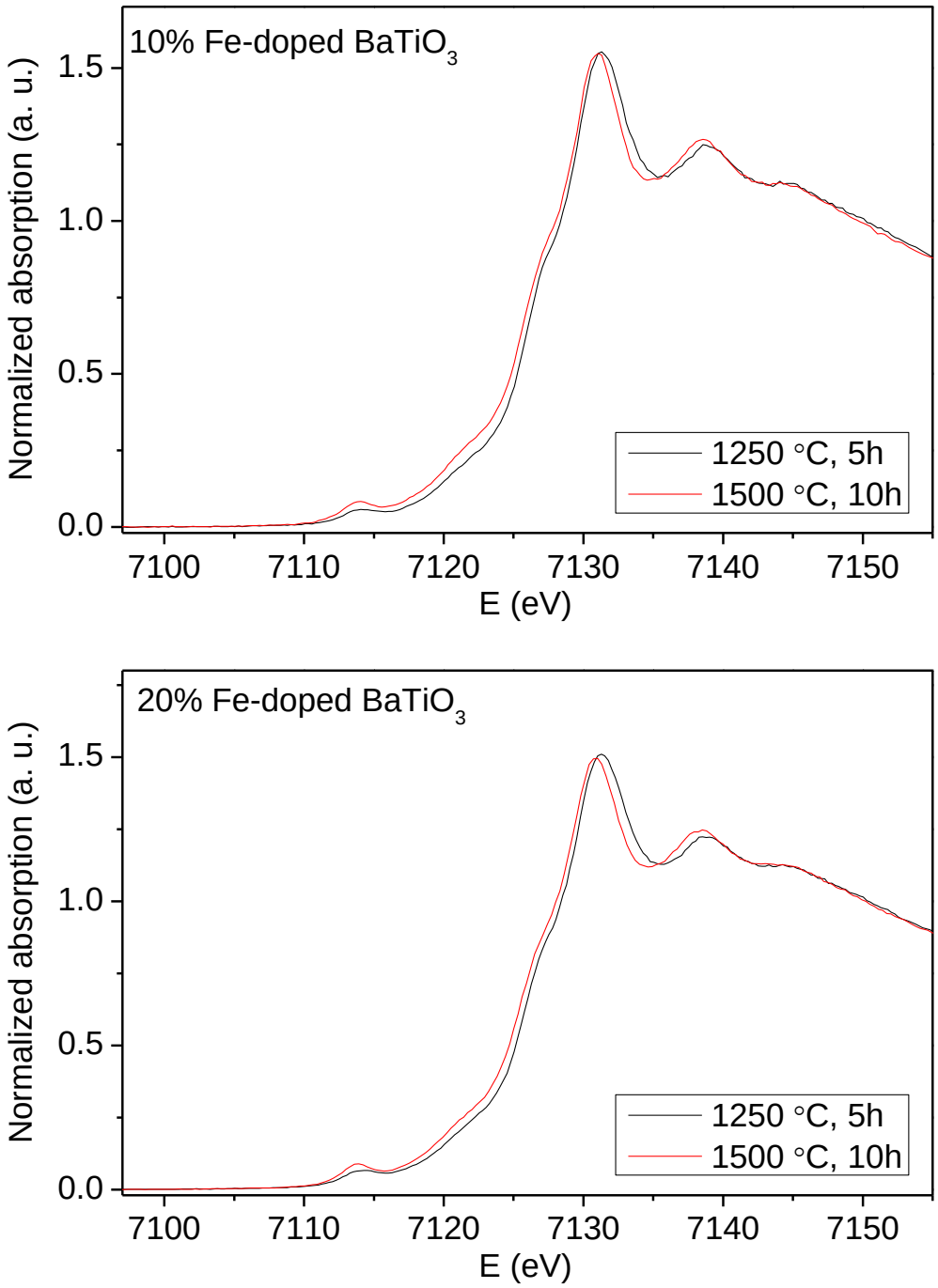

Figure 5.11. Normalized Fe K-edge XANES spectra measured on the 10% and 20% Fe-doped $BaTiO_3$ samples after treatment at 1250°C for 5h (20FBTO_12(5)_B1) and subsequent annealing at 1500°C for 10h (20FBTO_15(10)_B1).

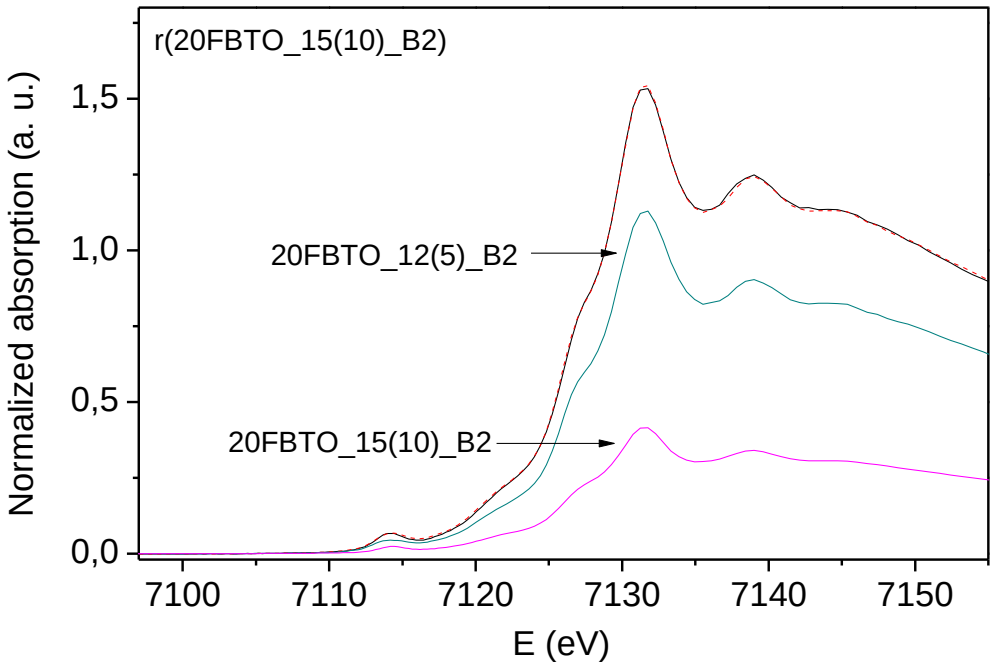

Figure 5.12. Fe K-edge XANES spectrum of the 20% Fe-doped $BaTiO_3$ sample re-annealed at 1250°C for 10h (r(20FBTO_15(10)_B2). Solid line – experiment; dashed red line – best fit linear combination of XANES profiles of 20% Fe-doped $BaTiO_3$ (Batch 2) samples, one fired at 1250ºC for 5h (20FBTO_12(5)_B2) and one additionally annealed at 1500ºC for 10h (20FBTO_15(10)_B2), both components are shown below.

5.4.Fe K-edge EXAFS analysis

For investigation of the Fe distribution over the Ti(1) and Ti(2) sites we have chosen to use Fe K-edge EXAFS, which gives information on the local structure around the Fe ion [92, 97-99].

The Fe K-edge EXAFS spectra of 10% and 20% Fe-doped $BaTiO_3$ samples, listed in Table 5.5, are plotted on Figure 5.14, Figure 5.17 and Figure 5.19. The EXAFS signal is a superposition of two signals, one from the Fe(1) atoms located at Ti(1) site and the other, arising from Fe(2) atoms located at Ti(2) site. Contributions of individual shells of atoms around Fe atom are visible up to about 5 Å in Fourier Transform (FT) magnitudes of the EXAFS spectra (Figure 5.15, Figure 5.18 and Figure 5.20). FT magnitude of consecutive neighbour shells contributions is shown on the Figure 5.21 for the EXAFS model of the 20% Fe-doped BaTiO3 (Batch 2)

annealed at 1500 ºC for 10 h (20FBTO_15(10)_B2). Qualitative comparison of the EXAFS spectra shows that the local neighbourhood of Fe in all samples of Fe-doped $BaTiO_3$ is similar, with small but significant differences in the first and second coordination shells.

Crystal structure of the hexagonal barium titanate consists of two titanium octahedrally coordinated crystallographic sites (Ti(1) and Ti(2)), which have significantly different local structure (Figure 3.1 and Table 3.1). The structure parameters of nearest neighbour shells around Ti(1) and Ti(2) sites (type and number of neighbour atoms, and distances) are listed in the Table 5.6.

Table 5.6. Parameters of the nearest neighbours around Ti atom for Ti(1) and Ti(2) crystallographic sites in the 6H-$BaTiO_3$ [84]. The neighbour atom annotations are based on Ti atoms at two crystallographic sites (Ti(1) and Ti(2)) and Ti neighbour atoms, ordered by distance in 6H-$BaTiO_3$ crystal structure: for example, O(2/1) are oxygen neighbours of Ti(2) atoms located at 1.96 Å; O(2/2) are oxygen neighbours of Ti(2) atoms located at 1.99 Å. ***N*** – number of neighbour atoms, ***R*** – distance from the Ti atom.

Ti neighbor	***N***	***R* (Å)**
Ti(2)		
O(2/1)	3	1,96
O(2/2)	3	1,99
Ti(2/1)	1	2,69
Ba(2/1)	3	3,40
Ba(2/2)	1	3,50
Ba(2/3)	3	3,57
Ti(2/2)	3	3,94
O(2/3)	3	4,07
Ti(1)		
O(1/1)	6	1,98
Ba(1/1)	2	3,49
Ba(1/2)	6	3,57
Ti(1/1)	6	3,94
O(1/2)	12	4,52
O(1/3)	12	4,52

For quantitative Fe K-edge EXAFS analysis, performed with the IFEFFIT program package [92], two FEFF [98] models were constructed, one for iron atoms located at Ti(1) site and one for iron atoms located at Ti(2) site. Measured EXAFS spectra were modelled with a linear combination of both FEFF models, where relative amount of each model signal ($X_{Fe(1)}$ and $X_{Fe(2)}$) - representing the relative occupancy of Fe on each Ti site, was allowed to vary in the EXAFS fit.

The FEFF model of each site comprised all single and significant multiple scattering paths of the photoelectron up to 4.5 Å. For each Fe neighbour shell a neighbour distances ΔR_i and Debye-Waller factor (σ_i^2) were allowed to vary. The stoichiometry was not varied in the fit, i.e. the number of neighbours at each distance was left as defined from the crystallographic data, except number of oxygens in the first Fe coordination shell was varied to detect eventual redistribution of oxygen vacancies around Fe cations in the crystal structure. In addition, a common shift of energy origin ΔE_0 for all scattering paths was allowed to vary in the fit for each spectrum. The EXAFS amplitude reduction factor S_0^2 was kept fixed at 0.75 the value determined in the Fe K-edge EXAFS fit in ref. [93].

The number of variable parameters in both EXAFS models was minimised, exploiting numerous connections and restraints between the parameters to reduce the uncertainty of best fit values and to precisely detect structural differences in the sample at different sintering conditions. A common variable linear expansion coefficient was introduced to restrain the variation of neighbour distance ΔR_i, and a correlated Debye model [92, 100] was used to determine the Debye-Waller factors by varying a single Debye temperature parameter. In exception, the distances and Debye-Waller factors for the first four closest single-scattering paths Fe(2)-O(2/1), Fe(2)-O(2/2) Fe(2)-Ti(2/1) and Fe(1)-O(1/1) were varied separately. In addition, Fe(2)-Ba(2/1), Fe(2)-Ba(2/3) and Fe(1)-Ba(1/2) distances were allowed to vary separately. The relative site occupation parameters $X_{Fe(1)}$ and $X_{Fe(2)}$ of Fe in Ti(1) and Ti(2) sites were constrained to a unit sum.

To verify the formation of Fe pairs on two adjacent Ti(2) sites in the Ti_2O_9 polyhedra (i.e. the formation of Fe_2O_9 polyhedra), Fe(2)-Fe(2/1) scattering path was included in the fit at the Ti(2)-Ti(2/1) distance of 2,69 Å of the undoped $BaTiO_3$. The number of such Fe pairs and their interatomic distance were allowed to vary. However, the number of Fe(2)-Ti(2/1) pairs was constrained to the total occupancy of Ti(2) sites

with Fe cations. The same Debye-Waller factor was used for Fe(2)-Fe(2/1) and Fe(2)-Ti(2/1) scattering paths. The Fe(2)-Fe(2/1) distance was allowed to vary separately.

To minimize the relatively large uncertainties of some fitting parameters, due to high correlations between these parameters in the fit of each individual spectrum, a simultaneous fit of all the measured spectra of Fe-doped $BaTiO_3$ samples was performed.

Fe EXAFS analysis shows that in all samples iron atoms substitute Ti in the $BaTiO_3$ crystal structure. There are no secondary iron phases present. Detailed Fe-EXAFS analysis also revealed a local deformation of the crystal structure around Fe cations in the samples with 10% and 20% of Fe. The substitution of Ti(2) atoms by Fe atoms leads to the small distortions of oxygen octahedra resulting in distribution of nearest oxygen neighbours in two distances. For the more distant shells we didn't find significant distortions, except a slight relaxation of interatomic distances.

A very good fit of the 10% Fe-doped $BaTiO_3$ was obtained in the R-range 1.1-3.9 Å and in the k-interval of [4.3 $Å^{-1}$ – 12 $Å^{-1}$] using k^2-weight for sample treated at 1250˚C (10FBTO_12(5)_B1) and k^3-weight for sample additionally annealed at 1500˚C for 10h (10FBTO_15(10)_B1). In the simultaneous relaxation, some of the parameters of the fitted spectra were constrained to common values, in particular, Debye temperature parameter, a common shift of energy origin ΔE_0 and Debye-Waller factor for Fe(2)-O(2/2) paths.

Quantitative EXAFS analysis of the 10% Fe-doped $BaTiO_3$ reveals that after heat treatment at 1250˚C in the first synthesis step (10FBTO_12(5)_B1), about half of all Fe atoms preferably occupy the Ti(1) crystallographic sites, while the other half of Fe atoms occupy Ti(2) site (Figure 5.13a). At this syntheses step the number of oxygen vacancies in O(2/2) site was below detection limit, so the coordination number of O(2/2) was fixed to 2.95, which corresponds to the random distribution of oxygen vacancies around Fe(2) in the sample. No formation of Fe(2)-Fe(2/1) pairs has been detected. After further heat treatment at 1500˚C for 10 h (10FBTO_15(10)_B1) about 10% of Fe atoms incorporated on Ti(1) site relocate to the Ti(2) site (Figure 5.13b). For this sample ordering of the oxygen vacancies by varying the coordination number of the O(2/2) atoms was detected. The number of oxygen vacancies ordered in O(2/2) site around Fe(2) atoms was 1.2. During the fit the number of Fe(2)-Fe(2/1)

pairs could not be reliably determined by varying the coordination number of the Fe(2/1) neighbour atoms. However, it was found that fixing the coordination number of the Fe(2/1) neighbours atoms to the 0.1 improves the fit. The EXAFS analysis shows that the distance between Fe(2)-Ti(2/1) cations decreases from 2.70 Å to 2.58Å compared with sample treated at 1250˚C (10FBTO_12(5)_B1). Best fit parameters are collected in Table 5.7. The quality of the fit is shown on the Figure 5.14 and Figure 5.15.

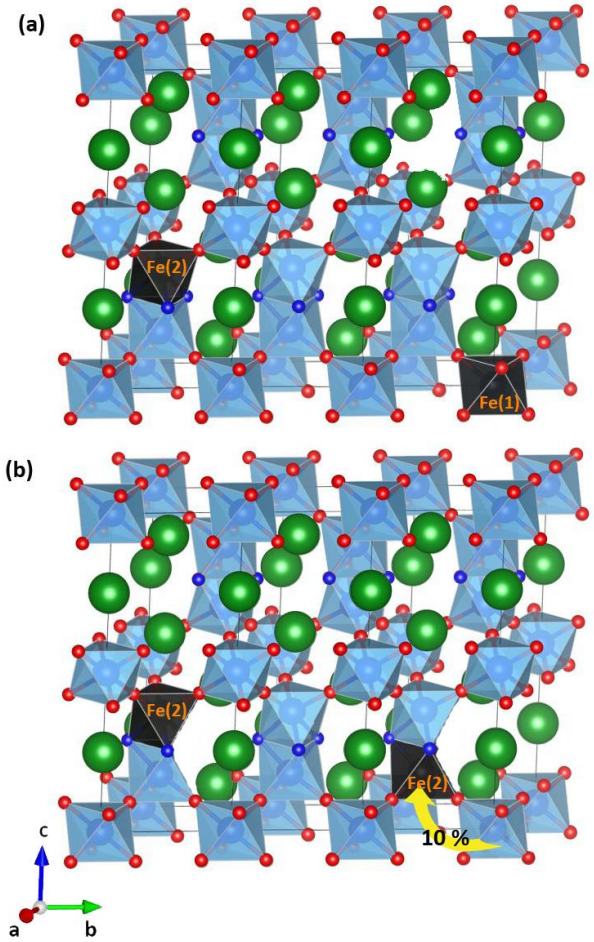

Figure 5.13. Schematic presentation of the oxygen ordering process in 10% Fe-doped 6H-$BaTiO_3$. Schematic view of the Fe-distribution within three unit cells of the Fe-doped 6H-$BaTiO_3$ crystal structure (*P63/mmc*): (a) after treatment at 1250 °C for 5h (10FBTO_12(5)_B1) (b) subsequent annealing at 1500°C for 10h (10FBTO_15(10)_B1). The Ti(1) and Ti(2) sites, occupied by Fe^{3+} cations, are marked black. Fe^{3+} movements between the Ti sites are indicated by the yellow arrow.

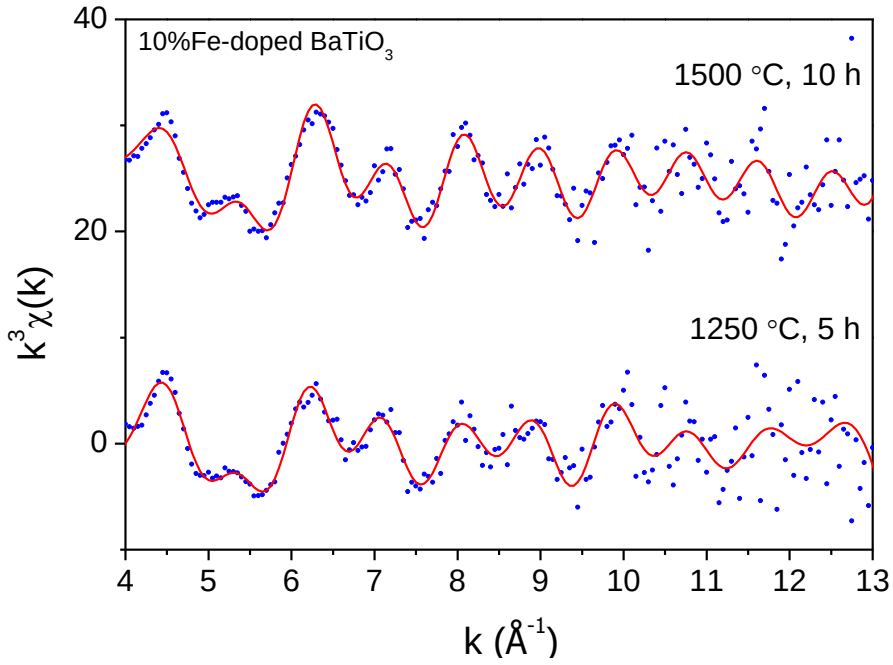

Figure 5.14. The k^3-weighted Fe K-edge EXAFS spectra of 10% Fe-doped $BaTiO_3$ annealed at different temperatures (10FBTO_12(5)_B1 and 10FBTO_15(10)_B1). Red line - best fit EXAFS model. The spectra are displaced vertically for clarity.

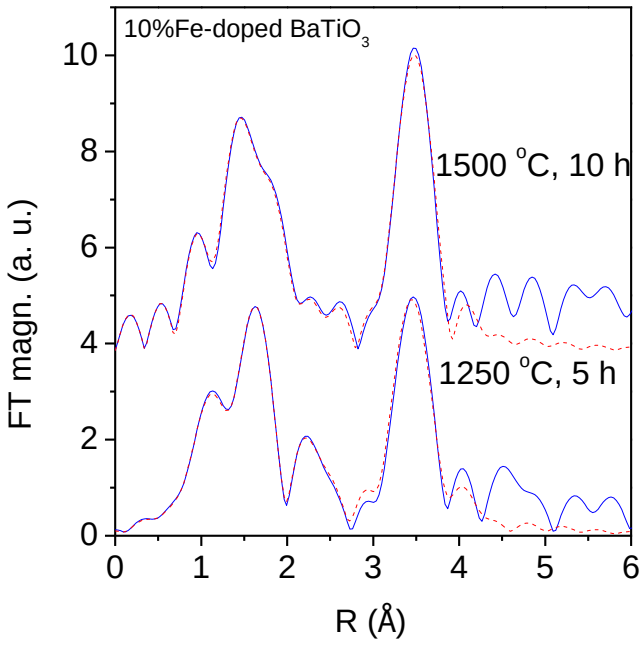

Figure 5.15. The Fourier transform magnitudes of 10% Fe-doped $BaTiO_3$ annealed at different temperatures (10FBTO_12(5)_B1 and 10FBTO_15(10)_B1). Red dashed line - best fit EXAFS model. The spectra are displaced vertically for clarity.

Table 5.7. Parameters of the nearest neighbours around Fe atom on Ti(1) and Ti(2) crystallographic sites in the 10% Fe-doped $BaTiO_3$ samples treated at different annealing temperatures 1250°C (10FBTO_12(5)_B1) and 1500°C (10FBTO_15(10)_B1). (***N*** – number of neighbour atoms, ***R*** – distance from the Fe atom; $\boldsymbol{\sigma^2}$ – Debye-Waller factor, $\boldsymbol{X_{Fe(1)}}$ and $\boldsymbol{X_{Fe(2)}}$ are the relative site occupation parameters of Fe in Ti(1) and Ti(2) sites, respectively).

	1250 °C, 5 h (10FBTO_12(5)_B1)			**1500 °C, 5 h (10FBTO_15(10)_B1)**		
ΔE_0	0.69 ±0.5 eV			0.29 ±0.5 eV		
Fe neighbours	**N**	**R [Å]**	**σ^2 [Å^2]**	**N**	**R [Å]**	**σ^2 [Å^2]**
Fe(2)	$X_{Fe(2)}$=0.51(4)			$X_{Fe(2)}$=0.61(3)		
O(2/1)	2.9	1.88 (1)	0.007 (3)	2.9	1.89 (1)	0.002 (1)
O(2/2)	2.9	2.02 (1)	0.004 (2)	1.8 (8)	2.02 (4)	0.004 (2)
Ti(2/1)	1	2.7 (1)	0.003 (1)	0.9	2.59 (2)	0.008 (1)
Fe(2/1)	0	-	-	0.1	2.88 (1)	0.008 (2)
Ba(2/1)	2.9	3.40 (1)	0.005 (1)	2.9	3.31 (1)	0.005 (1)
Ba(2/2)	1	3.50 (1)	0.005 (1)	1	3.45 (1)	0.005 (1)
Ba(2/3)	3	3.57 (1)	0.005 (1)	3	3.51 (1)	0.005 (1)
Ti(2/2)	3	3.94 (1)	0.008 (1)	3	3.88 (1)	0.008 (1)
O(2/3)	3	4.08 (1)	0.016 (1)	3	4.02 (1)	0.016 (1)
Fe(1)	$X_{Fe(1)}$=0.49 (4)			$X_{Fe(1)}$=0.39 (3)		
O(1/1)	5.8	1.99 (2)	0.010 (2)	5.8	2.04 (1)	0.003 (1)
Ba(1/1)	2	3.49 (1)	0.005 (1)	2	3.44 (1)	0.005 (1)
Ba(1/2)	6	3.65 (1)	0.005 (1)	6	3.70 (1)	0.005 (1)
Ti(1/1)	6	3.94 (1)	0.008 (1)	6	3.88 (2)	0.008 (1)
O(1/2)	12	4.52 (1)	0.016 (1)	12	4.45 (1)	0.016 (1)
O(1/3)	12	4.53 (1)	0.016 (1)	12	4.46 (1)	0.016 (1)

A very good agreement between the model and an experimental data of the 20% Fe-doped $BaTiO_3$ (Batch 1) was obtained in the k-interval of [4.3 $Å^{-1}$ – 13 $Å^{-1}$] using k^3-weight in the R-range 1.1-3.9 Å. Also in this case the simultaneous relaxation was used in the fit, where some of the parameters of the fitted spectra were constrained to common values. In particular, the Fe(2)-O(2/1) and Fe(1)-O(1/1) interatomic distances were kept the same for samples treated at 1250ºC (20FBTO_12(5)_B1) and sample additionally annealed at 1500ºC for 5 h (20FBTO_15(5)_B1). For samples subsequently annealed at 1500ºC (20FBTO_15(5)_B1 and 20FBTO_15(10)_B1) a common shift of energy origin ΔE_0 and the Debye-Waller factors for Fe(1)-O(1/1) and Fe(2)-Fe(2/1) paths were constrained to the common values. Constraining these common parameters to the same value for all the spectra, however, would represent too rigid model, which cannot adequately describe all of the structural differences that were detected between the samples with different concentration of iron and treated under different conditions.

The Fe K-edge EXAFS analysis (Figure 5.17 and Figure 5.18) of the 20% Fe-doped $BaTiO_3$ (Batch 1) sample treated at 1250°C (20FBTO_12(5)_B1) shows that Fe ions are randomly distributed over the Ti(1) and Ti(2) sites (Figure 5.16a): 1/3 of the dopant Fe ions are located at the Ti(1) site while 2/3 at the Ti(2) site. No preferential distribution of the oxygen vacancies was detected at this stage.

After further heat treatment of the same material at 1500°C for 5h (20FBTO_15(5)_B1) the formation of Fe(2)-Fe(2/1) pairs was detected. About half of the randomly distributed Fe ions on the Ti(2) sites pair up to form fully substituted Ti_2O_9 polyhedra (i.e. Fe_2O_9) (Figure 5.16b). The Fe ions on the Ti(1) sites do not change their position. We have not been able to detect any significant ordering or segregation of the oxygen vacancies during this stage. They appear to remain randomly distributed.

Only after the longer heat treatment at 1500°C for 10 h (20FBTO_15(10)_B1) the major part of the Fe ions from the Ti(1) sites relocate to the Ti(2) sites (Figure 5.16c). After the relocation to the Ti(2) sites is completed about half of the Fe ions on the Ti(2) sites occupy the Ti_2O_9 polyhedra in pairs whereas single occupancy has been found for the other half.

In all 20% Fe-doped $BaTiO_3$ samples of Batch 1 we observed relaxation of distances of barium atoms: Fe(2)-Ba(2/3) distance was increasing with increasing annealing

temperature and length of annealing time. Fe(1)-Ba(1/2) distance decreased from 3.66 Å for sample treated at 1250^{o}C (20FBTO_12(5)_B1) to 3.50 Å for samples treated at 1500^{o}C (20FBTO_15(5)_B1 and 20FBTO_15(10)_B1). Similar, the Fe(2)-Ba(2/1) distance decreased from 3.66 Å for sample treated at 1250^{o}C (20FBTO_12(5)_B1) to 3.33 Å for samples treated at 1500^{o}C (20FBTO_15(5)_B1 and 20FBTO_15(10)_B1).

EXAFS analysis shows the increasing of the distance between Fe(2)-Fe(2/1) cations from 2.67 Å to the 2.88 Å compared with Fe(2)-Ti(2/1) distance. Best fit parameters are collected in a Table 5.8 and Table 5.9. The quality of the fit is shown on the Figure 5.17 and Figure 5.18.

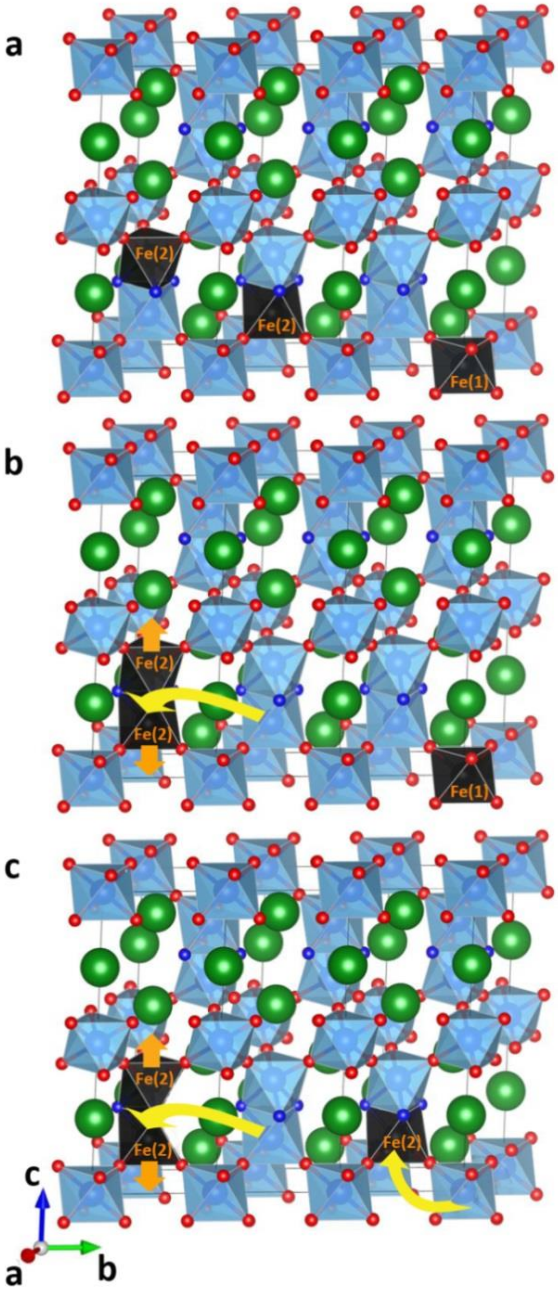

Figure 5.16. Schematic presentation of the cation ordering process in 20% Fe-doped 6H-$BaTiO_3$. Schematic view of the Fe-distribution within three unit cells of the Fe-doped 6H-$BaTiO_3$ crystal structure (*P63/mmc*): (a) after treatment at 1250 °C for 5h (20FBTO_12(5)_B1) (b) subsequent annealing at 1500°C for 5h (20FBTO_15(5)_B1) and (c) further annealing at 1500°C for another 10h (20FBTO_15(10)_B1). The Ti(1) and Ti(2) sites, occupied by Fe^{3+} cations, are marked black. Fe^{3+} movements between the Ti sites are indicated by the yellow arrows. The orange arrows mark displacements of Fe^{3+} ions with respect to the initial Ti position in the undoped 6H-$BaTiO_3$.

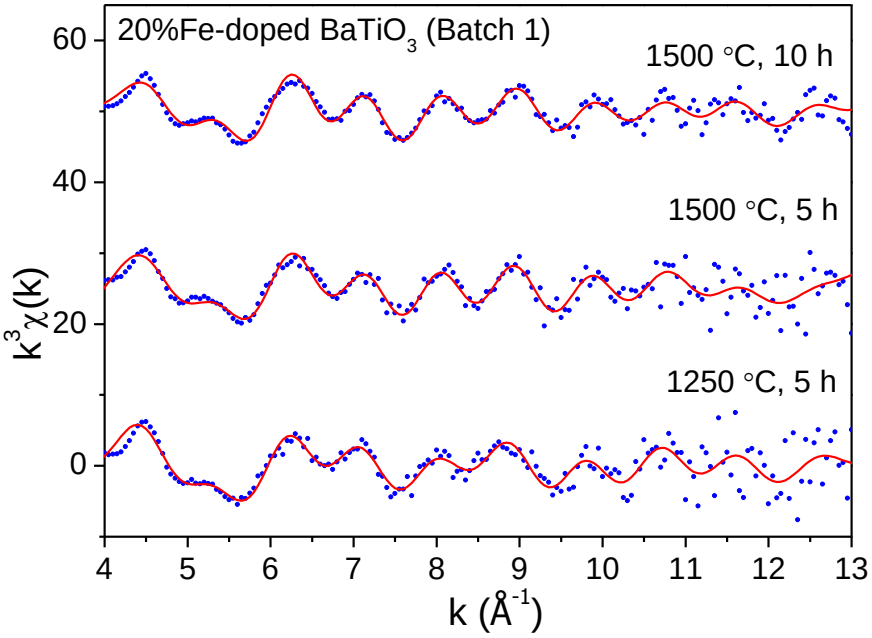

Figure 5.17. The k^3-weighted Fe K-edge EXAFS spectra of 20% Fe-doped $BaTiO_3$ (Batch 1) annealed at different temperatures (20FBTO_12(5)_B1, 20FBTO_15(5)_B1 and 20FBTO_15(10)_B1). Red line - best fit EXAFS model. The spectra are displaced vertically for clarity.

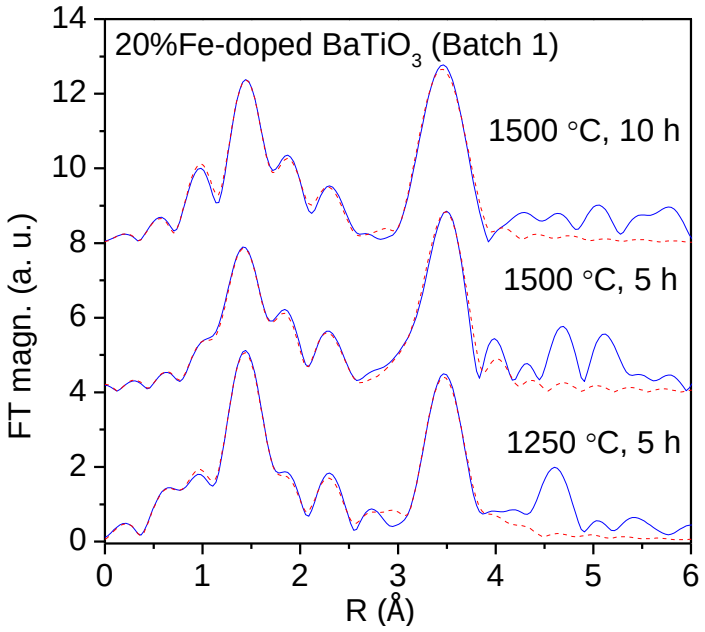

Figure 5.18. The Fourier transform magnitudes of 20% Fe-doped $BaTiO_3$ (Batch 1) annealed at different temperatures (20FBTO_12(5)_B1, 20FBTO_15(5)_B1 and 20FBTO_15(10)_B1). Red dashed line - best fit EXAFS model. The spectra are displaced vertically for clarity.

Table 5.8. Parameters of the nearest neighbours around Fe atom on Ti(1) and Ti(2) crystallographic sites in the 20% Fe-doped $BaTiO_3$ (Batch 1) treated at 1250ºC (20FBTO_15(5)_B1). (***N*** – number of neighbour atoms, ***R*** – distance from the Fe atom; $\boldsymbol{\sigma^2}$ – Debye-Waller factor, $\boldsymbol{X_{Fe(1)}}$ and $\boldsymbol{X_{Fe(2)}}$ are the relative site occupation parameters of Fe in Ti(1) and Ti(2) sites, respectively).

	1250 °C, 5 h (20FBTO_15(5)_B1)		
ΔE_0	**-0.7 ± 2.5 eV**		
Fe neighbours	**N**	**R [Å]**	**σ^2 [Å^2]**
Fe(2)	$X_{Fe(2)}$=0.61(8)		
O(2/1)	3	1.87 (1)	0.001
O(2/2)	2.79	2.01 (2)	0.003 (1)
Ti(2/1)	1	2.68 (2)	0.009 (2)
Fe(2/1)	0	-	-
Ba(2/1)	3	3.41 (2)	0.007 (2)
Ba(2/2)	1	3.48 (2)	0.007 (2)
Ba(2/3)	3	3.56 (2)	0.007 (2)
Ti(2/2)	3	3.93 (2)	0.010 (2)
O(2/3)	3	4.06 (2)	0.021 (2)
Fe(1)	$X_{Fe(1)}$=0.39 (8)		
O(1/1)	6	2.02 (1)	0.012 (6)
Ba(1/1)	2	3.48 (4)	0.007 (2)
Ba(1/2)	6	3.66 (2)	0.007 (2)
Ti(1/1)	6	3.93 (2)	0.010 (2)
O(1/2)	12	4.50 (3)	0.021 (2)
O(1/3)	12	4.51 (3)	0.021 (2)

Table 5.9. Parameters of the nearest neighbours around Fe atom on Ti(1) and Ti(2) crystallographic sites in the 20% Fe-doped $BaTiO_3$ (Batch 1) treated at 1500ºC (20FBTO_15(5)_B1 and 20FBTO_15(10)_B1). (***N*** – number of neighbour atoms, ***R*** – distance from the Fe atom; $\boldsymbol{\sigma^2}$ – Debye-Waller factor, $\boldsymbol{X_{Fe(1)}}$ and $\boldsymbol{X_{Fe(2)}}$ are the relative site occupation parameters of Fe in Ti(1) and Ti(2) sites, respectively).

	1500 °C, 5 h (20FBTO_15(5)_B1)			**1500 °C, 10 h (20FBTO_15(10)_B1)**		
ΔE_0	1.5 ±1.5 eV			1.5 ±1.5 eV		
Fe neighbours	**N**	**R [Å]**	**σ^2 [Å^2]**	**N**	**R [Å]**	**σ^2 [Å^2]**
Fe(2)	$X_{Fe(2)}$=0.63(7)			$X_{Fe(2)}$=0.86(10)		
O(2/1)	3	1.87 (1)	0.001 (1)	3	1.93 (3)	0.001 (1)
O(2/2)	2.79	2.13 (3)	0.012 (6)	2.2 (5)	2.08 (2)	0.001
Ti(2/1)	0.8 (1)	2.67 (1)	0.007 (2)	0.8 (1)	2.65 (2)	0.007 (1)
Fe(2/1)	0.2 (1)	2.88 (4)	0.007 (2)	0.2 (1)	2.88 (4)	0.007 (2)
Ba(2/1)	3	3.32 (1)	0.007 (2)	3	3.35 (2)	0.008 (1)
Ba(2/2)	1	3.47 (1)	0.007 (2)	1	3.45 (2)	0.008 (1)
Ba(2/3)	3	3.65 (6)	0.007 (2)	3	3.73 (2)	0.008 (1)
Ti(2/2)	3	3.91 (1)	0.010 (2)	3	3.88 (2)	0.013 (1)
O(2/3)	3	4.04 (1)	0.021 (2)	3	4.02 (2)	0.027 (1)
Fe(1)	$X_{Fe(1)}$=0.37 (7)			$X_{Fe(1)}$=0.14 (10)		
O(1/1)	6	2.02 (1)	0.002 (1)	6	1.81 (5)	0.002 (1)
Ba(1/1)	2	3.46 (1)	0.007 (2)	2	3.44 (2)	0.008 (1)
Ba(1/2)	6	3.48 (1)	0.007 (2)	6	3.52 (2)	0.008 (1)
Ti(1/1)	6	3.91 (2)	0.010 (2)	6	3.88 (2)	0.013 (1)
O(1/2)	12	4.48 (1)	0.021 (2)	12	4.45 (2)	0.027 (1)
O(1/3)	12	4.52 (1)	0.021 (2)	12	4.52 (2)	0.027 (1)

A very good fit for the 20% Fe-doped $BaTiO_3$ of Batch 2 samples was obtained in the k-range 4.3-12 $Å^{-1}$ using k^3-weight (20FBTO_12(5)_B2, 20FBTO_15(10)_B2, r(20FBTO_15(10)_B2) and 20FBTO_15(50)_B2). In the simultaneous relaxation, some of the parameters of the fitted spectra were constrained to common values. For 20FBTO_12(5)_B2, 20FBTO_15(10)_B2 and r(20FBTO_15(10)_B2) samples the Debye temperature parameter and Debye-Waller factor for Fe(2)-O(2/1) path were constrained to the common value. For all additionally annealed at 1250°C and 1500°C samples (20FBTO_15(10)_B2, r(20FBTO_15(10)_B2) and 20FBTO_15(50)_B2) a common shift of energy origin ΔE_0, the interatomic distance and Debye-Waller factor for Fe(2)-O(2/2) path were constrained to the common value. For samples treated at 1250°C (20FBTO_12(5)_B2 and r(20FBTO_15(10)_B2)) the interatomic distance and Debye-Waller factor for Fe(1)-O(1/1) path were constrained to the common value. For 20FBTO_15(10)_B2 and r(20FBTO_15(10)_B2) samples the interatomic distance and Debye-Waller factor for Fe(1)-Fe(1/1) path were constrained to the common value. For samples treated at 1500°C (20FBTO_15(10)_B2, r(20FBTO_15(10)_B2) and 20FBTO_15(50)_B2) the common value of the interatomic distance for the Fe(1)-O(1/1) path was used. Constraining these common parameters to the same value for all the spectra, however, would represent a too rigid model, which cannot adequately describe all of the structural differences that were detected between the samples with different concentration of iron and treated under different conditions.

EXAFS analysis of the 20% Fe-doped $BaTiO_3$ samples of Batch 2 shows that 2/3 of all Fe atoms occupy the Ti(2) sites, while the rest 1/3 occupy Ti(1) sites. In the samples treated at 1500°C for 10h and 50h (20FBTO_15(10)_B2 and 20FBTO_15(50)_B2) and, also, in the re-annealed at 1250°C for 10h sample (r(20FBTO_15(10)_B2)), the Fe(2)-Fe(2/1) pairs were observed. No preferential distribution of the oxygen vacancies has been detected in any of the samples. Best fit parameters are collected in a Table 5.10 and Table 5.11. The quality of the fit is shown on the Figure 5.19 and Figure 5.20.

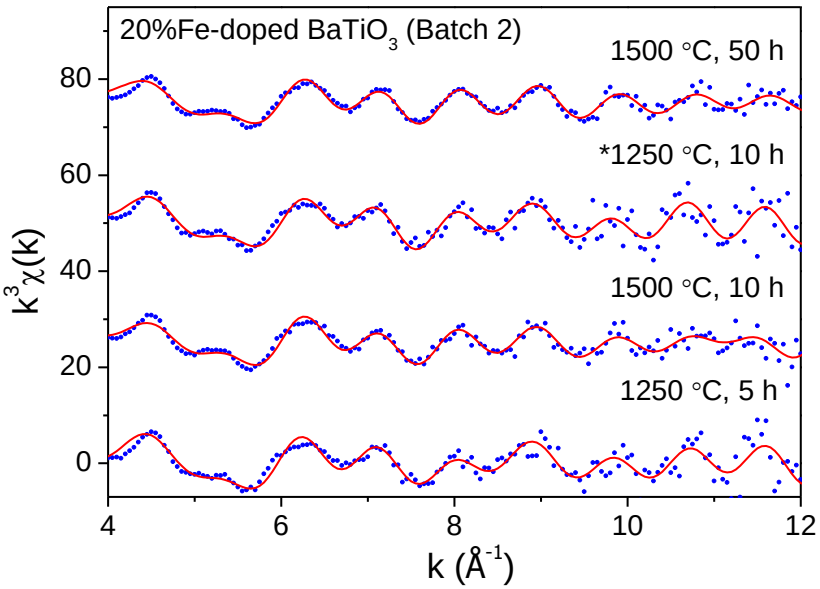

Figure 5.19. The k^3-weighted Fe K-edge EXAFS spectra of 20% Fe-doped $BaTiO_3$ (Batch 2) annealed at different temperatures and different time (20FBTO_12(5)_B2, 20FBTO_15(10)_B2, r(20FBTO_15(10)_B2) and 20FBTO_15(50)_B2). Red line - best fit EXAFS model. The spectra are displaced vertically for clarity.

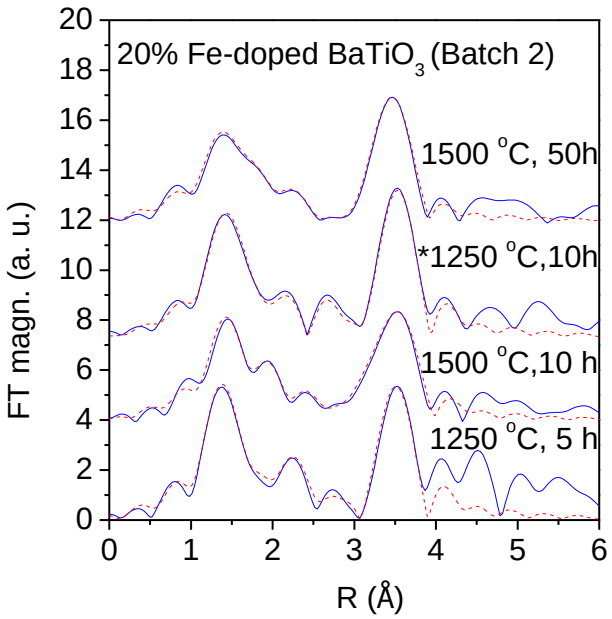

Figure 5.20. The Fourier transform magnitudes of 20% Fe-doped $BaTiO_3$ (Batch 2) annealed at different temperatures and different time (20FBTO_12(5)_B2, 20FBTO_15(10)_B2, r(20FBTO_15(10)_B2) and 20FBTO_15(50)_B2). Red dashed line - best fit EXAFS model. The spectra are displaced vertically for clarity.

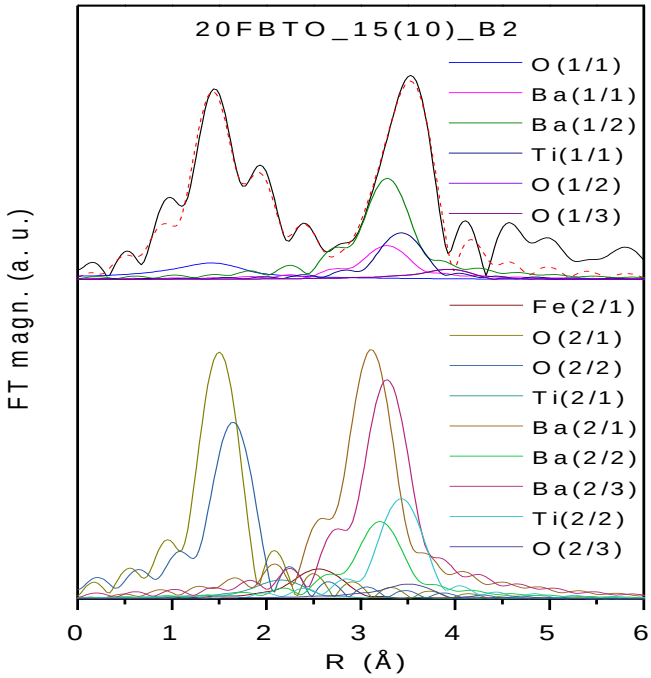

Figure 5.21. The Fourier transform magnitude of 20% Fe-doped BaTiO3 (Batch 2) annealed at 1500ºC for 10 h (20FBTO_15(10)_B2), together with the contributions of individual neighbour shells for Fe(1) (top) and Fe(2) (bottom) sites. Experiment – black solid line; EXAFS model - red dashed line. The spectra are displaced vertically for clarity.

Table 5.10. Parameters of the nearest neighbours around Fe atom on Ti(1) and Ti(2) crystallographic sites in the 20% Fe-doped $BaTiO_3$ (Batch 2) samples treated at 1250 °C for 5h (20FBTO_12(5)_B2) and 1500°C for 10h (20FBTO_15(10)_B2). (***N*** – number of neighbour atoms, ***R*** – distance from the Fe atom; $\boldsymbol{\sigma^2}$ – Debye-Waller factor, $\boldsymbol{X_{Fe(1)}}$ and $\boldsymbol{X_{Fe(2)}}$ are the relative site occupation parameters of Fe in Ti(1) and Ti(2) sites, respectively).

	1250 °C, 5h (20FBTO_12(5)_B2)			**1500 °C, 10h (20FBTO_15(10)_B2)**		
ΔE_0	**-5.9 ± 1.2 eV**			**-3.2 ± 0.8 eV**		
Fe neighbors	**N**	**R [Å]**	**σ^2 [Å^2]**	**N**	**R [Å]**	**σ^2 [Å^2]**
Fe(2)	$X_{Fe(2)}$=0.73 (4)			$X_{Fe(2)}$=0.81 (6)		
O(2/1)	2.9	1.87 (1)	0.002 (1)	2.9	1.87 (1)	0.002 (1)
O(2/2)	2.9	2.03 (1)	0.003 (1)	2.9	2.04 (1)	0.003 (1)
Ti(2/1)	1	2.63 (2)	0.005 (4)	0.5 (3)	2.59 (6)	0.012 (1)
Fe(2/1)	0	-	-	0.5 (3)	2.95 (4)	0.012 (3)
Ba(2/1)	3	3.34 (1)	0.003 (1)	3	3.34 (1)	0.003 (1)
Ba(2/2)	1	3.42 (1)	0.003 (1)	1	3.43 (3)	0.003 (1)
Ba(2/3)	3	3.49 (1)	0.003 (1)	3	3.51 (1)	0.003 (1)
Ti(2/2)	3	3.86 (1)	0.005 (1)	3	3.87 (1)	0.005 (1)
O(2/3)	3	3.99 (1)	0.010 (1)	3	4.00 (1)	0.010 (1)
Fe(1)	$X_{Fe(1)}$=0.27 (4)			$X_{Fe(1)}$=0.19 (6)		
O(1/1)	5.8	1.85 (1)	0.002 (1)	5.8	1.89 (1)	0.020 (14)
Ba(1/1)	2	3.42 (1)	0.003 (1)	2	3.51 (4)	0.003 (1)
Ba(1/2)	6	3.49 (1)	0.003 (1)	6	3.51 (1)	0.003 (1)
Ti(1/1)	6	3.86 (1)	0.003 (1)	6	3.87 (1)	0.005 (1)
O(1/2)	12	4.42 (1)	0.010 (1)	12	4.44 (1)	0.010 (1)
O(1/3)	12	4.43 (1)	0.010 (1)	12	4.45 (1)	0.010 (1)

Table 5.11. Parameters of the nearest neighbours around Fe atom on Ti(1) and Ti(2) crystallographic sites in the 20% Fe-doped $BaTiO_3$ (Batch 2) samples treated at 1250°C for 10h (r(20FBTO_15(10)_B2)) and 1500°C for 50h (20FBTO_15(50)_B2). (***N*** – number of neighbour atoms, ***R*** – distance from the Fe atom; $\boldsymbol{\sigma^2}$ – Debye-Waller factor, $\boldsymbol{X_{Fe(1)}}$ and $\boldsymbol{X_{Fe(2)}}$ are the relative site occupation parameters of Fe in Ti(1) and Ti(2) sites, respectively).

	1250 °C, 10h (r(20FBTO_15(10)_B2))			**1500 °C, 50h (20FBTO_15(50)_B2)**		
ΔE_0						
Fe neighbors	**N**	**R [Å]**	**σ^2 [Å^2]**	**N**	**R [Å]**	**σ^2 [Å^2]**
Fe(2)	$X_{Fe(2)}$=0.73 (6)			$X_{Fe(2)}$=0.78 (3)		
O(2/1)	2.9	1.92 (2)	0.002 (1)	2.9	1.87 (1)	0.007 (1)
O(2/2)	2.9	2.04 (1)	0.003 (1)	2.9	2.04 (1)	0.003 (1)
Ti(2/1)	0.6 (2)	2.64 (1)	0.004 (1)	0.7 (1)	2.65 (1)	0.006 (1)
Fe(2/1)	0.4 (2)	2.83 (2)	0.004 (3)	0.3 (1)	2.83 (2)	0.006 (1)
Ba(2/1)	3	3.34 (1)	0.003 (1)	3	3.32 (1)	0.006 (1)
Ba(2/2)	1	3.44 (1)	0.003 (1)	1	3.41 (1)	0.006 (1)
Ba(2/3)	3	3.51 (1)	0.003 (1)	3	3.48 (1)	0.006 (1)
Ti(2/2)	3	3.87 (1)	0.005 (1)	3	3.84 (1)	0.008 (1)
O(2/3)	3	4.000 (1)	0.010 (1)	3	3.97 (1)	0.017 (1)
Fe(1)	$X_{Fe(1)}$=0.27 (6)			$X_{Fe(1)}$=0.22 (3)		
O(1/1)	5.8	1.84 (1)	0.002 (1)	5.8	1.89 (1)	0.003
Ba(1/1)	2	3.43 (1)	0.003 (1)	2	3.41 (1)	0.006 (1)
Ba(1/2)	6	3.48 (1)	0.003 (1)	6	3.71 (2)	0.006 (1)
Ti(1/1)	6	3.87 (1)	0.005 (1)	6	3.84 (1)	0.008 (1)
O(1/2)	12	4.44 (1)	0.010 (1)	12	4.41 (1)	0.017 (1)
O(1/3)	12	4.45 (1)	0.010 (1)	12	4.41 (1)	0.017 (1)

6 DISCUSSION

Fe-doped $BaTiO_3$ with nominal compositions of $BaTi_{0.9}Fe_{0.1}O_3$ and $BaTi_{0.8}Fe_{0.2}O_3$ have been synthesized by the solid state reaction technique. The 10% Fe-doped $BaTiO_3$ sample treated at 1250 ºC (10FBTO_12(5)_B1) has prevailing hexagonal (*P63/mmc*) crystallographic phases with an admixture of the tetragonal (*P4mm*) phase. The rest of the samples show single phase composition (6H-$BaTiO_3$ crystallographic phase with *P63/mmc* space group). The results confirm the main claims of other authors from Ref. 57, 61 and 64 that about 10% of Fe is required to fully stabilize 6H-$BaTiO_3$ crystal structure. In addition, it can be concluded that the stabilization is temperature dependent: more than 10% of Fe are needed for stabilisation of the structure at 1250 ºC and less than 10% at higher temperature of 1500 ºC.

The samples treated at 1250 ºC are found to be paramagnetic. After additional annealing of the same materials at 1500 ºC for different length of time (3h, 5h, 10h and 50h) the magnetic measurements reveal the ferromagnetic behavior, except in 10% Fe-doped $BaTiO_3$ sample treated at 1500 ºC for only 1h (10FBTO_15(1)_B1) which remains paramagnetic. In consistence with the previous reports [45, 49, 53], our results show that for all ferromagnetic samples the magnetization does not reach saturation, what suggests that two kinds of magnetic states, i.e., ferromagnetic and paramagnetic, coexist.

Another striking feature of this system is that the magnetism is higher for 10% than 20% Fe-doped 6H-$BaTiO_3$. The decrease of the magnetic moment per Fe ion with an increase in the dopant concentration has already been shown by other authors [36, 42, 45, 49], however, no explanation for this behaviour has yet been offered.

Some authors claimed that room-temperature ferromagnetism is associated with some structural changes, such as ordering of oxygen vacancies [40] or Fe pairing on Ti(2) sites [66] , while others attribute the ferromagnetic behaviour to the double exchange interaction, due to the simultaneous presence of Fe^{3+} and Fe^{4+} or Ti^{4+} and Ti^{3+} valence states [40, 47, 48, 58]. And finally, ferromagnetism may also appear from impurities in the material, such as clusters or secondary phases [17, 23-27].

It is worth to mention, that there are no published reports claiming that the origin of the magnetization in Fe-doped $BaTiO_3$ is in magnetic impurities. Within our research

we examined the possibility of the presence of Fe impurities in all our Fe-doped $BaTiO_3$ samples. There are three reasons, which suggest the intrinsic nature of the ferromagnetism in Fe-doped $BaTiO_3$. First, no secondary iron-based phases were detected by XRD or EXAFS analysis. Second, all the samples treated at 1250ºC exhibit paramagnetic behaviour and ferromagnetic ordering was induced only after additional annealing at 1500 ºC. Finally, if the magnetism is attributed to presence of iron-based secondary phases, the increase in the dopant concentration would increase the saturation magnetization value. Our experimental results showed opposite behaviour. Thus, all aforementioned indications show that observed ferromagnetism in Fe-doped $BaTiO_3$ does not result from impurities in the material.

There were several reports that claimed that Fe ions in the ferromagnetic Fe-doped $BaTiO_3$ are present in a mixed valence state [45, 51, 58-60, 62, 66, 101] and, as a consequence, some authors attributed the ferromagnetic behaviour to the double exchange interaction. We used Fe K-edge XANES analysis to check the Fe valence state in all our Fe-doped $BaTiO_3$ samples. From the comparison of Fe K-edge XANES profiles of the samples and the reference compounds with well-established 3+ valence state of iron ions (Figure 5.9) we concluded that all iron is in trivalent state. Small differences in the edge profile and intensity of pre-edge resonances can be attributed to changes in an average local environment of Fe cations.

Similarly, we verified the valence state of Ti cations at all synthesis steps with the Ti K-edge XANES analysis (Figure 5.8). The analysis revealed that in all the samples Ti atoms were in the tetravalent form. No Ti^{3+} cations were detected, so we can exclude the reduction of Ti^{4+} to Ti^{3+} as a possible source of ferromagnetism in the material, which is a reasonable conclusion for the samples heat treated in oxygen atmosphere. These results are also in agreement with previously published results on 5% Fe-doped $BaTiO_3$ single crystals [66].

To summarise, no modifications of Fe or Ti valence state were detected in any of the samples so we can conclude that double exchange interaction is not responsible for the room-temperature ferromagnetism in 10% or 20% Fe-doped $BaTiO_3$.

The quantitative Fe K-edge EXAFS analysis has been carried out to verify the possible local structural changes around Fe cations at different synthesis steps, which may induce the room-temperature ferromagnetism. The EXAFS analysis showed that in all 10% and 20% Fe-doped $BaTiO_3$ samples Fe^{3+} cations substitute Ti atoms on

Ti(1) and Ti(2) crystallographic sites of 6H-$BaTiO_3$ with *P63/mmc* crystal structure. It was found that the fraction of Fe^{3+} cations incorporated onto Ti(2) crystallographic site strongly depends on the concentration of Fe cations and can be increased by treating samples at higher temperature (1500 ºC).

A unit cell of 6H-$BaTiO_3$ contains 6 octahedrally coordinated atoms of Ti^{4+}: 2 atoms at Ti(1) sites and 4 atoms at Ti(2) sites. Therefore, in a case of random distribution 2/3 of Fe atoms should substitute Ti(2) sites, while the rest 1/3 of Fe atoms should substitute Ti(1) crystallographic sites. The substitution by 10% and 20% of Fe atoms results in three and six iron atoms per five unit cells, respectively. The probability that two iron atoms would form the fully occupied face-sharing Fe_2O_9 polyhedra is less than 6%.

First, let us consider the results of Fe K-edge EXAFS analysis of the samples treated at 1250^{o}C, which exhibit pure paramagnetic behavior. In the 10% Fe-doped $BaTiO_3$ sample (10FBTO_12(5)_B1) one half of Fe ions preferably occupy the Ti(1) crystallographic site, while other half is located at Ti(2) site. This results are in disagreement with previously published by Wei et al. [40] who showed that Fe^{3+} ions prefer to occupy Ti(2) sites in 10% Fe-doped $BaTiO_3$. Such differences may be attributed to different process conditions. For 20% Fe-doped $BaTiO_3$ samples (20FBTO_12(5)_B1 and 20FBTO_12(5)_B2) we found that Fe atoms are randomly distributed over Ti(1) and Ti(2) crystallographic sites: 1/3 at the Ti(1) site, while 2/3 of Fe atoms are located in the Ti(2) site. No preferential distribution of the oxygen vacancies or formation of Fe-Fe pairs was detected.

The substitution process is well reflected in the variation of the unit cell parameters. The ionic sizes of Ti^{4+} and Fe^{3+} in its high spin configuration for the coordination number six are 0.605 Å and 0.645 Å, respectively. As a result of the substitution with the bigger ion the unit-cell parameters slightly increased.

Only after further heat treatment at 1500^{o}C for 10h the ordering of oxygen vacancies on O(2/2) crystallographic site has been detected in both 10% and 20% Fe-doped $BaTiO_3$ samples (10FBTO_15(10)_B1 and 20FBTO_15(10)_B1). In addition, the redistribution of Fe atoms from Ti(1) sites to Ti(2) sites has been observed. Such redistribution is driven by minimization of the total free energy, which comes from reduction of electrostatic repulsion of the highly charged Ti^{4+} ions on Ti(2) sites after they were substituted by Fe^{3+} ions. In all 20% Fe-doped $BaTiO_3$ samples that were

additionally annealed (20FBTO_15(5)_B1, 20FBTO_15(10)_B1, 20FBTO_15(10)_B2, r(20FBTO_15(10)_B2) and 20FBTO_15(50)_B2) about half of the randomly distributed Fe ions on the Ti(2) sites pair up to form fully substituted Ti_2O_9 polyhedra (i.e. Fe_2O_9). Statistically, for $Ba(Ti_{0.8}Fe_{0.2})O_{2.9}$, it means that out of ten parent Ti_2O_9 polyhedra in five unit cells, one polyhedron is fully substituted, four are partially ($FeTiO_9$), and the rest remain unsubstituted. Formation of such pairs results in the increase of the unit-cell volume due to the structural adaptation of the Ti_2O_9 polyhedra. This is evident from the fact that the entire volume change of the unit cell is accounted for an increase along the c-axis. The EXAFS analysis shows that the distance between cations on the Ti(2) site increases from 2.69 Å to 2.80 Å for the Ti−Ti and Fe−Fe pairs, respectively. In contrast, Chakroborty et al. reported reduction of the Fe-Fe distance compared to Ti-Ti distance in 5% Fe-doped $BaTiO_3$ single crystals [66]. For $Ba(Ti_{0.9}Fe_{0.1})O_{2.95}$ only 10% of Fe on the Ti(2) site was paired up to form the Fe_2O_9 polyhedra. These results are consistent with XRD analysis showing no additional changes in the unit cell parameters after treating samples at 1500 ºC. In contrast, Chakraborty et al. showed that about 40% of Fe atoms substituting Ti(2) site paired up for 5% Fe-doped $BaTiO_3$ single crystals [66]. Such differences may arise due to processing samples by different synthesis techniques.

Our experimental results suggest that different mechanisms are responsible for the long-range ferromagnetic interaction in 10% and 20% Fe-doped 6H-$BaTiO_3$. In case of $Ba(Ti_{0.9}Fe_{0.1})O_{2.95}$ we have shown that ordering of oxygen vacancies is playing a crucial role in ferromagnetic coupling. However, for $Ba(Ti_{0.8}Fe_{0.2})O_{2.9}$ we found that induction of ferromagnetism is associated with formation of Fe_2O_9 polyhedra in the 6H-$BaTiO_3$ crystal structure, rather than with distribution of oxygen vacancies. Moreover, in the final stage of the ordering, when (i) more Fe ions move to the Ti(2) sites and (ii) oxygen ions segregate at the O(2) sites, no significant change in the high-field magnetization was observed. This is consistent with the observation that the number of the Fe_2O_9 units does not significantly change because the new Fe^{3+} ions on the Ti(2) site do not form new Fe_2O_9 polyhedra units.

p-d Zener model is a model, which is often used to explain the ferromagnetism in p-type doped semiconductors, such as Mn-doped ZnO [14]. The model suggests that the Mn provides both the localized spins and itinerant holes. The ferromagnetic

interaction between Mn spins is mediated by high concentration of holes. According to this model the ferromagnetism in n-type doped semiconductors occurs at low temperatures or does not occur at all. Fe-doped $BaTiO_3$ is n-type semiconductor [55, 102]. Thus, the p-d Zener interaction cannot be adopted to explain the observed ferromagnetism in Fe-doped $BaTiO_3$.

The RKKY interaction is used to explain the ferromagnetism in metals. According to this model the coupling between the localized magnetic moments is mediated by conduction electrons. This model also was originally proposed to describe ferromagnetism in DMO and DMS systems [8, 32]. Therefore, increasing the charge carrier density enhances the magnetic ordering. However, in our case we observed opposite: the magnetic ordering decreased with the increasing concentration of Fe ions. Thus, RKKY interaction cannot be adopted to explain the ferromagnetism in Fe-doped $BaTiO_3$.

We demonstrated that the appearance of the room-temperature ferromagnetism in 10% Fe-doped $BaTiO_3$ is concurrent with ordering of the oxygen vacancies. The oxygen vacancies are also considered as mediator in magnetic coupling of other DMO materials [32, 40]. So we can assume the same mechanism to explain the appearance of ferromagnetic interaction between Fe cations with nonzero atomic magnetic moment, i.e. the Bound magnetic polaron model described in Chapter 3 [32]. Electron, trapped in an oxygen vacancy, occupies an extended orbital state and overlaps with 3d shells of neighbouring Fe^{3+} cations. The Fe^{3+} ($3d^5$) ions are in high spin state and, therefore, have five half-filled orbitals available for interaction with trapped electron. Thus, the Pauli Exclusion Principle allows only antiparallel alignment of the trapped electron with the net magnetic moment of individual Fe^{3+} cations. Such interaction results in the parallel alignment of the net magnetic moments of neighbouring Fe^{3+} ions.

As it was shown above, for 20% Fe-doped $BaTiO_3$ the room-temperature ferromagnetism is correlated with formation of Fe-Fe pairs. Such formation of pairs was predicted theoretically [44] and later confirmed experimentally by Ray et al. [66]. According to their theoretical calculations the Fe atoms on Ti(2) sites are mutually ferromagnetically coupled. This interaction was found to be the strongest between the nearest-neighbours and weaken with increasing distance between Fe

atoms. Ray et al. [44] also showed that Fe atoms on Ti(1) sites contribute only to paramagnetism.

Our experimental results, shows that out of 10 face-sharing Ti_2O_9 octahedra one is fully substituted (i.e. Fe_2O_9), four are partially substituted (i.e. $FeTiO_9$) and the rest remained unsubstituted. Based on the determined octahedral occupancy about 17% of all Fe expected to contribute to ferromagnetism, however we found that only tiny amount of Fe ions are coupled ferromagnetically, while the rest Fe ions contribute to paramagnetism. Thus, our findings show that interpretation of origin of magnetic coupling is more complex than it was previously assumed.

7 CONCLUSIONS

Fe-doped $BaTiO_3$ is one of the most promising candidates for DMO materials, due to simultaneous presence of semiconducting and ferromagnetic properties at room temperature. However, the reports published on structural and functional properties of this material are rather contradictory. Thus, the principle aim of the thesis was to perform a detailed microscopic structural analysis of the Fe-doped $BaTiO_3$ with intention to reveal any structural features that may be responsible for induction of the room-temperature ferromagnetism.

The XRD analysis confirmed the admixture of tetragonal (*P4mm*) phase to the dominant hexagonal (*P63/mmc)* phase for the 10% Fe-doped $BaTiO_3$ treated at 1250 ºC for 5 h, and a single phase (*P63/mmc*) of hexagonal crystal structure for the rest of the samples. Magnetization measurements showed that all samples fired at 1250 ºC for 5 h are paramagnetic. However, all samples annealed at 1500 ºC exhibit room-temperature ferromagnetism, except 10% Fe-doped $BaTiO_3$ additionally annealed at 1500 ºC for 1 h sample, which is still paramagnetic. We found that saturation magnetization gradually increased with increasing the length of annealing time. The saturation magnetization was found to decrease with increasing Fe concentration.

To correlate the observed variations in the magnetic properties with microscopic processes that occur in the Fe-doped-$BaTiO_3$ during thermal treatment a detailed structural analysis has been performed using XAS methods (XANES and EXAFS).

Ti and Fe K-edge XANES analysis showed no variations in the valence state of Fe^{3+} and Ti^{4+} cations, excluding the double exchange interaction between Fe^{3+} and Fe^{4+} cations as a mechanism of the ferromagnetic interaction. The Fe K-edge EXAFS analysis of the samples treated at 1250 °C revealed that Fe^{3+} ions preferably occupy Ti(1) sites in 10% Fe-doped $BaTiO_3$, while in the 20% Fe-doped $BaTiO_3$ samples Fe^{3+} ions are randomly distributed over Ti(1) and Ti(2) crystallographic sites. During annealing at 1500 °C for 10 h redistribution of Fe cations from Ti(1) sites to Ti(2) sites was detected for both compositions. Such redistribution was accompanied by segregation of oxygen vacancies in O(2) crystallographic site. In 20% Fe-doped $BaTiO_3$ the formation of Fe-Fe pairs in face-sharing octahedrons on Ti(2) sites was observed. According to the theoretical calculations by Ray et al. [44] the ferromagnetic coupling between nearest-neighbours Fe cations on Ti(2) sites is the

strongest and decreasing with increasing the distance between Fe cations. Therefore, about 17% of all Fe ions are expected to contribute to ferromagnetism in the samples. However, our experimental results show that only tiny amount of Fe cations is ferromagnetically coupled. Thus, interpretation of the origin of room-temperature ferromagnetism in 20% Fe-doped $BaTiO_3$ is more complex issue.

Based on experimental results different driving mechanism have been identified, possible for the establishing the long-range ferromagnetic coupling in 10% and 20% Fe-doped $BaTiO_3$. In the samples with the nominal composition of $BaTi_{0.9}Fe_{0.1}O_3$ the oxygen vacancies are associated with induction of the room-temperature ferromagnetism and would favour the BMP model. This is not the case for $BaTi_{0.8}Fe_{0.2}O_3$ samples where the formation of Fe-Fe pairs coincides with induction of the ferromagnetism. However, our experiments disclosed that the magnetization is far too low to be explained only with the coupling of spins in the Fe-Fe pairs, which casts doubts on all the reports claiming that this mode of Fe ordering is responsible for the observed magnetization.

Yet, it has undoubtedly been seen that the induction of the room-temperature ferromagnetism is in some way associated with the high temperature annealing and most probably with the observed high-temperature diffusion processes.

8 SCIENTIFIC CONTRIBUTIONS

Part of the work presented in Chapter 5 was partially published as:

- Valant, M., Arčon, I., Mikulska, I., Lisjak, D., *Cation Order–Disorder Transition in Fe-Doped 6H-$BaTiO_3$ for Dilute Room-Temperature Ferromagnetism*. Chemistry of Materials, 2013. **25**(17): p. 3544-3550.

Part of the work presented in the Chapter 5 has been submitted to publication:

- I., Mikulska, Valant, M., Arčon, I., Lisjak, D., *X-ray absorption spectroscopy studies of the room-temperature ferromagnetic Fe-doped 6H-$BaTiO_3$.* Submitted to Journal of the American Ceramic Society, 2014.

9 BIBLIOGRAPHY

1. Ivanov, V.A., et al., *Spintronics and spintronics materials.* Russian Chemical Bulletin, 2004. **53**(11): p. 2357-2405.
2. Felser, C., G.H. Fecher, and B. Balke, *Spintronics: A challenge for materials science and solid-state chemistry.* Angewandte Chemie-International Edition, 2007. **46**(5): p. 668-699.
3. Bader, S.D. and S.S.P. Parkin, *Spintronics.* Annual Review of Condensed Matter Physics, Vol 1, 2010. **1**: p. 71-88.
4. Fabian, J., et al., *Semiconductor spintronics.* Acta Physica Slovaca, 2007. **57**(4-5): p. 565-907.
5. Awschalom, D.D. and M.E. Flatte, *Challenges for semiconductor spintronics.* Nature Physics, 2007. **3**(3): p. 153-159.
6. Dietl, T., *Ferromagnetic semiconductors.* Semiconductor Science and Technology, 2002. **17**(4): p. 377-392.
7. Ohno, H., *Ferromagnetic III-V heterostructures.* Journal of Vacuum Science & Technology B, 2000. **18**(4): p. 2039-2043.
8. Ohno, H., *Making nonmagnetic semiconductors ferromagnetic.* Science, 1998. **281**(5379): p. 951-956.
9. Ohno, H., *Properties of ferromagnetic III-V semiconductors.* Journal of Magnetism and Magnetic Materials, 1999. **200**(1-3): p. 110-129.
10. Dietl, T., *A ten-year perspective on dilute magnetic semiconductors and oxides.* Nature Materials, 2010. **9**(12): p. 965-974.
11. Nazmul, A.M., S. Sugahara, and M. Tanaka, *Transport properties of Mn delta-doped GaAs and the effect of selective doping.* Applied Physics Letters, 2002. **80**(17): p. 3120-3122.
12. Matsukura, F., et al., *Transport properties and origin of ferromagnetism in (Ga,Mn)As.* Physical Review B, 1998. **57**(4): p. R2037-R2040.
13. Fukuma, Y., et al., *Carrier-induced ferromagnetism in Ge0.92Mn0.08Te epilayers with a Curie temperature up to 190 K.* Applied Physics Letters, 2008. **93**(25).
14. Dietl, T., et al., *Zener model description of ferromagnetism in zinc-blende magnetic semiconductors.* Science, 2000. **287**(5455): p. 1019-22.

15. Pearton, S.J., et al., *Dilute magnetic semiconducting oxides.* Semiconductor Science and Technology, 2004. **19**(10): p. R59-R74.
16. Chambers, S.A., et al., *Ferromagnetism in oxide semiconductors.* Materials Today, 2006. **9**(11): p. 28-35.
17. Coey, J.M.D., *Dilute magnetic oxides.* Current Opinion in Solid State & Materials Science, 2006. **10**(2): p. 83-92.
18. Sharma, P., et al., *Ferromagnetism above room temperature in bulk and transparent thin films of Mn-doped ZnO.* Nature Materials, 2003. **2**(10): p. 673-677.
19. Kittilstved, K.R. and D.R. Gamelin, *Manipulating polar ferromagnetism in transition-metal-doped ZnO: Why manganese is different from cobalt (invited).* Journal of Applied Physics, 2006. **99**(8).
20. Punnoose, A., et al., *Development of high-temperature ferromagnetism in SnO2 and paramagnetism in SnO by Fe doping.* Physical Review B, 2005. **72**(5).
21. Kundaliya, D.C., et al., *On the origin of high-temperature ferromagnetism in the low-temperature-processed Mn-Zn-O system.* Nature Materials, 2004. **3**(10): p. 709-714.
22. Adhikari, R., et al., *Structure and magnetism of Fe-doped SnO(2) nanoparticles.* Physical Review B, 2008. **78**(2).
23. Coey, J.M.D. and S.A. Chambers, *Oxide Dilute Magnetic Semiconductors-Fact or Fiction?* Mrs Bulletin, 2008. **33**(11): p. 1053-1058.
24. Valant, M., et al., *The Origin of Magnetism in Mn-Doped SrTiO3.* Advanced Functional Materials, 2012. **22**(10): p. 2114-2122.
25. Valant, M., et al., *Spin Ordering in Mn-Doped KTaO3?* Chemistry of Materials, 2010. **22**(6): p. 1952-1954.
26. Samanta, K., et al., *Raman scattering studies in dilute magnetic semiconductor ZnCoO.* Physical Review B, 2006. **73**(24): p. 245213.
27. Kolesnik, S., B. Dabrowski, and J. Mais, *Origin of spin-glass behavior of Zn-1-xMnxO.* Journal of Superconductivity, 2002. **15**(4): p. 251-255.
28. Abraham, D.W., et al., *Absence of magnetism in hafnium oxide films.* Applied Physics Letters, 2005. **87**(25).

29. Potzger, K., et al., *Fe implanted ferromagnetic ZnO.* Applied Physics Letters, 2006. **88**(5).
30. Kennedy, R.J., et al., *Hopping transport in TiO2 : Co: A signature of multiphase behavior.* Applied Physics Letters, 2004. **84**(15): p. 2832-2834.
31. Nasirpouri, F.N.A.e.I., *Nanomagnetism and spintronics : fabrication, materials, characterization and applications*. 2011, [Singapore]: World Scientific.
32. Coey, J.M.D., M. Venkatesan, and C.B. Fitzgerald, *Donor impurity band exchange in dilute ferromagnetic oxides.* Nature Materials, 2005. **4**(2): p. 173-179.
33. Akai, H., *Ferromagnetism and its stability in the diluted magnetic semiconductor (In,Mn)As.* Physical Review Letters, 1998. **81**(14): p. 3002-3005.
34. Blinowski, J. and P. Kacman, *Double exchange in mixed-valency diluted magnetic semiconductors.* Acta Physica Polonica A, 1996. **90**(4): p. 731-734.
35. Blinowski, J., P. Kacman, and J.A. Majewski, *Ferromagnetic superexchange in Cr-based diluted magnetic semiconductors.* Physical Review B, 1996. **53**(15): p. 9524-9527.
36. Wei, X.K., et al., *Structure, electrical and magnetic property investigations on dense Fe-doped hexagonal $BaTiO_3$.* Journal of Applied Physics, 2011. **110**(11).
37. Nakayama, H. and H. Katayama-Yoshida, *Theoretical prediction of magnetic properties of Ba(Ti1-xMx)O-3 (M=Sc,V,Cr,Mn,Fe,Co,Ni,Cu).* Japanese Journal of Applied Physics Part 2-Letters, 2001. **40**(12B): p. L1355-L1358.
38. Liu, H.X., B.B. Cao, and C.J. O'Connor, *Structural and magnetic properties of single-crystalline Co-doped barium titanate nanoparticles.* Journal of Magnetism and Magnetic Materials, 2010. **322**(7): p. 790-793.
39. Liu, H.X., B.B. Cao, and C. O'Connor, *Intrinsic magnetism in BaTiO3 with magnetic transition element dopants (Co, Cr, Fe) synthesized by sol-precipitation method.* Journal of Applied Physics, 2011. **109**(7).
40. Wei, X.K., et al., *Origin of ferromagnetism and oxygen-vacancy ordering induced cross-controlled magnetoelectric effects at room temperature.* Journal of Applied Physics, 2012. **111**(7).

41. Wei, J.J., et al., *Magnetoelectric effect in bilayer composites of Fe-doped BaTiO(3) and terfenol-D.* Journal of Physics-Condensed Matter, 2008. **20**(8).
42. Wei, X.K., et al., *Structural modulation and magnetic properties of hexagonal Ba(Ti1-xFex)O3-delta ceramics.* Physica B-Condensed Matter, 2010. **405**(23): p. 4851-4854.
43. Ray, S., et al., *Defect controlled room temperature ferromagnetism in Co-doped barium titanate nanocrystals.* Nanotechnology, 2012. **23**(2).
44. Ray, S., et al., *High temperature ferromagnetism in single crystalline dilute Fe-doped BaTiO(3).* Physical Review B, 2008. **77**(10).
45. Dang, N.V., et al., *Structural, optical and magnetic properties of polycrystalline BaTi1-xFexO3 ceramics.* Journal of Applied Physics, 2011. **110**(4).
46. Radaelli, G., et al., *Electric control of magnetism at the Fe/BaTiO3 interface.* Nat Commun, 2014. **5**.
47. Guo, Z.G., et al., *Structural, magnetic and dielectric properties of Fe-doped $BaTiO_3$ solids.* Modern Physics Letters B, 2012. **26**(9).
48. Lin, F.T., et al., *Effect of annealing atmosphere on magnetism for Fe-doped BaTiO3 ceramic.* Physica B-Condensed Matter, 2008. **403**(17): p. 2525-2529.
49. Lin, F.T., et al., *Influence of doping concentration on room-temperature ferromagnetism for Fe-doped BaTiO3 ceramics.* Journal of Magnetism and Magnetic Materials, 2008. **320**(5): p. 691-694.
50. Lin, F.T. and W.Z. Shi, *Effects of doping site and pre-sintering time on microstructure and magnetic properties of Fe-doped BaTiO3 ceramics.* Physica B-Condensed Matter, 2012. **407**(3): p. 451-456.
51. Lin, F.T. and W.Z. Shi, *Influence of non-isovalent ion substitution at A site on microstructure and magnetic properties of Ba(Ti0.3Fe0.7)O-3 ceramic.* Journal of Alloys and Compounds, 2010. **495**(1): p. 167-172.
52. Rajamani, A., et al., *Faraday rotation, ferromagnetism, and optical properties in Fe-doped BaTiO3.* Journal of Applied Physics, 2005. **98**(6).
53. Maier, R. and J.L. Cohn, *Ferroelectric and ferrimagnetic iron-doped thin-film BaTiO3: Influence of iron on physical properties.* Journal of Applied Physics, 2002. **92**(9): p. 5429-5436.

54. Maier, R., et al., *Ferroelectricity and ferrimagnetism in iron-doped BaTiO3.* Applied Physics Letters, 2001. **78**(17): p. 2536-2538.
55. Xu, B., et al., *Room-temperature ferromagnetism and ferroelectricity in Fe-doped BaTiO3.* Physical Review B, 2009. **79**(13).
56. Qiu, S.Y., et al., *Phase evolution and room temperature ferroelectric and magnetic properties of Fe-doped BaTiO3 ceramics.* Transactions of Nonferrous Metals Society of China, 2010. **20**(10): p. 1911-1915.
57. Keith, G.M., et al., *Synthesis and characterisation of doped 6H-BaTiO3 ceramics.* Journal of the European Ceramic Society, 2004. **24**(6): p. 1721-1724.
58. Nguyen, H.M., et al., *Tetragonal and hexagonal polymorphs of BaTi1-xFexO3-delta multiferroics using x-ray and Raman analyses.* Applied Physics Letters, 2011. **99**(20).
59. Vanderah, T.A., J.M. Loezos, and R.S. Roth, *Magnetic Dielectric Oxides: Subsolidus Phase Relations in the BaO:Fe2O3:TiO2System.* Journal of Solid State Chemistry, 1996. **121**(1): p. 38-50.
60. Grey, I.E., et al., *Structure Analysis of the 6H–Ba(Ti, Fe3+, Fe4+)O3−δSolid Solution.* Journal of Solid State Chemistry, 1998. **135**(2): p. 312-321.
61. Mashkina, E., C. McCammon, and F. Seifert, *A Mossbauer study of oxygen vacancy and cation distribution in 6H-BaTi1-xFexO3-x/2.* Journal of Solid State Chemistry, 2004. **177**(1): p. 262-267.
62. Chikada, S., K. Hirose, and T. Yamamoto, *Analysis of Local Environment of Fe Ions in Hexagonal BaTiO3.* Japanese Journal of Applied Physics, 2010. **49**(9).
63. Dechakupt, T., et al., *Electrical and Aging Properties of Doped Barium Titanate Ceramics.* Ferroelectrics, 2010. **403**: p. 97-103.
64. Wei, X.K., et al., *Structural evolution induced by acceptor doping into BaTiO3 ceramics.* Journal of Alloys and Compounds, 2010. **508**(2): p. 486-493.
65. Chakraborty, T., S. Ray, and M. Itoh, *Defect-induced magnetism: Test of dilute magnetism in Fe-doped hexagonal BaTiO3 single crystals.* Physical Review B, 2011. **83**(14).

66. Chakraborty, T., et al., *Microscopic distribution of metal dopants and anion vacancies in Fe-doped BaTiO3-delta single crystals.* Journal of Physics-Condensed Matter, 2013. **25**(23).
67. Grey, I.E., L.M.D. Cranswick, and C. Li, *Accurate site occupancies for light atoms from powder X-ray data? Oxygen vacancy ordering in 6H-BaFe0.67Ti0.33O3-delta (delta = 0.08 and 0.32).* Journal of Applied Crystallography, 1998. **31**: p. 692-699.
68. Colson, T.A., M.J.S. Spencer, and I. Yarovsky, *A DFT study of the perovskite and hexagonal phases of BaTiO3.* Computational Materials Science, 2005. **34**(2): p. 157-165.
69. Vonsovskiĭ, S.V., *Magnetism*. 1974, New York,: J. Wiley.
70. du Trémolet de Lacheisserie, E., D. Gignoux, and M. Schlenker, *Magnetism: Fundamentals, Materials and Applications*. 2002: Springer.
71. Cullity, B.D. and C.D. Graham, *Introduction to magnetic materials*. 2nd ed. 2009, Hoboken, N.J.: IEEE/Wiley. xvii, 544 p.
72. Blundell, S., *Magnetism in condensed matter*. Oxford master series in condensed matter physics. 2001, Oxford ; New York: Oxford University Press. xii, 238 p.
73. Chtchelkanova, A., S.A. Wolf, and Y. Idzerda, *Magnetic interactions and spin transport*. 2003, New York: Kluwer Academic. xxii, 572 p.
74. Ashcroft, N.W. and N.D. Mermin, *Solid state physics*. 1976, New York,: Holt. xxi, 826 p.
75. Halliday, D., R. Resnick, and J. Walker, *Fundamentals of physics*. 7th ed. 2005, Hoboken, NJ: Wiley.
76. Getzlaff, M., *Fundamentals of magnetism*. 2008, Berlin ; New York: Springer. xiv, 387 p.
77. Coey, J.M.D., *Magnetism and magnetic materials*. 2010, Cambridge: Cambridge University Press. xii, 614 p.
78. Tauxe, L., T.A.T. Mullender, and T. Pick, *Potbellies, wasp-waists, and superparamagnetism in magnetic hysteresis.* Journal of Geophysical Research-Solid Earth, 1996. **101**(B1): p. 571-583.
79. Richter, C. and B.A. van der Pluijm, *Separation of paramagnetic and ferrimagnetic susceptibilities using low temperature magnetic susceptibilities*

and comparison with high field methods. Physics of the Earth and Planetary Interiors, 1994. **82**(2): p. 113-123.

80. Stöhr, J. and H.C. Siegmann, *Magnetism : from fundamentals to nanoscale dynamics*. Springer series in solid-state sciences,. 2006, Berlin ; New York: Springer. xvii, 820 p.
81. Torrance, J.B., M.W. Shafer, and T.R. Mcguire, *Bound Magnetic Polarons and Insulator-Metal Transition in Euo.* Physical Review Letters, 1972. **29**(17): p. 1168-&.
82. Dietl, T., et al., *Spintronics*. 2009: Elsevier Science.
83. Recnik, A., *Twins in barium titanate.* Acta Chimica Slovenica, 2001. **48**(1): p. 1-50.
84. Akimoto, J., Y. Gotoh, and Y. Oosawa, *Refinement of hexagonal BaTiO3.* Acta Crystallographica Section C, 1994. **50**(2): p. 160-161.
85. Sinclair, D.C., et al., *Structure and electrical properties of oxygen-deficient hexagonal BaTiO3.* Journal of Materials Chemistry, 1999. **9**(6): p. 1327-1331.
86. Megaw, H.D., *Crystal structure of double oxides of the perovskite type.* Proceedings of the Physical Society, 1946. **58**(2): p. 133.
87. Harada, J., T. Pedersen, and Z. Barnea, *X-ray and neutron diffraction study of tetragonal barium titanate.* Acta Crystallographica Section A, 1970. **26**(3): p. 336-344.
88. Ravel, B., *Ferroelectric phase transitions in oxide perovskites studied by XAFS*. 1997, University of Washington. p. 224.
89. Kwei, G.H., et al., *Structures of the Ferroelectric Phases of Barium-Titanate.* Journal of Physical Chemistry, 1993. **97**(10): p. 2368-2377.
90. Wu, Z., *Preparation and Characterization of Nanotube Ferrofluids by Template-Directed Methods*, in *der Fakultдt fьr Ingenieurwissenschaften und Informatik*. 2011, Universitдt Ulm. p. 137.
91. Nalwa, H.S., *Deposition and Processing*. 2001: Elsevier Science & Technology Books.
92. Ravel, B. and M. Newville, *ATHENA, ARTEMIS, HEPHAESTUS: data analysis for X-ray absorption spectroscopy using IFEFFIT.* Journal of Synchrotron Radiation, 2005. **12**: p. 537-541.

93. Rangus, M., et al., *Spectroscopic Investigation of Ti-Modified Aluminum-Free Zeolite-Beta Crystallization.* Chemistry of Materials, 2011. **23**(5): p. 1337-1346.
94. Arcon, I., et al., *XANES analysis of Fe valence in iron gall inks.* X-Ray Spectrometry, 2007. **36**(3): p. 199-205.
95. Pantelouris, A., et al., *The influence of coordination geometry and valency on the K-edge absorption near edge spectra of selected chromium compounds.* Chemical Physics, 2004. **300**(1-3): p. 13-22.
96. Lytle, F.W. and R.B. Greegor, *Discussion of X-Ray-Absorption near-Edge Structure - Application to Cu in the High-Tc Superconductors La1.8sr0.2cuo4 and Yba2cu3o7.* Physical Review B, 1988. **37**(4): p. 1550-1562.
97. Dominko, R., et al., *On the Origin of the Electrochemical Capacity of Li2Fe0.8Mn0.2SiO4.* Journal of the Electrochemical Society, 2010. **157**(12): p. A1309-A1316.
98. Rehr, J.J., R.C. Albers, and S.I. Zabinsky, *High-Order Multiple-Scattering Calculations of X-Ray-Absorption Fine-Structure.* Physical Review Letters, 1992. **69**(23): p. 3397-3400.
99. Makovec, D., et al., *Structure of manganese zinc ferrite spinel nanoparticles prepared with co-precipitation in reversed microemulsions.* Journal of Nanoparticle Research, 2009. **11**(5): p. 1145-1158.
100. Kodre, A., et al., *Extended x-ray absorption fine structure study of phase transitions in the piezoelectric perovskite K0.5Na0.5NbO3.* Journal of Applied Physics, 2009. **105**(11).
101. Dang, N.V., et al., *Structure of BaTi1-xFexO3-delta Multiferroics Using X-ray Analysis.* Chinese Journal of Physics, 2012. **50**(2): p. 262-270.
102. Vijatovic, M.M., J.D. Bobic, and B.D. Stojanovic, *History and Challenges of Barium Titanate: Part II.* Science of Sintering, 2008. **40**(3): p. 235-244.